Optical Fibre-based Hydrophone and Critical Ignition in Detonation Cells

by

Kevin Cheevers

Thesis submitted to the University of Ottawa
in partial fulfillment of the requirements for the
For the M.A.Sc degree in Mechanical Engineering

Department of Mechanical Engineering
Faculty of Engineering
University of Ottawa

Abstract

This thesis is composed of two distinct parts. The first part of this work addresses the problem of critical ignition behind a decaying shock wave in the context of cellular detonations. Low-pressure (4.1 kPa) shock tube experiments were performed in a thin rectangular channel using the highly-unstable mixture of $CH_4 + 2O_2$ and the weakly-unstable mixture of $2H_2 + O_2 + 7Ar$, with Schlieren visualization of the flow field. The dynamics of the lead shock in a detonation cell was reconstructed from measurements of the lead shock position and curvature. The post-shock state and the expansion rate along the path of a Lagrangian particle crossing the lead shock at any given point in the cell cycle were evaluated with the shock jump and shock change equations. The chemical evolution behind the shock was then integrated using a detailed chemistry model. Quenching of the post-shock reaction zone was found within the first half of the detonation cell for both mixtures, with quenching occurring earlier in the highly unstable mixture. Simplified models derived from 1-step and 2-step chemistry models very accurately predict the quenching of the post-shock reactions and the evolution of the ignition delay through the cell.

The second part describes the assembly and characterization of a fibre-optic probe hydrophone (FOPH) for the measurement of shock waves associated with blast-induced neuro-trauma. Compared to traditional polyvinylidene difluoride (PVDF) hydrophones, the assembled FOPH has a higher bandwidth and smaller active diameter, which are comparable to the characteristic time and thickness of shock waves associated with blast-induced neuro-trauma. However, the sensitivity of FOPHs are substantially lower than traditional hydrophones. We assemble a FOPH and provide detailed calculations and measurements of its sensitivity $\left(0.66 \frac{\text{mV}}{\text{MPa}}\right)$, noise floor, and spatial resolution. The 150 MHz bandwidth, limited by the photodetector, is sufficient for resolving shock waves with over-pressures of up to 174 kPa with 3 measurement points. Experimental measurements of the system noise gives a floor of 260 $\frac{\text{Pa}}{\sqrt{\text{Hz}}}$. A detailed noise analysis finds that the system

is limited by photodetector noise $\left(215\ \frac{\text{Pa}}{\sqrt{\text{Hz}}}\right)$, which is $4\times$ the fundamental shot noise limit, closely followed by a laser noise of $150\ \frac{\text{Pa}}{\sqrt{\text{Hz}}}$. We conclude that the system noise floor is insufficient for resolved measurements of the post-shock pressure in the range associated with blast-induced neuro-trauma. From our noise analysis, we quantify the sensitivity enhancement required for resolving this regime, and we conclude that sensitivity-enhancing fibre-coatings could provide a sufficient increase in sensitivity.

Foreword

The work performed consists of two separate studies, each written as a part of this two-part thesis. The first part of this thesis contains the study performed on detonation wave structure. The generality of the combustion mechanism in a detonation wave and the quenching of the post-shock ignition is experimentally studied. To this end, shock tube experiments and chemical kinetic integrations of the post-shock state are performed.

The second part of this thesis develops a fibre-optic sensor which can be used to measure the pressure profile of a shock wave associated with blast-induced neuro-trauma. The measurement system is characterized, after which the limitations in spatial resolution, time resolution, and pressure resolution are analysed. The current capabilities of the system are finally presented alongside potential improvements.

Acknowledgements

I would first and foremost like to thank Dr. Matei Radulescu for not only co-supervising the development of this thesis, but for giving me the opportunity to be an undergraduate research assistant prior to my enrolment into graduate studies. This experience eventually convinced me to continue my studies under his supervision, which culminated in the submission of the present work. I look forward to continuing my studies under his supervision.

Similarly, I would like to thank Dr. Raphael St-Gelais for agreeing to co-supervise this thesis, notably assisting with the development of a fibre-optic hydrophone. His help in understanding optical fibre-based systems is much appreciated, as was the guidance given throughout the present work.

I would additionally like to thank the members of the Detonation & Reactive Dynamics Laboratory for their company throughout recent years. Their assistance was vital to the shock tube experiments performed for this thesis. Likewise, I would like to thank the members of the Micro and Nano Systems Laboratory for their input over the course of the development of the hydrophone.

Finally, I would like to express my profound gratitude towards my parents and my partner for their constant support and inspiration throughout this endeavour.

Table of Contents

List of Tables

List of Figures

Nomenclature

List of Abbreviations

ADC Analog-to-digital converter

APC Angled polished connectors

CJ Chapman-Jouguet

FFT Fast Fourier Transform

FOPH Fibre-optic probe hydrophone

NEP Noise Equivalent Power

PVDF Polyvinyl-difluoride

RIN Relative Intensity Noise

SNR Signal-to-noise Ratio

ZND Zel'dovich-Doering-Von Neumann

List of Roman Symbols used in Part I

c	Sound Speed
c_p	Heat capacity at constant pressure per unit mass
c_v	Heat capacity at constant volume per unit mass
$\frac{D}{Dt}$	Material derivative along a particle path
Da	Damkohler Number
D	Shock propagation speed
e	Internal energy per unit mass
h	Enthalpy
k_i	Induction rate fitting constant
k_r	Reaction rate fitting constant
L_{cell}	Detonation cell length
M	Mach Number
p	Pressure
Q	Chemical energy released per unit mass
n_i	Reaction order of the induction stage
n_r	Reaction order of the reaction stage
R	Specific gas constant
T	Temperature
t	Time
t_{is}	Ignition delay without expansion
t_i	Ignition delay with expansion
t_{cell}	Detonation cell time
u	Flow speed
v	Specific volume
W	Molecular weight
x	Distance
Y	Mass fraction

List of Greek Symbols used in Part I

α	Characteristic rate of expansion
β	Nondimensional heat release
χ	Parameter characterizing the detonability of a reactive mixture
ϵ	Inverse activation energy
η	Shock wave sonicity in the post-shock state
γ	Ratio of specific heats $\left(\frac{c_p}{c_v}\right)$
κ	Lead shock curvature
ξ	Induction zone progress variable
ρ	Material density
$\dot{\sigma}$	Thermicity
$\dot{\sigma}_A$	Losses due to area change
$\dot{\omega}$	Molar rate of creation of a chemical species
ζ	Controlling parameter of ignition with expansion

List of Roman Symbols used in Part II

A Attenuation

A_{loss} Attenuation loss in an optical system

BW Measurement bandwidth

c Sound Speed

$\mathbb{G}$ Photodetector gain

h Planck Constant

k_B Boltzmann Constant

M Mach Number

n_g Refractive index of a glass fibre

n_m Refractive index of a test fluid

n_{points} Number of measurements points within a shock wave

P Optical power

p Pressure

p_∞ Stiffening pressure

$\mathbb{R}$ Photodetector responsivity

R Optical reflection coefficient

S_F Scaling Factor

T Temperature

$t_{residence}$ Residence time of a passing wave over a point

$t_{resolution}$ Characteristic time resolution

V Voltage

Z Impedance Load

List of Greek Symbols used in Part II

Δ	Shockwave thickness
δ	Measurement tool active diameter
λ	Optical wavelength
μ	Material viscosity
ν	Laser frequency
ρ	Material density

List of Subscripts

0	State ahead of a shock wave
24Xs	Quantity pertaining to the Lecroy WaveSurfer 24Xs-A
a	Quantity used considering air as the test fluid
AD2	Quantity pertaining to the Analog Discovery 2
CJ	Chapman-Jouguet State
C5658	Quantity pertaining to the Hamamatsu C5658
det	Quantity taken at a photodetector
H	Derivative taken along the Hugoniot
II	Second-Order Perturbation
laser	Quantity produced by the laser diode
PDA10A2	Quantity pertaining to the Thorlabs PDA10A2
S	Quantity or derivative taken at the shock
shot	Shot noise
w	Quantity used considering water as the test fluid

Part I

Critical Ignition Behind Decaying Shock Waves : Application to Detonation Cells

Chapter 1

Introduction

Detonations are self-sustained combustion waves propagating in a reactive medium at supersonic speeds. The total chemical energy dictates the propagation velocity. The average speed of propagation observed in experiments is well predicted by Chapman-Jouguet (CJ) theory [4]. A simple model for the reaction zone structure of detonations is the Zel'dovich-Doering-Von Neumann (ZND) model. The model assumes a planar shock wave followed by a zone of energy release occurring after an induction time [5, 6], seen in Figure 1.1 a). In reactive gases, however, the induction time is very sensitive to changes in the strength of the lead shock through the exponential sensitivity of reaction rates on temperature. In turn, the strength of the lead shock is sensitive to changes in the post-shock rate of energy release. This feedback leads to an instability. In multiple dimensions, due to this instability, the lead shock takes on a cellular structure, sketched in Figure 1.1 b).

The unsteady structure of cellular detonations differs substantially from the ZND detonation model. Cellular detonations have a complex multi-dimensional structure composed of a Mach shock, an incident shock, and a transverse shock, all of which intersect at triple points. The triple points propagate along the lead shock tracing the fish scale-like pattern plotted as a dashed line in Figure 1.1 b). When these triple points collide, the strength of the lead shock is amplified. Between triple point collisions, the shock strength continuously

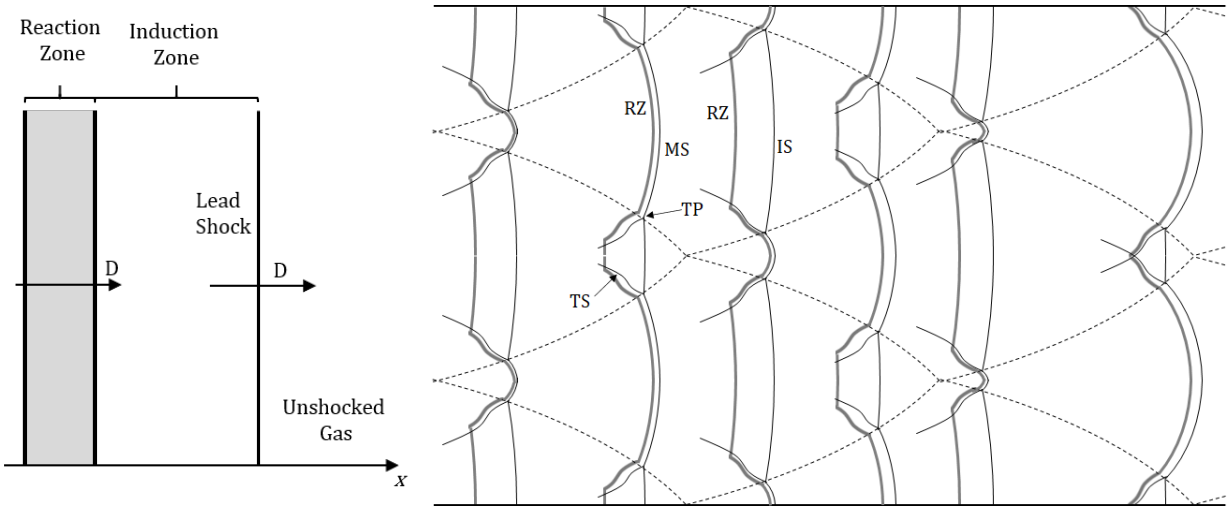

(a) (b)

Figure 1.1: A schematized detonation which propagates from left-to-right. a) The conventional representation of a detonation consisting of a planar lead shock followed by a reaction zone, separated by an induction zone. b) A cellular detonation propagating from left-to-right, identifying the important features of a cellular detonation. IS : Incident shock. MS : Mach Shock. TS : Transverse Shock. TP :Triple point, located at the juncture of the three aforementioned shock waves. Reaction zones are sketched in grey.

decays. The variation of the shock speed can be quite large during a cell cycle, ranging from approximately $1.8D_{CJ}$ at the beginning of the cell cycle, to approximately $0.6D_{CJ}$ at the end of the cell [7], where D_{CJ} is the propagation velocity determined from CJ theory.

Subbotin was the first to identify two types of detonation cellular structures [8], the difference between the two lying in the mechanism of combustion and the regularity of detonation cell structure. Weakly unstable detonations have very regular structures, with the most regular structure registered in the hydrogen-oxygen-argon system, as illustrated in Figure 1.2 a). In contrast, highly unstable detonations have irregular structures, an example being methane-oxygen detonations showed in Figure 1.2 b). The main feature of weakly unstable detonations is the prompt termination of the induction zone close the lead shock and transverse waves. In contrast, the main features in highly unstable detonation cells are the same Mach stem, incident shock, transverse waves, and reaction waves as in the stable detonations, but one also sees pockets of unburnt gas further downstream, which

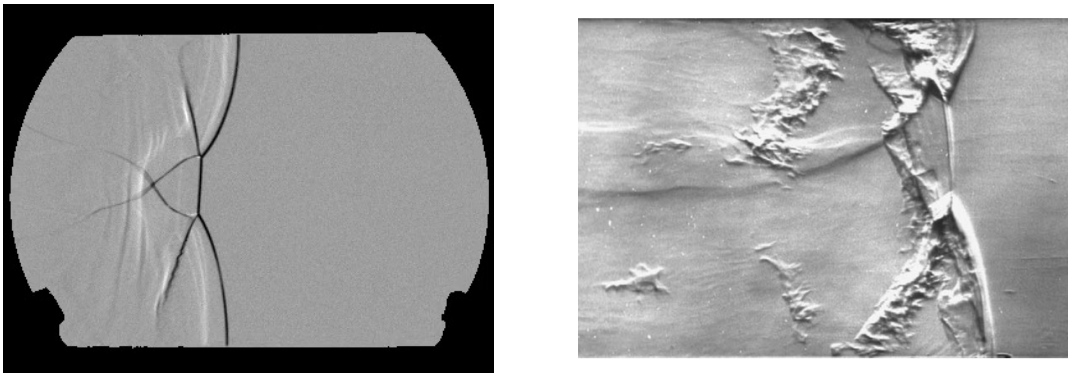

(a) (b)

Figure 1.2: Schlieren visualization of detonations propagating from left-to-right through a) a stable mixture of $2H_2$+O_2+7Ar [1], and b) a highly unstable mixture of CH_4 + $2O_2$, with visible turbulent mixing pockets of unreacted flow in the post-shock region [2].

burn via diffusive phenomena (wrinkled flames) [1]. The increased delays in combustion for these non-reacted pockets is due mainly to the higher sensitivity of the induction time to shock temperature in these systems.

Radulescu and co-workers previously categorized the instability (and conversely the regularity) of a detonable mixture as a function of its χ parameter [9]. This is found to be a function of the mixture's sensitivity, and the ratio of the induction time to explosion time,

$$\chi = \frac{Ea}{RT}\frac{t_i}{t_r}. \tag{1.1}$$

Mixtures with small χ parameters, such as $2H_2$ + O_2 + 7Ar, are weakly unstable and their cellular structure are similar to that shown in Figure 1.2 a). Higher χ parameters are associated with unstable mixtures, such as CH_4 + $2O_2$, and their cellular structure resembles that shown in Figure 1.2 b). Distinguishing between mixtures is important when considering that the secondary initiation mechanisms are different for each structure.

Modelling and predicting the effective energy release rate behind the front of cellular detonations is very important for predicting the dynamics of detonations in practical problems such as detonation arrestors, detonation engines, and cloud ignition. The prediction of this rate of energy release behind the lead shock in cellular detonations remains very

challenging. With current numerical simulations, it is currently not feasible to perform well-resolved numerical simulations of detonations for macroscopic applications due to the large range of scales present. The smallest scale required for such simulations is on the order of 10^{-7} m to properly resolve the reaction zone structure, the thin reaction zones, and their interaction with turbulence at the Kolmogorov scale [10]. In contrast, the largest scales in applications are on the order of the device size, and approximately 10 to 1000 larger than the characteristic cell dimension. This *outer* scale is on the order of meters. To solve these problems, one requires a macroscopic model which can accurately predict the energy release occurring behind the lead shock in detonations. Recognizing the non-stationarity of the lead shock at scales smaller than the cell size, the first step would thus be studying the effect of the unsteadiness of the shock on the reaction zone structure, such that one can predict the distribution of ignition delays in the reaction zone structure of detonations.

A global reaction model necessarily needs to model the various combustion mechanisms found within cellular detonations to accurately model the average rate of energy release. This would be a very useful model in the context of engineering scale numerical simulations to reduce computational cost by modelling the small-scale phenomena which are expensive to resolve. An initial model which can accurately predict the evolution of the ignition delay and rate of heat release behind the lead shock is the first step towards a global reaction model. This model will also determine the point within a detonation cell cycle where the reaction zone quenches, and the proportion of gas crossing the lead shock which reacts through secondary combustion mechanisms.

The problem of ignition within the structure of an unsteady cellular detonation can be posed as a generic problem of ignition behind a decaying shock wave. If the shock dynamics (its curvature, speed, and acceleration) are locally known *a priori*, the ignition dynamics can be determined. This problem, summarized in Figure 1.3, consists of a Lagrangian particle that crosses a shock whose strength decays with time, after which the particle

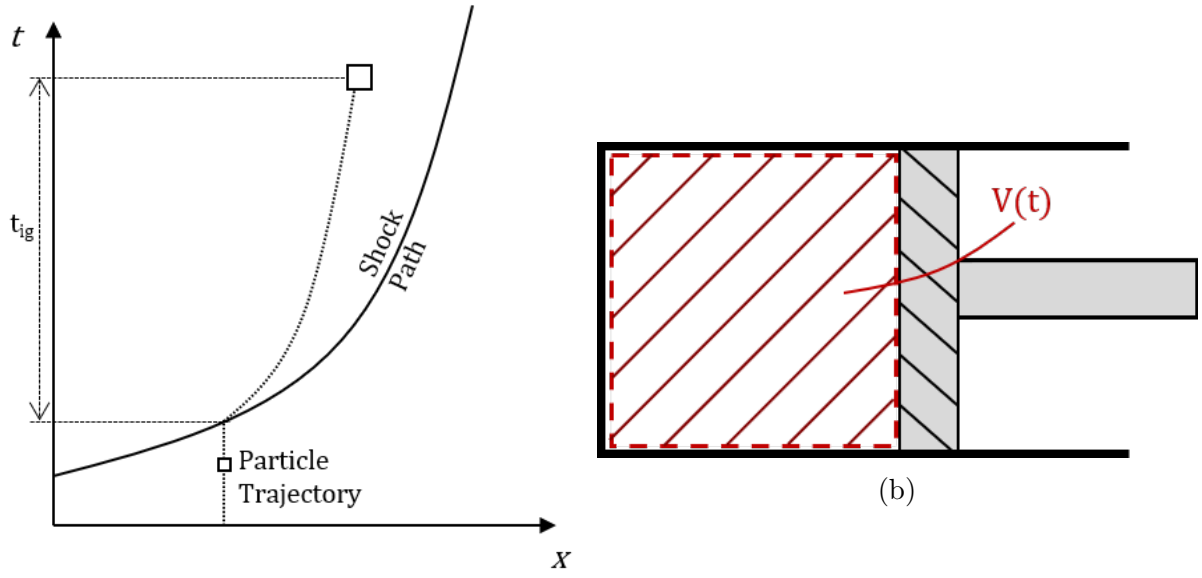

(a) (b)

Figure 1.3: A representation of the problem of ignition behind a decaying shock wave. a) An x-t diagram showing a Lagrangian particle whose trajectory crosses the lead shock. The particle expands in the post-shock state after an initial compression by the shock wave and ignites after an induction time t_{ig} elapses. b) The problem of a piston whose volume expands as a function of time is used to model the expanding Lagrangian particle in the post-shock state.

undergoes an expansion. This particle expansion can be visualized as a zero-dimensional combustor problem whose volume change in time is described in terms of the dynamics of the shock. To solve these problems and thus be able to predict the ignition of a particle behind the shock, one needs to know the relation between the shock dynamics and the time history of the volume change of the Lagrangian particle after it crosses the shock.

Lundstrom and Oppenheim first studied this problem to address the ignition in cellular detonations in mixtures of hydrogen-oxygen diluted with nitrogen [11], which have a fair regularity and lie between the two extremes discussed above. The dynamics of the lead shock were approximated as those of a Taylor-Sedov blast wave. Using blast wave theory, they inferred the rate of particle expansion along particle paths and used this to evaluate the particle's ignition delay under the influence of a decaying lead shock. Using ignition kinetics derived from shock tube experiments, they found that ignition behind the lead

shock is quenched within the first half of the cellular cycle. The gas particles that cross the lead shock after this quenching point are ignited through other secondary mechanisms, such as heating by transverse shock waves.

More recently, Eckett and Shepherd developed an approximate solution by reformulating the reactive inviscid Euler equations in the vicinity of the shock wave to treat the evolution of ignition [12]. Their local analysis of the competing terms for the rate of energy release along particle paths revealed the possibility of ignition quenching. This critical ignition was associated with a critical decay rate of the lead shock. For decay rates higher than this critical decay rate, the post-shock reaction is quenched reminiscent to the quenching in the model of Lundstrom and Oppenheim. At around the same time as Eckett's work, Vidal and Khasainov [13] also independently analyzed this same problem and arrived at similar conclusions.

Austin [14] further used Eckett's model to study the decoupling of the decaying lead shock and the subsequent reaction wave in numerical simulations of idealized cellular detonations. She analysed the numerical simulations performed by Gamezo and co-workers of a cellular detonation propagating through a 2-dimensional channel [15] described by a one-step Arrhenius reaction. The activation energy of the gas was increased between simulations to increase the instability of the detonation. Austin used the time evolution of the lead shock velocity along the centreline of the tube to calculate the shock decay. Comparing the critical decay rate calculated by applying Eckett's model to data measured from results obtained from the numerical simulation, local decoupling of the reaction wave and lead shock is found for unstable detonations with high activation energy. The decay rate of the lead shock at the intermediate activation energy is not comparable to the critical decay until the very end of the cycle, thus no local decoupling was predicted.

The problem of ignition behind decaying shock waves has also been addressed by Kiyanda and Higgins, who performed photographic studies of cellular detonations of methane-oxygen [16], which have a very irregular structure. Similar to Lundstrom and Oppenheim,

they used blast wave theory for inert gases to determine the evolution of temperature as a function of time along a particle path. The evolution of temperature with time was then used as a forcing function during the integration of a homogeneous reactor modelling a Lagrangian particle. This phenomenological model found quenching halfway through the cellular cycle. The experiments suggested that turbulent mixing of unreacted flow pockets with products of combustion were the secondary initiation mechanism.

More recently, an alternative solution to the problem of shock induced ignition behind non-steady shocks has been proposed by Radulescu and Maxwell [17]. They formulated their model using the energy and species evolution equations, with the rate of change of volume of a particle as a function of time appearing explicitly in their formulation. The volumetric forcing function can be predicted using arbitrary shock dynamics in the Newtonian limit or by using a local analysis at the shock using the shock change equations [18]. In their analysis, using one-step chemistry, critical ignition was also found to depend on the volumetric expansion rate of the Lagrangian particles in the post-shock state.

Previous research has thus showed that expansion induced quenching was present in unstable detonations, while the situation was not clear for weakly unstable ones, idealized simulations showing that was not the case. The models differed between the authors. The present study attempts to unify the theoretical treatment for ignition behind decaying shocks. It addresses this problem of ignition behind decaying shocks in the context of cellular detonation waves, at the two extremes of cellular regularity.

In the present thesis, the results of shock tube experiments are reported for weakly unstable detonations in a mixture of argon-diluted hydrogen-oxygen, since it is the system with the most regular structure known to date. In contrast, analysis of highly unstable detonations in methane-oxygen mixtures reported in our group previously are also analysed to further compare with the findings of Kiyanda and Higgins. In these systems, high speed photographic sequences of the experiments are used to determine the dynamics of the lead shock. The rate of volumetric expansion along a particle path is inferred from

these measurements using the shock change equations. The knowledge of the volumetric expansion source term allows the integration of the energy and species equations in order to study ignition. The problem is addressed numerically for realistic multi-specie kinetic models and theoretically for one and two step reaction formulations. These simplifications allow analytical treatments using asymptotic methods. Chapter 2 contains the details of the models used to predict ignition behind decaying shocks. Chapter 3 details the physical setup for the shock tube experiments. Chapter 4 contains the results of the shock tube experiments. Chapter 5 contains the results obtained by applying the solution methodology to the experiments. Chapter 6 summarizes the findings and draws the conclusions of this work.

Chapter 2

Models for Ignition Behind Decaying Shocks

The goal of this chapter is to develop models which can predict the ignition time of a particle which crosses a decaying shock, given the dynamics of the lead shock. Recalling the problem as posed in Figure 1.3, one can study this problem as that of a Lagrangian particle which crosses a decaying lead shock at an arbitrary time and ignites after an induction time has elapsed since its crossing. This is achieved by using the shock dynamics to describe the expansion rate of the shocked particle in the post-shock region and using this volumetric change in time along the particle path as a source term in the energy equation. It is assumed that the information about the lead shock and its variation in time is known *a priori*.

2.1 Shock Dynamics to Predict $\frac{1}{\rho}\frac{D\rho}{Dt}$

The analysis of the shock dynamics comprises linking the evolution of the lead shock in time to the evolution of the post-shock particle expansion rate. Consider a Lagrangian particle crossing a shock wave. The state of this particle is described by the conservation laws

of mass, momentum, and energy. The reactive Euler equations for quasi-one-dimensional flow in a tube with a non-uniform cross-sectional area are:

$$\frac{1}{\rho}\frac{D\rho}{Dt} = -\frac{\partial u}{\partial x} - \dot{\sigma}_A, \tag{2.1}$$

$$\rho\frac{Du}{Dt} = -\frac{\partial p}{\partial x}, \tag{2.2}$$

$$\frac{Dp}{Dt} = c^2\frac{D\rho}{Dt} + \rho c^2\dot{\sigma}, \tag{2.3}$$

in which ρ is the density, u is the velocity, p is the pressure, c is the sound speed, and $\dot{\sigma}$ is the thermicity. For a multi-component mixture of ideal gases, it is given by

$$\dot{\sigma} = \sum_{i=1}^{N}\left(\frac{\bar{W}}{W_i} - \frac{h_i}{c_pT}\right)\frac{DY_i}{Dt}, \tag{2.4}$$

where W_i is the molecular weight of the i$^{\text{th}}$ component, $\bar{W}$ is the mean molecular weight of the mixture, h_i is the specific enthalpy of the i$^{\text{th}}$ specie and c_p is the mixture frozen specific heat.

The derivative $\frac{D}{Dt} = \frac{\partial}{\partial t} + u\frac{\partial}{\partial x}$ is the material derivative taken along the trajectory of a fluid element. The rate of strain induced by area changes of the tube is

$$\dot{\sigma}_A = \frac{D\ln A}{Dt}, \tag{2.5}$$

with A the cross-sectional area of the tube.

If we model the propagation of a shock wave in a ray-tube with variable area, the rays serve as the tube walls, and the area is not variable in time. At the shock,

$$\dot{\sigma}_A = u\frac{\partial \ln A}{\partial x} = u\kappa, \tag{2.6}$$

where κ is the shock wave curvature. The conservation equations can be combined with the Rankine-Hugoniot shock jump relations to derive the so-called shock change equations.

The reader is referred to the derivations by Fickett and Davis [6] and Radulescu [18]. These shock change equations relate the derivatives of fluid variables behind the shock with the shock wave strength, curvature, and acceleration. One of the shock change equations can be written as,

$$\frac{1}{\rho}\frac{D\rho}{Dt} = \frac{-\dot{\sigma} + u\kappa(1-\eta) + \frac{1}{\rho c^2}\left(\frac{dp}{dt}\right)_S \left(1 + \rho_0(D-u_0)\left(\frac{du}{dp}\right)_H\right)}{\eta}, \tag{2.7}$$

which relates the rate of particle expansion (on the left-hand side) to the variables describing the shock dynamics, such as the shock speed D, its acceleration through the rate of change of the post shock pressure $\left(\frac{dp}{dt}\right)_S$ and its curvature κ. In this equation, η is the sonicity

$$\eta = (1-M)^2, \tag{2.8}$$

in which M is the Mach number of the flow behind the shock relative to the shock wave. All variables without a subscript refer to properties evaluated at the post-shock state, which are dependent on a single variable measuring the shock strength through the shock jump relations and the initial state density ρ_0 and particle velocity u_0. The term $\left(\frac{du}{dp}\right)_H$ represents the change of post shock particle speed with the post shock pressure, which is a property of the mixture; it is measured along the shock Hugoniot curve.

If one considers the state immediately behind the shock in the induction zone, the thermicity $\dot{\sigma}$ is found to be negligible. The resulting shock change equation becomes:

$$\frac{1}{\rho}\frac{D\rho}{Dt} = \frac{u\kappa(1-\eta) + \frac{1}{\rho c^2}\left(\frac{dp}{dt}\right)_S \left(1 + \rho_0(D-u_0)\left(\frac{du}{dp}\right)_H\right)}{\eta}. \tag{2.9}$$

The shock change equation can also be written in terms of the specific volume $v = \frac{1}{\rho}$, or

$$\frac{1}{\rho}\frac{D\rho}{Dt} = -\frac{1}{v}\frac{Dv}{Dt}. \tag{2.10}$$

Simplifications to the shock change equation can be made by the assumption of a perfect gas [18], to obtain a simplified relationship for

$$\left(\frac{dp}{dt}\right)_S = \frac{4\gamma p_0 M_s}{\gamma+1}\dot{M}_s, \tag{2.11}$$

and

$$\left(\frac{du}{dp}\right)_H = \frac{c_0(M_s^2+1)}{2M_s^3\gamma p_0}. \tag{2.12}$$

where γ is the ratio of specific heats and M_s is the propagation Mach number of the shock with respect to the flow ahead of the shock, i.e., $M_s = (D-u_0)/c_0$. By subsequently assuming a strong shock and zero flow speed ahead of the shock, our shock change equation reduces to

$$\frac{1}{\rho}\frac{D\rho}{Dt} = \frac{6}{\gamma+1}\frac{\dot{D}}{D} + 2D\kappa\frac{\gamma-1}{(\gamma+1)^2}, \tag{2.13}$$

in which $\dot{D}$ is the acceleration of the shock. This form of the shock change equation separates the two terms contributing to the gas volumetric expansion behind the shock: the shock unsteadiness and lateral strain rate. The working assumption is made that the volumetric expansion rate evaluated immediately behind the shock remains constant throughout the induction zone, which will permit modelling the ignition process. This is explained next.

2.2 Ignition Along the Particle Path

Consider a particle of gas at some initial state which eventually crosses a shock at time t_s, as sketched in Figure 1.3 a). This inert shock will increase the pressure, temperature, and density within this particle of gas in accordance with the shock jump relations. From the moment the particle crosses the lead shock, this problem becomes that of a particle of gas subjected to a volumetric expansion in time, with the expansion exerted on the particle

found using the shock change equation mentioned in the previous section. What remains in order to solve this problem is to integrate the state within this particle of gas in time. If the time history of density (or volume) is known for a fluid particle crossing the shock wave, the process of ignition of a fluid particle is described by the chemical kinetic laws describing the production or depletion of the different species at the prescribed density, as well as the energy budget.

The characteristic rate of expansion α

$$\alpha = \frac{1}{v}\frac{Dv}{Dt} = -\frac{1}{\rho}\frac{D\rho}{Dt}, \tag{2.14}$$

experienced by the particle is the value it has acquired when crossing the shock wave, given by the shock dynamics via the shock change equation. In the foregoing, we assume each particle retains this characteristic expansion rate. With this approximation, the exact energy equation for diffusionless flow, namely,

$$c_v\frac{DT}{Dt} = -\sum_{i=1}^{N} e_i\frac{DY_i}{Dt} + \frac{p}{\rho^2}\frac{D\rho}{Dt} \tag{2.15}$$

simplifies to an ordinary differential equation:

$$c_v\frac{dT}{dt} = -\sum_{i=1}^{N} e_i\frac{dY_i}{dt} - \alpha\frac{p}{\rho}. \tag{2.16}$$

The relations describing the evolution of chemical compositions along the particle path for diffusionless flow, namely,

$$\rho\frac{DY_i}{Dt} = \dot{\omega}_i W_i, \tag{2.17}$$

are also ODE's, which can be re-written for clarity as

$$\rho \frac{dY_i}{dt} = \dot{\omega}_i W_i. \tag{2.18}$$

In these equations, $\dot{\omega}_i$ is the molar production rate of i per unit time, per unit volume. It can be evaluated from the law of mass action from chemical kinetics, given the rate of individual reactions.

The problem to solve is thus described by the initial value problem given by the two ODE's (2.16) and (2.18), with initial conditions $Y_i = Y_{i,0}$, and $T = T_s$ evaluated immediately behind the shock.

2.2.1 Multiple Species Real Gas Calculation

The ignition problem described in the previous section can be solved numerically for realistic thermo-chemical data of reactive mixtures of interest. To this end, we use Cantera, which is a suite of tools developed to solve numerical problems involving chemically reacting flows[19]. This package handles the integration of the species and energy conservation ODEs described in section 2.2. The problem of a particle undergoing a volumetric expansion in time can be modelled in Cantera using the zero-dimensional homogeneous reactor package. This models a Lagrangian fluid element which has a homogeneous state and species composition at every point in time, and no gradients in any spatial dimension within the control system. The initial state of the particle upon crossing the lead shock is calculated using the *postshock_fr* method available in the Shock and Detonation Toolbox developed by Kao and Shepherd [20]. The chemical model used for the integration is the San Diego 2016 model developed by Williams [21], containing a total of 57 species. The volumetric expansion rate of the particle in the post-shock state calculated from the dynamics of the lead shock and is imposed as the constraint on the reactor.

As an example, consider a shock wave propagating at the CJ velocity into a mixture

of stoichiometric methane-oxygen at an initial state of 4.1 kPa and 293 K. The post-shock state is subjected to increasing expansion. The aforementioned equations are integrated to visualize the evolution of the chemical processes behind the shock. The evolution in time of the post-shock temperature, rate of heat release, and pressure are shown in Figure 2.1. Three curves are included on each graph, representing a shock which propagates at a constant CJ velocity without any decay, and two shocks which propagate at CJ velocity with increasing decay rates. The shock propagating with no expansion has a very noticeable jump in temperature and pressure coinciding with a spike in the rate of heat release, which occurs at the ignition time following an induction zone with relatively little heat release or increase in temperature or pressure. The second curve is that of a post-shock state with increased post-shock expansion. This curve sees an increased ignition delay due to the expansion felt by the shocked gas. In addition to the increased ignition delay, one notices that the peak temperature, pressure, and rate of heat release reached are lower than those of the gas without any expansion. Due to the expansion in this curve, one notices that the post-combustion temperature and pressure steadily decreases once the heat release becomes negligible due to expansion cooling. If one increases the post-shock expansion even further, the expansion of the gas will dominate the post-shock chemical kinetics such that the gas will not react, as the cooling overcomes the effect of post-shock heat release. In this case, no noticeable increase in temperature or pressure occurs, and the rate of heat release remains smaller by a few orders of magnitude than those associated with combustion. One can deduct from these figures that a critical expansion rate exists, with smaller expansion allowing for ignition behind the lead shock and higher expansion leading to the quenching of the post-shock combustion.

As an alternative to studying the temperature and thermicity evolutions, one can study the evolution of chemical species in the post-shock region. This can offer an alternative description of ignition and quenching of the post-shock combustion process. Figure 2.2 a) shows the mass fraction of a reactant (CH_4). Studying the solution corresponding to

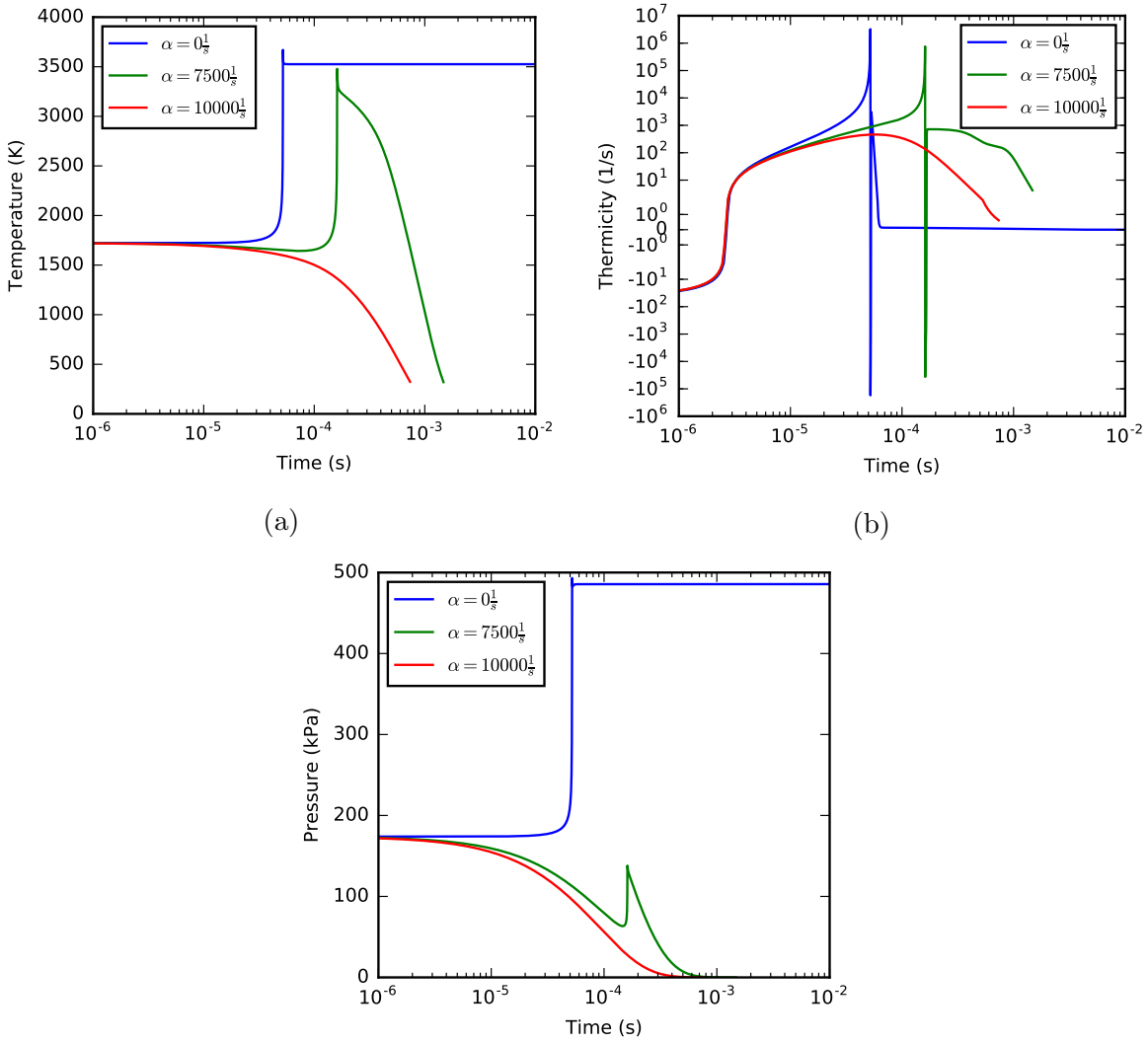

Figure 2.1: Results of the integration of a shock wave propagating through a quiescent mixture of stoichiometric methane-oxygen, with an initial pressure and temperature of 4.1 kPa and 293 K, for increasing expansion rates $\alpha = -\frac{1}{v}\frac{Dv}{Dt}$. a) temperature vs time, b) thermicity vs time, and c) pressure vs time

a shock without any expansion, one sees a sharp decline in the mass fraction of the reactants occurring after the induction time. As in Figure 2.1, the induction time increases with increasing expansion rates between the ignition cases. When increasing the expansion further, the reactants are very minimally depleted, clearly differentiating between the expansion rates associated with ignition and quenching. Similarly, in Figure 2.2 b), the product mass fraction increases by an order of magnitude when ignition occurs, until plateauing at the final product concentration. The quenched case has an increasing product mass fraction, however the products never constitute the majority of the chemical species in the mixture, plateauing at around 1% of the overall mass.

In Figure 2.2 b), one notices that a CJ detonation with a small post-shock expansion rate has a higher mass fraction of products than the CJ detonation without any post-shock expansion. In experiments, a sonic surface exists and the thermodynamic evolution of particles behind this sonic surface will be affected by the rear boundary conditions, whereas particles ahead of this sonic surface will not be affected by acoustic waves. The zero-dimensional reactor model used to integrate the state of the particle does not have any such constraint applied, and the volumetric expansion is applied for the duration of the particle's post-shock evolution. For particles which ignite, the post-combustion temperature plotted in Figure 2.1 a) is very high, thus reactions predicted by a one-step Arrhenius equation occur very quickly, on a timescale smaller than the timescale of volumetric expansion. As the temperature initially decreases from upwards of 3000 K, the intermediate species present in large amounts recombine to form larger stable molecules such as H_2O and CO_2. As the temperature decreases, the reaction rate increases until changes in chemical composition occur on a timescale similar or greater than the timescale of volumetric expansion. The remainder of the integration in time sees very little change in chemical composition as an equilibrium is reached. For an expansion rate of 7500 $\frac{1}{s}$, this occurs around 10^3 s, after which the reactant, intermediate, and product mass fractions cease to meaningfully vary. Particles undergoing no post-shock volumetric expansion do

not follow this recombination pathway, thus the final state of the integration is similar to the expanding particle's state immediately following combustion. This is shown in Figure 2.2 c), as the blue and green particles' state immediately following ignition contain similar mass fractions of product and intermediate species.

2.2.2 1-step Combustion Model

The problem of ignition in the presence of volumetric expansion can also be modeled with a single overall reactive step for a perfect gas. Such a treatment permits to obtain an analytical result for the effect of expansion on ignition delay and the critical expansion rate that can prevent ignition. The following treatment follows closely the development of Radulescu & Maxwell [17], who extended the model of Eckett and co-workers [12]. As in the general problem outlined in the previous section, the problem is defined by the energy conservation along a fluid element, the rate of expansion (assumed known *a priori* through the constant α) and the evolution of the mass fraction of products Y, modeled here with a single step Arrhenius reaction. In dimensional terms, the initial value problem becomes

$$\begin{aligned} c_v \frac{dT}{dt} &= Q\frac{dY}{dt} + \frac{p}{\rho^2}\frac{d\rho}{dt}, \\ \frac{d\ln\rho}{dt} &= -\alpha, \\ \rho\frac{dY}{dt} &= k\rho^n(1-Y)^n \exp\left(-\frac{Ea}{RT}\right), \end{aligned} \tag{2.19}$$

with initial conditions immediately behind the shock denoted with a subscript s:

$$T(t=0) = T_s,\ \rho(t=0) = \rho_s \text{ and } Y(t=0) = 0. \tag{2.20}$$

It is worthwhile to non-dimensionalize these equations by choosing the scales T_s as characteristic temperature, ρ_s as characteristic density and the ignition delay obtained in the

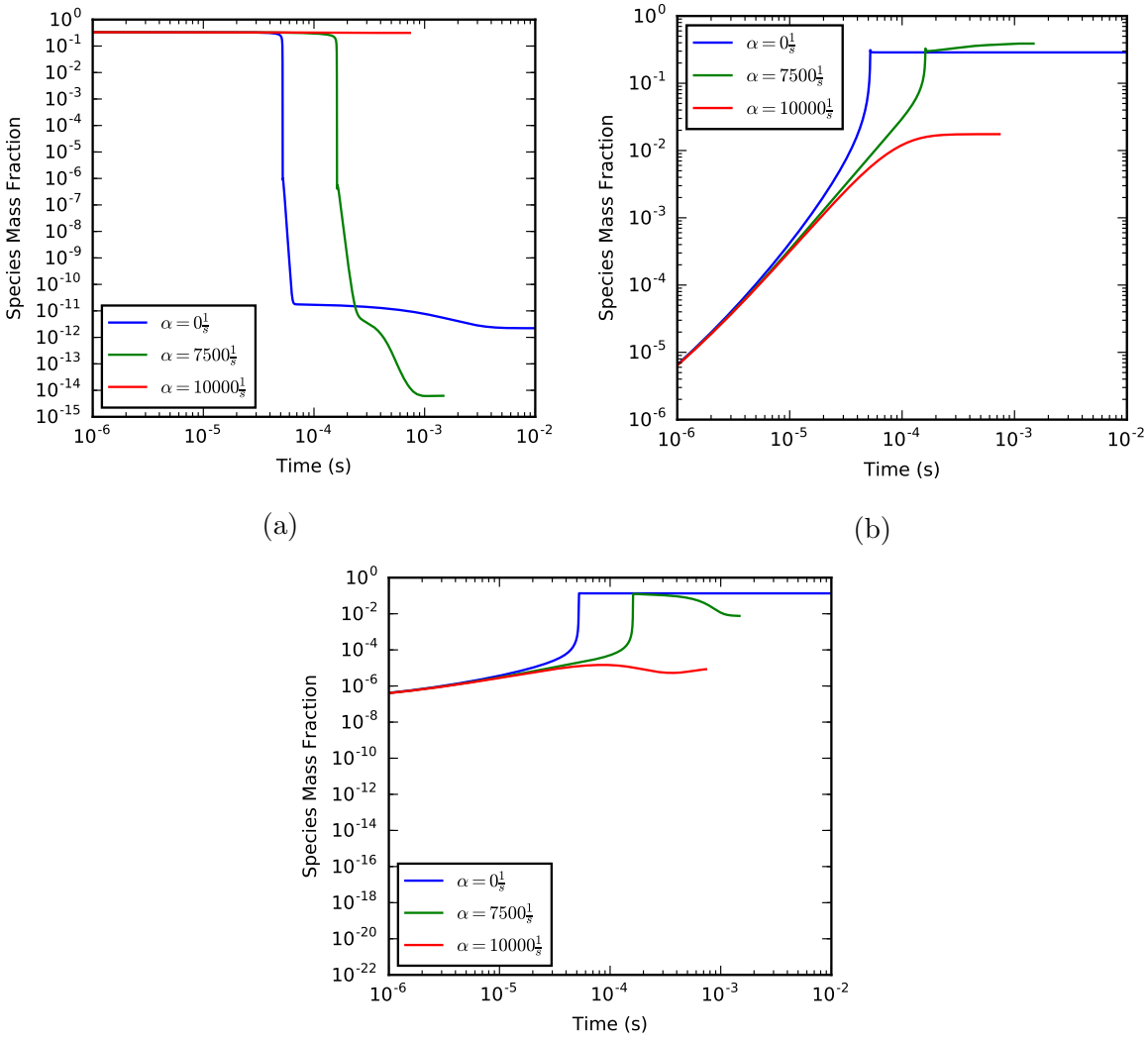

(a) (b)

(c)

Figure 2.2: Results of the integration of a shock wave propagating through a quiescent mixture of stoichiometric methane-oxygen, with an initial pressure and temperature of 4.1 kPa and 293 K, for increasing expansion rates $\alpha = -\frac{1}{v}\frac{Dv}{Dt}$. Mass fraction as a function of time, for a) reactants (CH_4), b) products (H_2O), and c) intermediates (OH^-).

limit of high activation energy as time scale, i.e.,

$$t_{is} = k^{-1}\rho_s^{-(n-1)}\left(\frac{Ea}{RT_s}\right)^{-1}\left(\frac{Q}{c_vT_s}\right)^{-1}\exp\left(\frac{Ea}{RT_s}\right). \tag{2.21}$$

The latter choice will be justified *a posteriori* in the following perturbation analysis in the limit of high activation energy. The new non-dimensional variables and parameters are

$$\tilde{T} = \frac{T}{T_s},\ \tilde{\rho} = \frac{\rho}{\rho_s},\ \tilde{t} = \frac{t}{t_{is}},\ \epsilon = \left(\frac{Ea}{RT_s}\right)^{-1},\ \beta = \frac{Q}{c_vT_s},\ \mathrm{Da} = \frac{1}{\alpha t_{is}}, \tag{2.22}$$

where we have introduced the Damkohler number Da to denote the ratio of expansion time over the nominal ignition delay time. This parameter controls the ignition in the resulting non-dimensional initial value problem:

$$\begin{aligned}
\frac{d\tilde{T}}{d\tilde{t}} &= \beta\frac{dY}{d\tilde{t}} - \frac{\gamma-1}{\mathrm{Da}}\tilde{T},\\
\frac{d\ln\tilde{\rho}}{d\tilde{t}} &= -\frac{1}{\mathrm{Da}},\\
\frac{dY}{d\tilde{t}} &= \frac{\epsilon}{\beta}\tilde{\rho}^{n-1}(1-Y)^n\exp\left(\frac{\tilde{T}-1}{\epsilon\tilde{T}}\right),\\
\tilde{T}(\tilde{t}=0) = 1,\ \tilde{\rho}(\tilde{t}=0) = 1 &\text{ and } Y(\tilde{t}=0) = 0.
\end{aligned} \tag{2.23}$$

By inspection, the energy equation has the same form as the classical Frank-Kamenetskii homogeneous explosion problem with heat loss [22], the loss term being proportional to temperature. This system is characterized by a critical value of loss rate that can suppress the thermal ignition, parametrized by the Damkohler number. Although the critical Damkohler number can be determined numerically, as it was performed in the previous section for full chemistry, an analytical approximation can be found in the limit of high

activation energy (or small ϵ). We perturb the initial state by a small perturbation, i.e.,

$$\tilde{T} = 1 + \epsilon \tilde{T}_{II}(\tilde{t}) + \mathcal{O}(\epsilon^2), \tag{2.24}$$

$$Y = 0 + \epsilon \lambda_{II}(\tilde{t}) + \mathcal{O}(\epsilon^2), \tag{2.25}$$

$$\tilde{\rho} = 1 + \epsilon \tilde{\rho}_{II}(\tilde{t}) + \mathcal{O}(\epsilon^2). \tag{2.26}$$

We substitute these expansions in the original problem (2.23) and solve at the various orders. The $\mathcal{O}(1)$ problem is the constant state at the initial condition. The $\mathcal{O}(\epsilon)$ problem becomes:

$$\frac{d\tilde{T_{II}}}{d\tilde{t}} = \exp\left(\tilde{T}_{II}\right) - \zeta, \; \tilde{T}_{II}(\tilde{t} = 0) = 0, \tag{2.27}$$

with

$$\zeta \equiv \frac{1}{\epsilon} \frac{\gamma - 1}{\mathrm{Da}} = \mathcal{O}(1). \tag{2.28}$$

This can be integrated to yield the solution to the temperature perturbation in the induction zone as

$$\tilde{T}_{II}(\tilde{t}) = \ln\left(\frac{\zeta}{1 - (1 - \zeta)e^{\tilde{t}\zeta}}\right). \tag{2.29}$$

Thermal ignition is associated with the manifestation of $\tilde{T}_{II} \to \infty$ as $\tilde{t} \to \tilde{t}_i$. Taking this limit in (2.29), we obtain an expression for the ignition delay $\tilde{t}_i$ in the presence of expansion

$$\tilde{t}_i = \ln\left(\left(\frac{1}{1 - \zeta}\right)^{\frac{1}{\zeta}}\right). \tag{2.30}$$

Ignition occurs in finite time only if $\zeta < 1$. The critical value of ζ, henceforth denoted with a $*$ as ζ^*, is 1. This is the condition for ignition in the presence of expansion. Note that ignition occurs at $\tilde{t}_i = 1$ when there is no expansion ($\zeta = 0$), hence justifying *a posteriori* our choice for time scale.

In dimensional variables, the condition for thermal ignition $\zeta < \zeta^* = 1$ is

$$\zeta = \frac{1}{\epsilon}\frac{\gamma - 1}{\mathrm{Da}} = \frac{Ea}{RT_s}(\gamma - 1)\,\alpha t_{is} < 1. \tag{2.31}$$

The comparison between the prediction of this analysis with the numerical integration of the full multi-specie problem will be discussed later in this chapter.

2.2.3 2-Step Combustion Model

As discussed in the introduction, critical ignition has been also addressed by Lundstrom and Oppenheim using a generalized ignition delay model. In the modern literature, the framework of their analysis falls within the scope of a two-step chemical model that is characterized by a thermally neutral induction zone followed by an exothermic stage. This structure does not necessarily associate the ignition with thermal explosion, but relies on either simulations or experiments to determine the effective kinetics of the induction delay time. The kinetics of the induction zone can also model a radical explosion in chain-branching systems. In any case, it is worthwhile formulating a two-step model for ignition with expansion and compare its predictions for the ignition delay variation with expansion rate and the critical conditions for ignition with the full chemistry and one-step model discussed above.

In the two-step model, the sequential induction and reaction zones are modelled by the rate equations

$$\frac{D\xi}{Dt} = k_i \rho^{n_i - 1} \exp\left(-\frac{E_a}{RT}\right), \tag{2.32}$$

$$\frac{DY}{Dt} = k_r \rho^{n_r - 1}(1 - Y)^{n_r} H(\xi), \tag{2.33}$$

where ξ is the progress variable of the induction zone, ranging from 0 to 1 at the end of the induction time and Y is the mass fraction of product, ranging from 0 to 1 in the main

reaction zone. The reaction zone only starts when the progress variable ξ of the induction zone reaches unity; $H(\xi)$ is the switch:

$$H(\xi) = \begin{cases} 0 & \text{for } \xi < 1 \\ 1 & \text{for } \xi \geq 1 \end{cases} \tag{2.34}$$

The parameters of the two step model are the rate constants rate multipliers k_i and k_r, the reaction orders n_i and n_r and the activation temperature of the induction zone Ea/R.

The same energy equation (2.19) and expansion rate hold as for the 1-step model discussed previously:

$$c_v \frac{dT}{dt} = Q\frac{dY}{dt} + \frac{p}{\rho^2}\frac{d\rho}{dt}, \tag{2.35}$$

$$\frac{d\ln\rho}{dt} = -\alpha, \tag{2.36}$$

with initial conditions immediately behind the shock denoted with a subscript s:

$$T(t=0) = T_s,\ \rho(t=0) = \rho_s,\ \xi(t=0) = 0,\ Y(t=0) = 0. \tag{2.37}$$

We again non-dimensionalize these equations by choosing the scales T_s as characteristic temperature, ρ_s as characteristic density and the ignition delay without expansion, which for the two-step model,

$$t_{is} = k_i^{-1}\rho_s^{-(n_i-1)} \exp\left(\frac{Ea}{RT_s}\right). \tag{2.38}$$

The new non-dimensional variables and parameters are

$$\tilde{T} = \frac{T}{T_s},\ \tilde{\rho} = \frac{\rho}{\rho_s},\ \tilde{t} = \frac{t}{t_{is}},\ \epsilon = \left(\frac{Ea}{RT_s}\right)^{-1},$$
$$\beta = \frac{Q}{c_v T_s},\ \mathrm{Da} = \frac{1}{\alpha t_{is}},\ \zeta = \frac{\gamma-1}{\epsilon \mathrm{Da}},\ \tilde{k}_r = k_r t_{is}\rho_s^{n_r-1}. \tag{2.39}$$

The resulting non-dimensional initial value problem becomes:

$$\begin{aligned}
\frac{d\tilde{T}}{d\tilde{t}} &= \beta\frac{dY}{d\tilde{t}} - \epsilon\zeta\tilde{T}, \\
\frac{d\ln\tilde{\rho}}{d\tilde{t}} &= -\epsilon\frac{\zeta}{\gamma-1}, \\
\frac{d\xi}{dt} &= \tilde{\rho}^{n_i-1}\exp\left(\frac{\tilde{T}-1}{\epsilon\tilde{T}}\right), \\
\frac{dY}{d\tilde{t}} &= \tilde{k}_r\tilde{\rho}^{n_r-1}(1-Y)^{n_r}H(\xi), \\
\tilde{T}(\tilde{t}=0)=1,\ \tilde{\rho}(\tilde{t}=0)=1\ &\xi(t=0)=0\ , Y(\tilde{t}=0)=0.
\end{aligned} \tag{2.40}$$

In the induction zone, there is no heat release and the problem is further simplified:

$$\begin{aligned}
\frac{d\tilde{T}}{d\tilde{t}} &= -\epsilon\zeta\tilde{T}, \\
\frac{d\ln\tilde{\rho}}{d\tilde{t}} &= -\epsilon\frac{\zeta}{\gamma-1}, \\
\frac{d\xi}{dt} &= \tilde{\rho}^{n_i-1}\exp\left(\frac{\tilde{T}-1}{\epsilon\tilde{T}}\right), \\
\tilde{T}(\tilde{t}=0)=1,\ \tilde{\rho}(\tilde{t}=0)=1,\ &\xi(t=0)=0.
\end{aligned} \tag{2.41}$$

These ODEs are readily integrated from the shock to the end of the induction zone, marking the ignition time $\tilde{t}=\tilde{t}_i$:

$$\int_0^1 d\xi = 1 = \int_0^{\tilde{t}_i}\tilde{\rho}^{n_i-1}\exp\left(\frac{\tilde{T}-1}{\epsilon\tilde{T}}\right)d\tilde{t}, \tag{2.42}$$

with $\tilde{\rho}(\tilde{t})$ and $\tilde{T}(\tilde{t})$ in the last integral given by

$$\tilde{\rho} = \exp\left(-\epsilon\frac{\zeta}{\gamma-1}\tilde{t}\right), \tag{2.43}$$

$$\tilde{T} = \exp\left(-\epsilon\zeta\tilde{t}\right). \tag{2.44}$$

This expression is an implicit relation that defines the ignition delay time in the presence of expansion, which can be evaluated numerically.

2.2.3.1 Reaction order $n_i = 1$

Analytical expressions can be obtained for a reaction order of $n_i = 1$. The implicit expression (2.42) for $\tilde{t_i}$ becomes:

$$\zeta = \frac{1}{\epsilon} \exp\left(\frac{1}{\epsilon}\right) \left(-\mathrm{Ei}\left(-\frac{1}{\epsilon}\right) + \mathrm{Ei}\left(-\exp\left(\epsilon\zeta\tilde{t_i}\right)\right)\right), \tag{2.45}$$

where Ei is the exponential integral function. The ignition limit corresponds to letting $\tilde{t_i} \to \infty$, yielding the critical condition for ignition

$$\zeta^* = \frac{\gamma - 1}{\epsilon \mathrm{Da}^*} = -\frac{1}{\epsilon} \exp\left(\frac{1}{\epsilon}\right) \mathrm{Ei}\left(-\frac{1}{\epsilon}\right). \tag{2.46}$$

The asymptotic expansion of this expression can also be written as

$$\zeta^* = \frac{\gamma - 1}{\epsilon \mathrm{Da}^*} = 1 - \epsilon + \mathcal{O}\left(\epsilon^2\right). \tag{2.47}$$

To order $\mathcal{O}(1)$, the limit agrees with the result obtained for the 1 step model given by (2.31).

The ignition delay time can also be expressed in closed form by linearizing (2.45) in ϵ, yielding

$$\tilde{t_i} = \frac{1 - \epsilon \ln\left(1 - \zeta\right) - \epsilon W\left(\frac{1}{\epsilon} \frac{e^{\frac{1}{\epsilon}}}{1-\zeta}\right)}{\epsilon^2 \zeta}, \tag{2.48}$$

in which W is the Lambert function, or product logarithm. This approximate solution exhibits the same behaviour as the implicit solution given in (2.45), specifically the asymptotic behaviour obtained near the limit, which differs from $\zeta \to 1$ due to the presence of logarithmic functions. The main advantage of this simplified solution is that $\tilde{t_i}$ is given

explicitly near the limit and reproduces the limit correctly.

2.2.3.2 Ignition with the two step model with $\zeta = \mathcal{O}(1)$

The analysis showed that the two step model limit expressed in terms of ζ was in agreement with that of the 1-step model to $\mathcal{O}(1)$, yielding a critical ignition limit given by $\zeta^* = 1$. It is worthwhile to further pursue this limit and determine the ignition delay predicted by the two-step model in the presence of expansion. For the one step model, the analysis required that $\zeta = \mathcal{O}(1)$ for balancing terms in the $\mathcal{O}(\epsilon)$ problem. It is straightforward to show that taking the expansions (2.24) and (2.26) to solve the problem given by (2.41), the leading order solution for the ignition delay requires $\zeta = \mathcal{O}(1)$ and $\gamma - 1 = \mathcal{O}(1)$ for matching and yields the same result for the ignition delay as the 1-step model, namely (2.30).

At $\mathcal{O}(\epsilon)$, we obtain:

$$\tilde{T}_{II} = -\zeta\tilde{t}, \tag{2.49}$$

$$\tilde{\rho}_{II} = -\frac{\zeta}{\gamma - 1}\tilde{t}. \tag{2.50}$$

resulting in the asymptotic approximations for temperature and density in the induction zone given by

$$\tilde{T} = 1 - \epsilon\zeta\tilde{t} + \mathcal{O}(\epsilon^2), \tag{2.51}$$

$$\tilde{\rho} = 1 - \epsilon\frac{\zeta}{\gamma - 1}\tilde{t} + \mathcal{O}(\epsilon^2). \tag{2.52}$$

The ignition delay is obtained by substituting these expressions in the integral expression given by (2.42), yielding:

$$1 = \int_0^{\tilde{t}_i} \left(1 - \epsilon(n_i - 1)\frac{\zeta}{\gamma - 1}\tilde{t} + ...\right) \exp\left(-\zeta\tilde{t}\right) d\tilde{t} \tag{2.53}$$

Evaluating the integral for $n_i = 1$ yields the same result as for the 1 step model given by (2.30), namely

$$\tilde{t}_i = \ln\left(\left(\frac{1}{1-\zeta}\right)^{\frac{1}{\zeta}}\right). \tag{2.54}$$

For $n_i \neq 1$, $\tilde{t}_i$ cannot be obtained in closed form. However, the ignition limit can be evaluated by taking the limit $\tilde{t}_i \to \infty$. Evaluating the integral, the condition for ignition becomes:

$$\zeta^* = \frac{\gamma - 1}{\epsilon \mathrm{Da}^*} = 1 - \epsilon \frac{n_i - 1}{\gamma - 1}. \tag{2.55}$$

The non-unity reaction order appears as a perturbation to the $\zeta^* = 1$ limit obtained above for the 1 step and 2 step models at leading order.

2.2.4 Comparison of the Simplified Models

The models derived previously in this chapter predict quenching in the limit of $\zeta \simeq 1$. It is interesting to also compare the evolution of the induction delay as a function of the controlling parameter ζ. Figure 2.3 plots this evolution, while considering the effect of the magnitude of the inverse activation energy ϵ. This allows us to study the effect of expansion in the induction zone on the predicted ignition delay obtained using simplified models.

Three different solutions modelling the evolution of the ignition delay are compared in Figure 2.3. The first solution is derived from the two-step model giving an implicit function of the ignition delay in (2.45). The second solution is obtained by making the assumption of $n_i = 1$, as in section 2.2.3.1, and linearizing the implicit two-step solution in ϵ under the assumption that this parameter is small. This second model yields an explicit function for the ignition delay as a function of the controlling parameter, shown in (2.48). The third model can be obtained independently using either a 1-step or 2-step combustion model. After a derivation following the development of Radulescu & Maxwell, who in turn

extended the model of Eckett and co-workers, an explicit solution is obtained under the assumption of a 1-step combustion model in the limit of high activation energy, shown in (2.30). An identical expression for the ignition delay is obtained from an asymptotic expansion of the temperature and density evolution in the induction zone while using a 2-step combustion model under the assumption that $\zeta = \mathcal{O}(1)$ and $\gamma - 1 = \mathcal{O}(1)$, shown in (2.54).

In the limit of a small inverse activation energy as shown in Figure 2.3 a), one notices the very good agreement between the predicted evolution of the ignition delay calculated using the previously presented solutions. The critical ignition limit is found to be $\zeta = 1$, which agrees with the predicted ignition limit when ϵ is small. Conversely, the predictions diverge when ϵ becomes large, as seen in Figure 2.3 b). Studying the evolution of the implicit 2-step solution given in (2.45), one notices that this solution correctly recovers the expected behaviour when the volumetric expansion rate is small, be it $\tilde{t}_i = t_{ig}/t_{is} \approx 1$. When increasing the controlling parameter, and thus the post-shock volumetric expansion rate, the ignition delay also increases and reaches the critical ignition limit sooner than the other simplified ignition models, at $\zeta \approx 0.85$. The approximate solution to 2-step chemistry plotted in green in Figure 2.3 b) initially under-predicts the ignition delay as $\tilde{t}_i \approx 0.83$ when ϵ becomes large. This model also recovers the critical ignition limit of $\zeta = 1$. When comparing with the implicit 2-step solution, this model is the least accurate of the three predictions of the ignition delay as it under-predicts the ignition delay early in the cell, and over-predicts the critical ignition limit. For its part, the solution obtained for 1-step and 2-step chemistry models under the assumption that $\zeta = \mathcal{O}(1)$ reproduces the expected behaviour for small values of the controlling parameter, however also recovers the critical ignition limit specified by $\zeta = 1$.

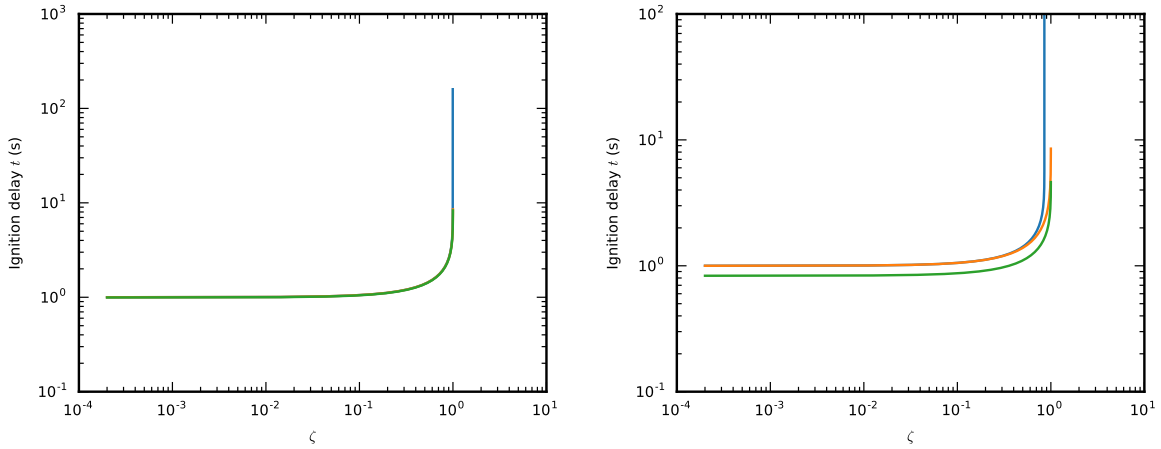

(a) (b)

Figure 2.3: Plot of the non-dimensional ignition $\tilde{t}_{ig}$ as a function of ζ, for the cases of a) $\epsilon = 0.005$ and b) $\epsilon = 0.2$. One notices deviation between the ignition delay predicted by simplified models when ϵ becomes large. Blue : Implicit 2-step solution given in (2.45) for $n_i = \mathcal{O}(1)$. Green : Approximate solution for 2-step chemistry obtained by linearizing the implicit solution in ϵ, given in (2.48). Orange : 1-step and 2-step solutions in the limit of $\zeta = \mathcal{O}(1)$ given in (2.30) and (2.54).

2.2.5 Comparison of Simplified Models with Detailed Chemistry

Having shown general agreement between the ignition delay predicted by the simplified models derived above, it is now of interest to compare these models with an integration of a post-shock state using detailed chemistry. To do this, we will study ignition behind a decaying shock wave propagating at its CJ velocity following the methodology proposed in sections 2.2 and 2.2.1. The lead shock will be subjected to increasing post-shock volumetric expansion rates (α) until the quenching of post-shock reactions occurs due to expansion cooling. The results obtained from the detailed chemical model can be compared with the simplified models by calculating the controlling parameter

$$\zeta = (\gamma - 1)\,\frac{E_a}{RT_s}\alpha t_{is}, \tag{2.56}$$

for each expansion rate studied. The expansion rate α is the only parameter in this equation which changes, as γ, E_a, T_s, and t_{is} are all properties of the shock and will thus only vary

with the shock speed.

Figure 2.4 shows the comparison of post-shock ignition delays, normalized by the ignition delay without expansion t_{is}, as a function of the controlling parameter. In the limit of small expansion rates, the predicted ignition delay found using simplified models agree with those found using detailed chemistry. The approximate 2-step model obtained by linearizing the implicit solution in ϵ (2.48) under-predicts the ignition delay by 10%-15% compared to the other models, but this tendency was also observed in section 2.2.4 when ϵ ceases to be small. There is excellent agreement when studying the critical ignition which occurs as $\zeta \to 1$. As seen in Figure 2.3 b), the implicit 2-step model has a critical ignition asymptote associated with a smaller value of ζ than the other models. This behaviour is also seen in critical ignition calculated using detailed chemistry, occurring at a smaller value of $\zeta \approx 0.8$ in Figure 2.4. The implicit 2-step model therefore recovers the ignition time predicted by detailed chemistry the best of any simplified model derived earlier in this chapter. Nevertheless, the approximate 2-step model obtained by linearizing the implicit solution in ϵ (2.48) and the model derived in the limit of $\zeta = \mathcal{O}(1)$ for 1-step and 2-step chemistry also recover critical ignition as $\zeta \to 1$. As seen in Figure 2.4, this criterion agrees with the critical ignition calculated using detailed chemistry.

2.2.6 Criterion for Ignition Behind Decaying Shock Waves

To summarize, we have now formulated a criterion for the critical ignition, which yields approximately the same result for both 1 step thermal explosions, 2 step models for chain-branching explosions. This criterion, derived in sections 2.2.2 and 2.2.3

$$\zeta = \frac{1}{\epsilon}\frac{\gamma - 1}{\mathrm{Da}} < 1, \tag{2.57}$$

was also found in very good agreement with the results of the integration using a realistic network of chemical reactions. This criterion can be recast in dimensional form in terms of

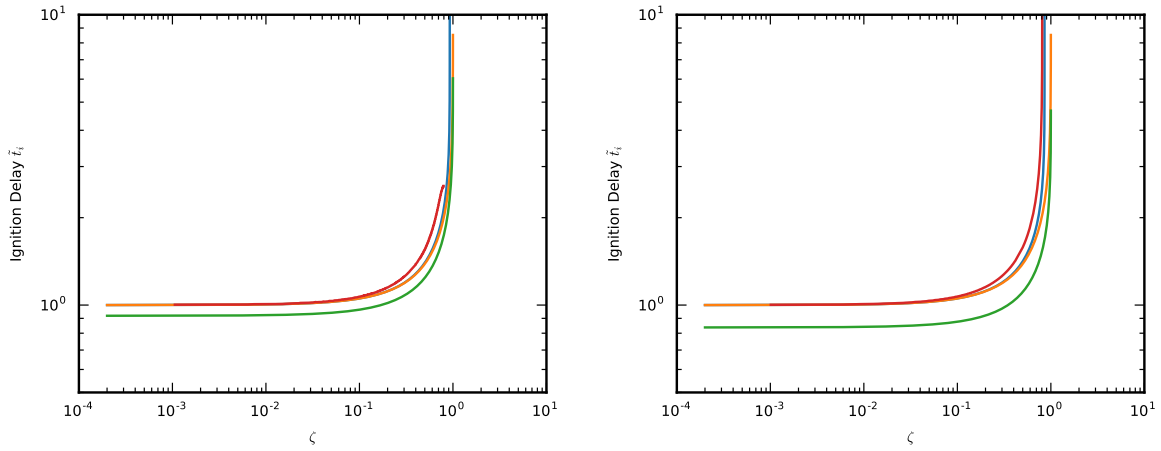

(a) (b)

Figure 2.4: The evolution of the non-dimensional ignition delay $\tilde{t}_{ig}$ as a function of ζ behind a shock wave propagating at the CJ velocity through a quiescent mixture of a) $2H_2 + O_2 + 7Ar$ with $p_0 = 4.1$ kPa ($\epsilon = 0.089$), and b) $CH_4 + 2O_2$ with $p_0 = 3.5$ kPa ($\epsilon = 0.194$). One notices the simplified models recover the evolution of the ignition delay obtained using full chemistry. Blue : Implicit 2-step solution given in (2.45) for $n_i = \mathcal{O}(1)$. Green : Approximate solution for 2-step chemistry obtained by linearizing the implicit solution in ϵ, given in (2.48). Orange : 1-step and 2-step solutions in the limit of $\zeta = \mathcal{O}(1)$ given in (2.30) and (2.54). Red : solution obtained by integrating the post-shock state using a detailed chemical model.

thermo-chemical properties of the gas at the post-shock state and the post-shock volumetric expansion rate,

$$\frac{Ea}{RT_s}\left(\gamma-1\right)\alpha t_{is}(T_s)<1. \tag{2.58}$$

Making use of the relation between expansion rate along the particle and the shock dynamics, obtained via the shock change equations (2.13), this criterion can be re-written for a strong shock in a perfect gas as:

$$\frac{E_a}{RT_s}\left(\gamma-1\right)t_{is}(T_s)\left(\frac{-6}{\gamma+1}\frac{\dot{D}}{D}-2D\kappa\frac{\gamma-1}{\left(\gamma+1\right)^2}\right)<1. \tag{2.59}$$

This criterion links the quenching of post-shock reactions solely to the dynamics of the lead shock. From the shock speed and curvature, every term in this equation can be calculated knowing the quiescent mixture through which the shock propagates. As shown in section 2.2.5, this criterion can be used to model the quenching of reactions behind a shock due to expansion cooling and recovers the ignition limit calculated using detailed chemistry models. The applicability of this criterion to cellular detonations will be studied further in Chapter 5.

The criterion given by (2.59) is identical with the one derived by Eckett and co-workers by a very different approach for a 1 step model, and by Radulescu & Maxwell; our result also includes the effect of curvature neglected by these previous authors. The derivation of the models presented in sections 2.2.2 and 2.2.3 unified Eckett's 1-step Critical Decay Rate model and Lundstrom & Oppenheim's treatment of induction kinetics and Taylor-Sedov blast waves. In the limit of $\gamma-1=\mathcal{O}(1)$ and high activation energy, an identical solution is obtained from these two independent treatments of post-shock ignition. It was also found that the models yielding an explicit expression for the ignition delay also recovered the behaviour of the implicit 2-step solution in the limit of small ϵ, with the predictions diverging as ϵ ceases to be small. The ignition delay predicted using models derived from simplified chemical kinetics was finally compared to that calculated using

detailed chemistry, and general agreement was observed. The critical ignition asymptote calculated using detailed chemistry agreed particularly well with the one predicted by the implicit 2-step model yet remains compatible with the ignition delay predicted using the models who give an explicit expression for the ignition delay, notably the approximate 2-step linearization of the implicit model in ϵ and the model obtained in the limit of $\zeta = \mathcal{O}(1)$. A strong case can thus be made for the usage of the ignition criterion presented in section 2.2.6, as it is found to offer a good prediction of quenching caused by expansion cooling.

From the evolution of the lead shock velocity and curvature, one can use the Rankine-Hugoniot shock jump equations in conjunction with the shock change equations to describe the evolution of the state of a Lagrangian particle crossing the lead shock, and the expansion of this particle in the post-shock region. Subsequently, one can integrate the energy and species conservation equations in time to study the progression of the post-shock combustion using a detailed chemical kinetics model. As an alternative to integrating the post-shock state using a detailed description of the chemistry, one can study the evolution of the ignition time behind the lead shock using a simplified model derived from a 1-step or 2-step description of the chemical kinetics. To use these simplified models, one must calculate the model parameters ϵ and ζ using the measured dynamics of the lead shock. This methodology will be applied to cellular detonations to study post-shock combustion, and the quenching of the reaction zone occurring within detonation cells.

Chapter 3

Experimental Setup And Apparatus

3.1 Test Mixture Selection

The two fuel mixtures used in experiments were $2H_2 + O_2 + 7Ar$ and $CH_4 + 2O_2$, as these represent both extremes of stability for detonable mixtures as explained in the introduction. Radulescu [9] proposed the χ parameter to characterize the detonability of a reactive mixture, defined as

$$\chi = \frac{t_i}{t_e}\frac{Ea}{RT}, \tag{3.1}$$

with t_i/t_e the ratio of induction to reaction times and Ea/RT the non-dimensional activation energy. The two chosen mixtures have a χ parameter value of 4.7 and 11000, representing a weakly unstable mixture which is insensitive to small changes in temperature and a very unstable mixture which is extremely sensitive to small changes in temperature. These mixtures are chosen because of the extremes they represent, allowing for the observation of generalities across the entire range of detonable mixtures.

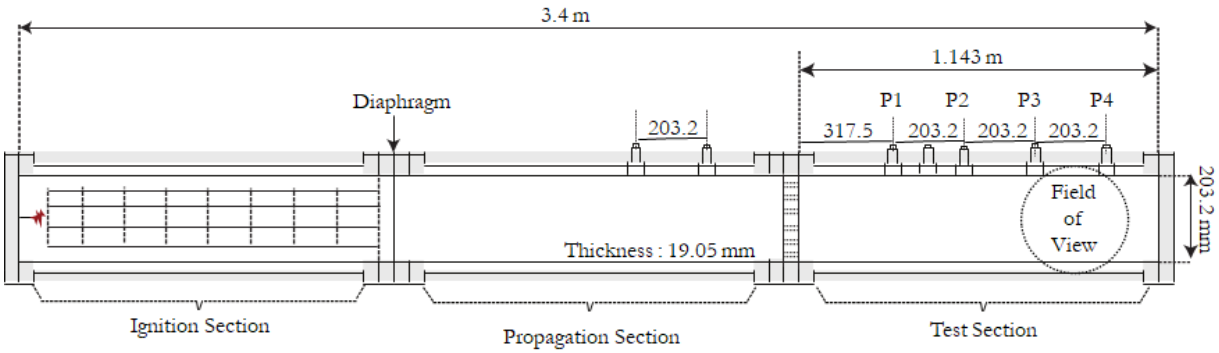

Figure 3.1: Schematic drawing of the shock tube.

3.2 Shock Tube Apparatus

The experiments were performed in a thin shock tube with a rectangular cross-section, as sketched in Figure 3.1. The shock tube is 3.4 m long with a height of 203 mm and a depth of 19 mm, allowing for the visualization of the flow field while minimizing gasdynamic effects in the 3rd dimension. The tube is composed of an ignition, a propagation, and a test section of equal lengths, with aluminium panels placed on the ignition and propagation sections and non-tempered sodium silicate panels placed on the test section to allow visualization of the flow. More details pertaining to the shock tube can be found in Drolet's undergraduate thesis [23].

A high voltage igniter was used to initiate the gas by the means of a spark plug installed in the end-wall of the ignition section. The two 1μF capacitors within this system can be charged to a voltage of 30 kV, and subsequently discharged to deposit a charge of approximately 1 kJ with a deposition time of under 2 μs. A mesh grid placed within the ignition section further promotes the onset of detonation.

3.3 Flow Field Visualization

The smooth-walled propagation section allowed for the detonation to stabilize before being visualized near the end of the test section using Z-type Schlieren photography. More details

on Schlieren photography can be found in Settles' book [24]. The high-speed camera used has a resolution of 384 pixels by 288 pixels at 77481 frames per second for an interframe time of approximately 12.91 μs. Schlieren visualization allows the visualization of the first derivative of density within a test fluid. Changes in density are visualized from its effect on the fluid's refractive index. The light source produces diverging rays of light, which are reflected by the parabolic mirror and directed to the test section as parallel rays. The light is then refracted by the test fluid depending on its index of refraction and thus its density, before being directed to the second mirror. The rays then converge from the second mirror at the knife edge, which blocks half the rays, before again diverging until reaching the camera lens. In a flow without any gradient in density, removing half the focused rays would simply darken the frame. However, due to the ray refraction throughout the test fluid due to density variations, the distorted beams will converge imperfectly, blocking the rays which are focused onto the knife edge. This results in areas which are darker and brighter within the frame representing positive and negative gradients in the fluid density. This gradient is normal to the direction of the knife-edge, thus the vertical knife-edge used in this setup allows the visualization of horizontal density gradients normal to the edge. A compression wave propagating in a given direction can appear as a black or white line, depending on which rays of light are blocked by the knife-edge, as shown in Figure 3.3.

The Schlieren setup was achieved using a vertical knife-edge and a 360 W light source placed opposite to the camera, as shown in Figure 3.2. The knife-edge and light source were placed at the parabolic mirrors' focal length of 2540 mm, whereas the distance between each mirror is minimized. The camera was placed slightly behind the knife-edge, such that the light beams diverge past the knife edge until their diameter is equal to that of the camera lens. The horizontal angle of each mirror is $\theta_c = \theta_l = 8.5^o$, representing the minimum angle required for the light source and camera to be located outside of the flow field. The vertical knife edge was placed to discard half of the light rays such that the incident shock appears as a black line and the reflected shock appears as a white line, akin

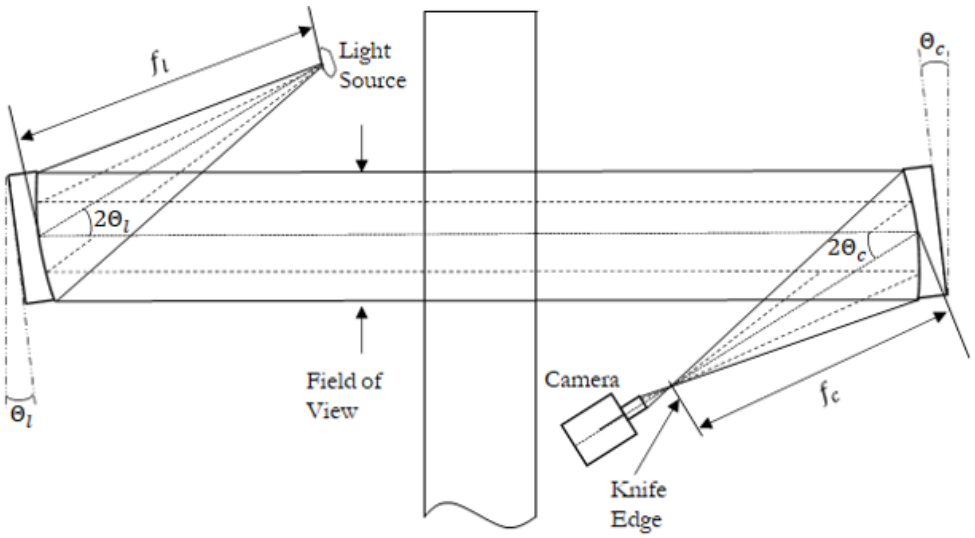

Figure 3.2: Schematic of the Z-type Schlieren imagery setup used.

to that seen in Figure 3.3 b).

3.4 Gaseous Test Mixture Preparation

The two fuel mixtures used in experiments were $2H_2 + O_2 + 7Ar$ and $CH_4 + 2O_2$. The initial conditions of each mixture are shown below in Table 3.1, chosen such that only a single detonation cell forms across the height of the shock tube. The test conditions are the same as those used by Maxwell for stoichiometric methane-oxygen experiments [3], and Xiao for argon-diluted hydrogen-oxygen experiments [1]. A driver gas mixture of $C_2H_4 + 3O_2$ was used to help facilitate the onset of detonation, with initial conditions of $p_0 = 10.34$ kPa (1.5 psi), and $T_0 = 293$ K. Disposable aluminium diaphragms were placed between the initiation and propagation sections to partition the gases as shown in Figure 3.1. These diaphragms, shown in Figure 3.4, are lightly scored to facilitate rupturing by the incoming shock and to promote repeatable rupturing between experiments.

The detonable gaseous mixtures were prepared using the method of partial pressures, and remained in the mixing tank for at least one day before use. The mixing tanks were first evacuated to a pressure of 40 Pa before being filled, with the combustible fuel added

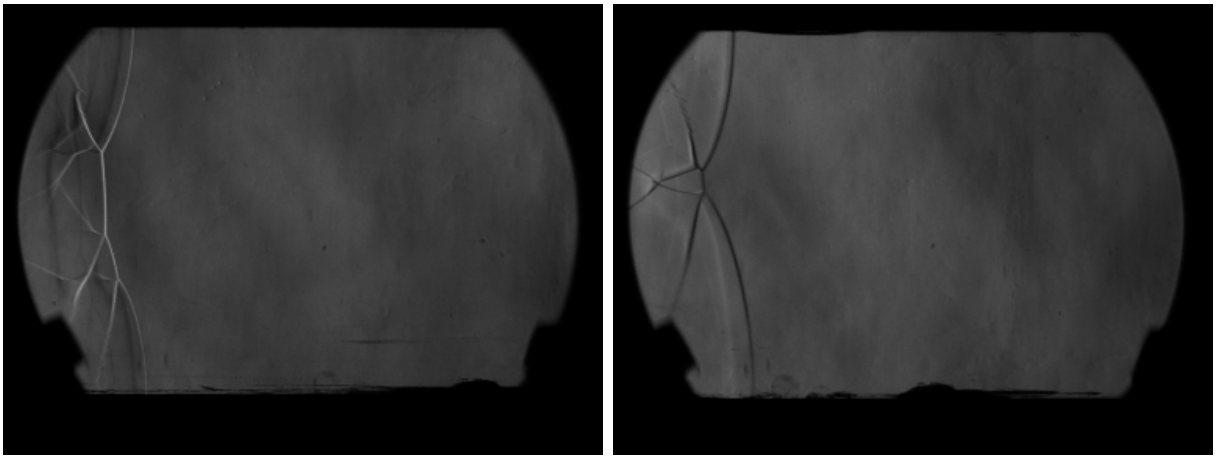

(a) (b)

Figure 3.3: Incident detonation waves propagating in a mixture of argon-diluted hydrogen-oxygen, for opposite placements of the vertical knife edge. In a), the lead shock appears as a positive density gradient in the direction normal to the knife edge and the reaction wave appears as a negative density gradient. In b), the lead shock appears as a negative density gradient in the direction normal to the knife edge and the reaction wave appears as a positive density gradient. Both waves are propagating from left to right.

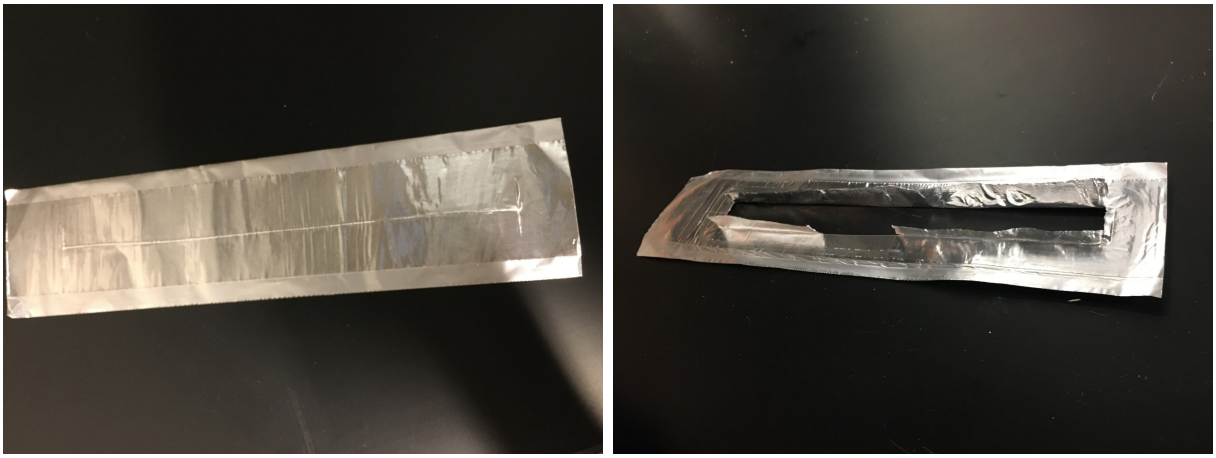

(a) (b)

Figure 3.4: The aluminium diaphragms used to separate the driver gas from the test gas. a) The scoring on the unused diaphragm promoted repeatable rupturing over multiple experiments and reduces the amount of debris which propagates into the test section. b) An expended diaphragm ruptured during an experiment.

Table 3.1: Shock tube experiment test conditions.

Mixture	p_0 (kPa)	T_0 (K)	Interframe Time (μs)	$\bar{D}$ (m/s)	D_{CJ} (m/s)
$CH_4 + 2O_2$	3.5	293	12.97	1870	2244
$2H_2 + O_2 + 7Ar$	4.1	293	12.91	1340	1603

first, the inert diluent second if applicable, and finally the oxidizer added last. Before each experiment, the shock tube is emptied by a vacuum pump to a pressure of at most 80 Pa before being filled with the mixture. The driver section is filled first, followed by the test section.

Chapter 4

Results

4.1 High Speed Visualization Results

Figures 4.1 and 4.2 show two typical high speed visualization sequences of the detonation structure seen in $2H_2 + O_2 + 7Ar$ and $CH_4 + 2O_2$, respectively, with the detonation propagating from left-to-right. The detonation wave seen in Figure 4.1 begins near the end of a cell, with two Mach shocks near each of the walls and an incident shock in the centre, in black. The reaction waves, shown in white, follow the lead shocks, however the distance between the incident shock and the reaction wave is noticeably larger than the distance between the Mach shock and the reaction wave. Proceeding through the following two frames, one notices that the distance between the lead shock and the reaction wave increases. It is interesting to note the effect of the asymmetry on the transverse reaction waves, the topmost being closely coupled to its transverse shock wave whereas the bottom lags behind quite significantly. The second row of frames sees the beginning of the next cell, starting at collision of the triple points. The top and bottom shocks now become the incident shocks, being weaker than the very strong Mach shock formed in the middle of the frame. The reaction wave in the centre follows the Mach shock very closely after the triple point collision, however after around nine frames the induction zone length

begins to quickly increase. Similarly, this length will continuously increase throughout the remainder of the sequence. One can see the Mach shock runs ahead of the incident shocks in the subsequent frames due to the higher velocity associated with the high strength of this wave compared to the incident shock and the triple points. The subsequent collision of the triple points occurs with the walls, out of the field of view.

The evolution of the detonation propagating through the methane-oxygen mixture, shown in Figure 4.2, looks similar to the previous mixture as many key features are shared between these detonations. The sequence begins near the end of a cell, with an incident shock in the centre of the cell bounded by two triple points which propagate towards one another. This incident shock is followed by a reaction zone separated by an increasing induction zone. The first qualitative difference appears in the reaction zone itself, which is more corrugated than the relatively featureless reaction zone seen in the previous mixture. This is similar to the lead shocks, which are again more corrugated than in the first mixture. Upon the collision of the triple points in the third row of frames, a pocket of unburnt gas in the post-shock region detaches from the shock and continues burning through turbulent combustion further behind the lead shock and its coupled reaction wave. The complete set of experimental frames is presented in Appendices A.1 and A.2.

4.2 Measurement of the Shock Dynamics

From the sequence of Schlieren images taken from the experiments, such as those contained in figures 4.1 and 4.2, one can measure the position of the lead shock and its curvature at various points in time. Measurement points are placed on the lead shock at its intersection with the top and bottom walls, and on the reaction wave at these locations. The location of the triple points are also measured, and the cell centreline is taken as halfway between the triple points. The lead shock and reaction zone locations are measured at this centreline. Each measurement point has its x and y coordinates recorded as a pixel distance from the

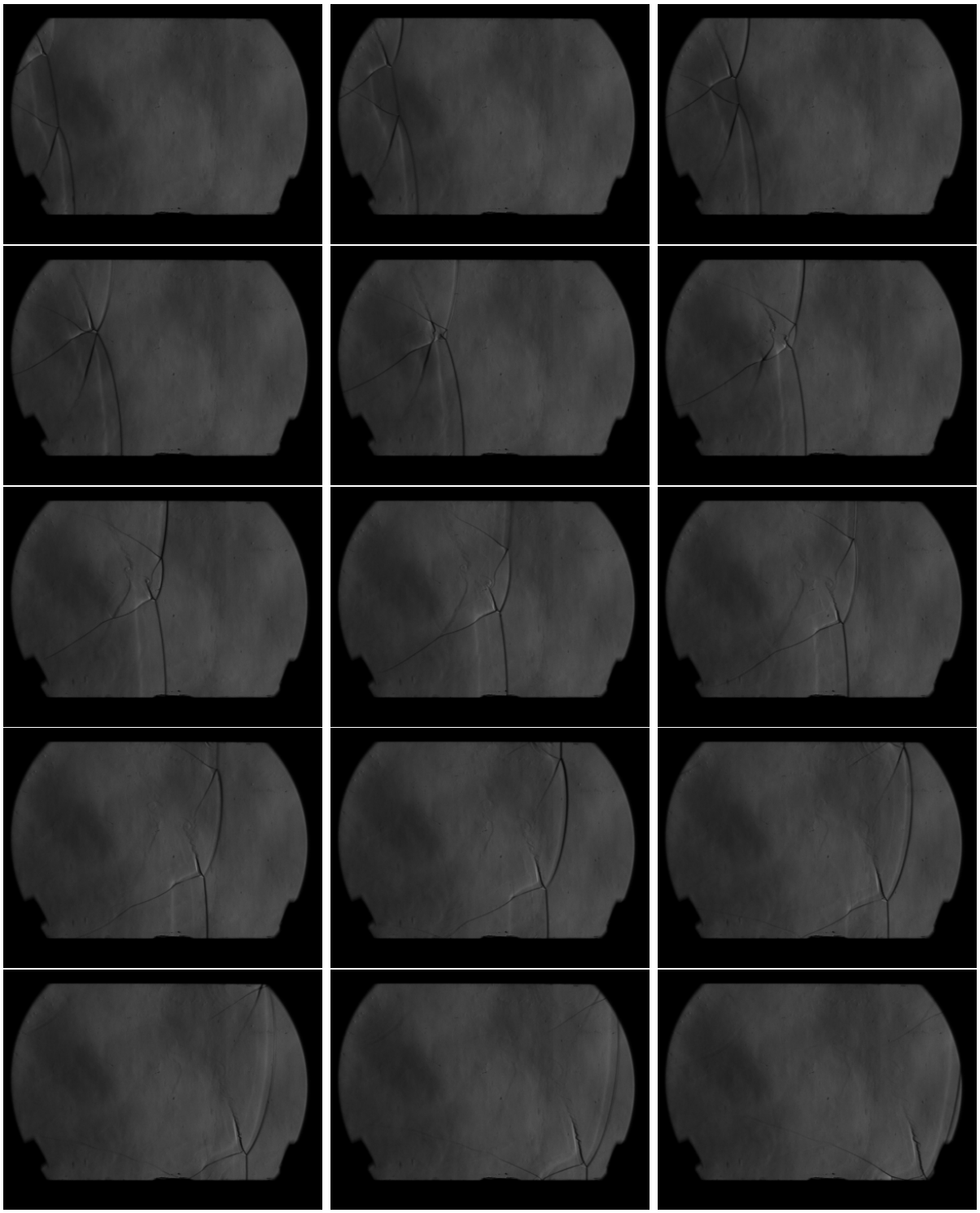

Figure 4.1: Schlieren visualization of the experiment 13_H2 conducted in $2H_2 + O_2 + 7Ar$.

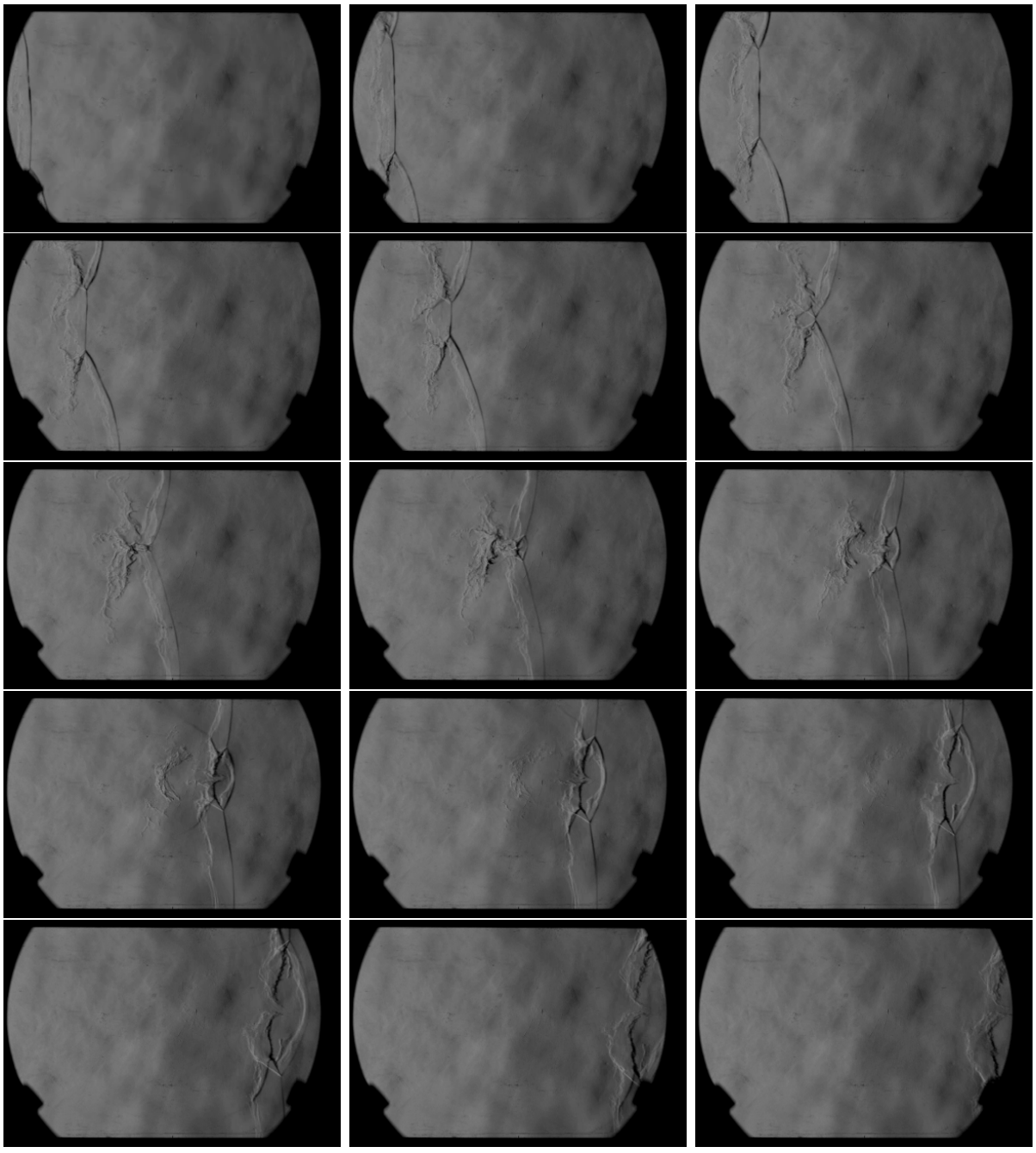

Figure 4.2: Schlieren visualization of experiment 0_CH4 performed in $CH_4 + 2O_2$. Taken from Maxwell and co-workers [3].

upper-left corner of the image. The velocity of the wave in frame n is calculated using a centred difference rule

$$\dot{x}_n = \frac{x_{n+1} - x_{n-1}}{2\Delta t}, \tag{4.1}$$

with the velocity of the waves in the first and last frames being calculated using a forward-difference rule

$$\dot{x}_n = \frac{x_{n+1} - x_n}{\Delta t}, \tag{4.2}$$

and a backward-difference rule

$$\dot{x}_n = \frac{x_n - x_{n-1}}{\Delta t}, \tag{4.3}$$

respectively. In these equations, x_n represents the position of the wave in frame n, x_{n+1} and x_{n-1} represent the position of the wave in the frames preceding and following frame relative to frame n. $\Delta t = \frac{1}{fps}$ is the interframe time of the high speed camera, with the frequency in frames per second (fps) set prior to the experiment. A similar differentiation scheme is used to obtain the acceleration of each wave, replacing $\dot{x}_n$ with $\ddot{x}_n$ in (4.1 - 4.3).

In addition to the velocity of the lead shock, measurements of the curvature of the lead shock at the top wall, centreline, and bottom wall were also taken. A box containing the region of interest was individually measured at the top, centre, and bottom, with each box enclosing the lead shock at these three locations, and this is repeated for each frame. A Python script was written to find the largest negative derivative of pixel intensity within each of these boxes to determine the lead shock position. This interrogation window spans from the wall to the nearest triple point, or from one triple point to the other for the centremost shock. Once transformed into a series of points, an arc of circle was fit over these points using a least-square fitting method with a Levenberg-Marquardt algorithm. An example of such a measurement is shown in Figure 4.3, which properly captures the entirety of the lead shock's position along its arc.

The top wall, centreline, and bottom wall measurements are separated into measure-

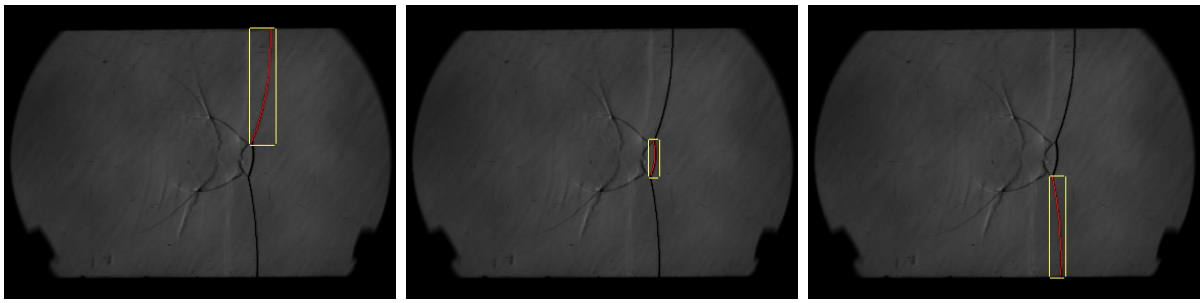

Figure 4.3: Measurement radius of curvature of the lead shock, for an experiment performed in argon-diluted hydrogen. The yellow boxes represent the manually measured regions of interest containing the lead shock, with the measured lead shock overlaid in red on the Schlieren frame.

ment series based on the triple point collision at those locations. Referring to Figure 4.1, the centreline has a series containing the first 4 frames (pre-collision), and a second series containing the remainder of the frames, whereas the top and bottom walls are comprised of a single series each (no data is separated by the triple point collisions as these occurred out-of-frame in this experiment).

4.2.1 Measurement Uncertainty

Due to the nature of measuring experimental results, a certain error is introduced when measuring the velocity and curvature. Figure 4.4 shows an enlarged image obtained through the experiments, showing the pixelation of the shock wave. Considering an exposure time of 0.468 μs, and a spatial resolution of

$$\text{Aspect Ratio} = \frac{\text{Channel Height in mm}}{\text{Channel Height in px}} = \frac{208 \text{ mm}}{235 \text{ px}} = 0.89 \frac{\text{mm}}{\text{px}}, \tag{4.4}$$

the distance that a wave propagates during the exposure time is

$$x_{\text{exposure}} = Dt_{exposure}[\text{mm}] = \frac{Dt_{exposure}}{\text{Aspect Ratio}}[\text{px}]. \tag{4.5}$$

Table 4.1: Exposure distance for varying wave speeds, with an aspect ratio of 0.89.

$D\ \left[\frac{m}{s}\right]$	Exposure Distance [mm]	Exposure Distance [px]
1000	0.468	0.529
1500	0.702	0.793
1900	0.889	1.00

Likewise, this formulation can be used to calculate the measurement uncertainty if one assumes the wave can travel ±1 px in relation to the centremost pixel. In this case, the measurement error is

$$D_{\text{err}} = \frac{x_{\text{err}}}{t_{\text{interframe}}} = \pm 2 \text{ px } 0.89 \frac{\text{mm}}{\text{px}} 77841 \text{ Hz} = \pm 138 \frac{\text{m}}{\text{s}}. \tag{4.6}$$

The results obtained are shown in Table 4.1 for varying wave velocities. The velocity of 1900 m/s is representative of a velocity of the Mach shock near the beginning of a detonation cell, and a full pixel is travelled during the exposure duration. Likewise, velocities of 1000 m/s are representative of those near the end of the cycle, at which point the exposure distance decreases to slightly larger than half a pixel. This can be seen in Figure 4.4 b), in which the very strong Mach shock has a thickness of roughly 3 pixels as it propagates at 1700 m/s whereas the weaker shock at the top wall shown in Figure 4.4 a) also has a 3 pixel thickness at a lower velocity of 1440 m/s. In this latter case, one notices the two outermost pixels are noticeably lighter than the centremost pixel, which is not the case for the higher wave speed. Considering the last measurement taken at the bottom wall shown in Figure 4.4 c), the low velocity shock propagating at 1000 m/s also has a thickness of 3 pixels, however the two outermost pixels are even lighter than those in Figure 4.4 a). The uncertainty associated with measurements of the wave position is thus ±1 px around the centremost pixel regardless of the wave speed. Note that the aspect ratio calculated (4.4) depends on the specific experiment, as the channel height can vary by up to 8 pixels depending on the zoom and placement of the high-speed camera.

When considering the measurements of curvature, the uncertainty primarily comes

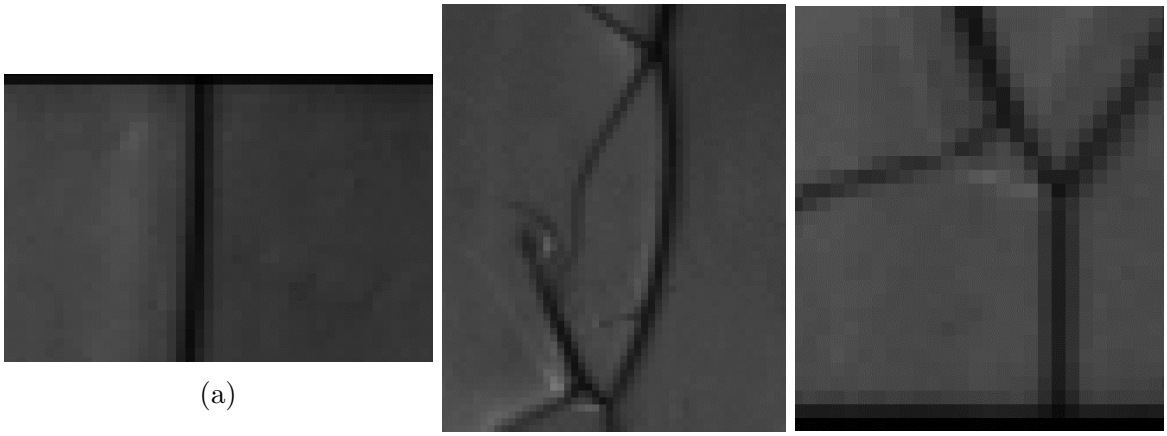

(a) (b) (c)

Figure 4.4: Enlarged view of the shock visualized using Schlieren imagery, for Experiment 0_H2. The waves shown are captured at a) the top wall of frame 7 (1440 m/s), b) the centreline of frame 7 (1700 m/s), c) the bottom wall of frame 14 (1000 m/s). Note a shock thickness of roughly 3 pixels for each image, with the intensity of the neighbouring pixels decreasing with decreasing wave velocities.

from fitting the arc of circle over the lead shock. As mentioned in the previous section, the radius of curvature is obtained by curve-fitting an arc of circle over the lead shock using a Levenberg-Marquardt algorithm implemented in Python. This curve-fitting algorithm also returns the R^2 value representing how well the curve fits the data, and from the Python curve-fitting function one can also obtain the standard error associated with each fit.

4.2.2 Velocity and Curvature Progression

It was necessary to combine the separate series of measurements in such a way that an entire cell cycle can be plotted. As seen in Figures 4.2 and 4.1, the first visualized frame does not coincide with the beginning of a new cell. To reconstruct the cellular cycle, multiple methods were studied. A first method attempted to place each frame based on the ratio of the distance between the triple points and the height of the channel. In this method, the cell would follow the progress of the Mach shock from the triple point collision until the collision with the wall, followed by the progress of the incident shock in the second half of the cell. A second method studied the bottom- and top-half of the channel separately, and

subsequently averaged the results, while following the reconstruction method of the first method.

The method presented below consists of reconstructing the detonation cell by shifting the position of each data series in order to obtain a continuous speed in the cell cycle. This method is possible because the beginning and end of each series of measurements share significant regions of overlapping speeds. Figure 4.5 shows the speed evolution of a reconstructed cell, with each series plotted in a different colour. The error associated with this reconstruction method also agrees with the exponential trendline, and accounts for the reconstruction error. In Figures 4.2 and 4.2, the four measurement series are attributed to the lead shock evolution at the top wall (middle of cell), bottom wall (middle of cell), centreline before the triple point collision (end of cell), and centreline after the triple point collision (beginning of cell). Experiments 5_H2 and 11_H2 has a collision of a triple point with the top and bottom walls, thus separating these measurement series at the collision is necessary.

Once the cell is reconstructed, one can curve-fit the progression of the speed and the curvature over the cell distance. These fits are shown in Figures 4.5 and 4.6. The exponential functions

$$D = D_0 e^{-ax}, \tag{4.7}$$

and

$$\kappa = \kappa_0 e^{-bx}, \tag{4.8}$$

are chosen for these curve-fits as they are found to offer better fits than 3rd order polynomial and power law fits. The choice of using an exponential decay is also supported by the findings of Jackson and co-workers [25], where an exponential speed decay is found. One notices the generally good agreement between the fitted curves and the measured data, however a linear decay would have fit the data equally well. The parameters of the curve fits are shown in tables 4.2 along with the R-squared value associated to each fit. When

Table 4.2: Curvature and shock speed curve fitting parameters.

Experiment	D_0 (m/s)	a	R^2_D	κ_0 (1/m)	b	R^2_κ
0_H2	1783	1.8	0.92	0.02	9.1	0.95
5_H2	1902	1.9	0.93	0.029	10.9	0.92
11_H2	1812	2.1	0.96	0.027	14.3	0.68
13_H2	1849	1.8	0.96	0.026	13.6	0.79
18_H2	1806	1.7	0.97	0.023	9.9	0.80
19_H2	1934	3.0	0.95	0.039	14.6	0.68
0_CH4	2534	1.5	0.93	0.048	10.1	0.86

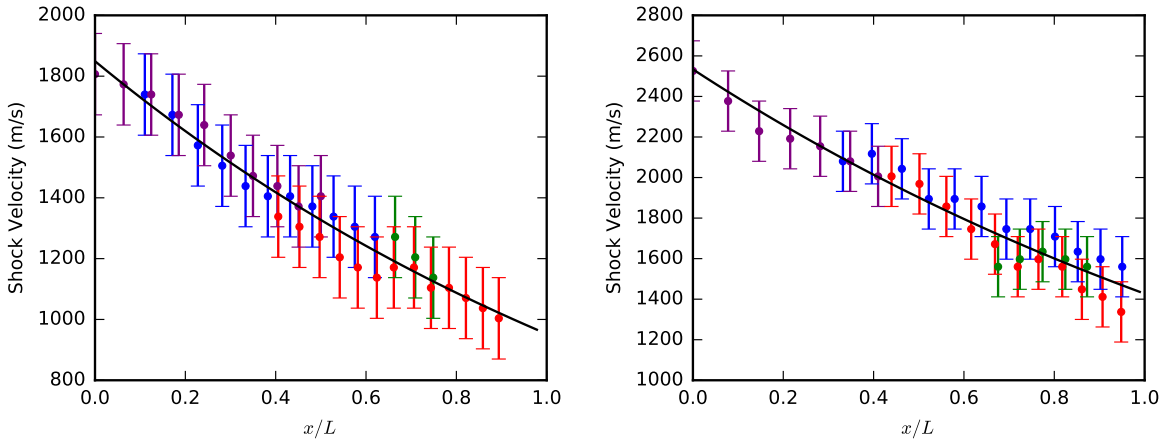

(a) (b)

Figure 4.5: The shock speed evolution over a detonation cell, with the exponential curve-fit traced in black. For experiments a) 13_H2 and b) 0_CH4. The colour of each point represents their measurement series - blue : top wall, red : bottom wall, green : centreline pre-collision, purple : centreline post-collision.

fitting the evolution of curvature over the cell, the very large curvature values at the beginning of the cell are removed as outliers. This is in part to the difficulty of measuring a radius on the order of millimetres from the pixelated frames reducing the meaningfulness of such measurement points, and in part due to these points being outliers due to their extremely large value which is frequently on the order of meters. In comparison to this, the remainder of the curvature values very rarely reach an order of 10^{-1} m. The fitted curve under-predicts the curvature at the beginning of the cell regardless of the inclusion of these points in the fit, therefore an accurate reconstruction of the evolution of curvature over the remainder of the cell is preferred.

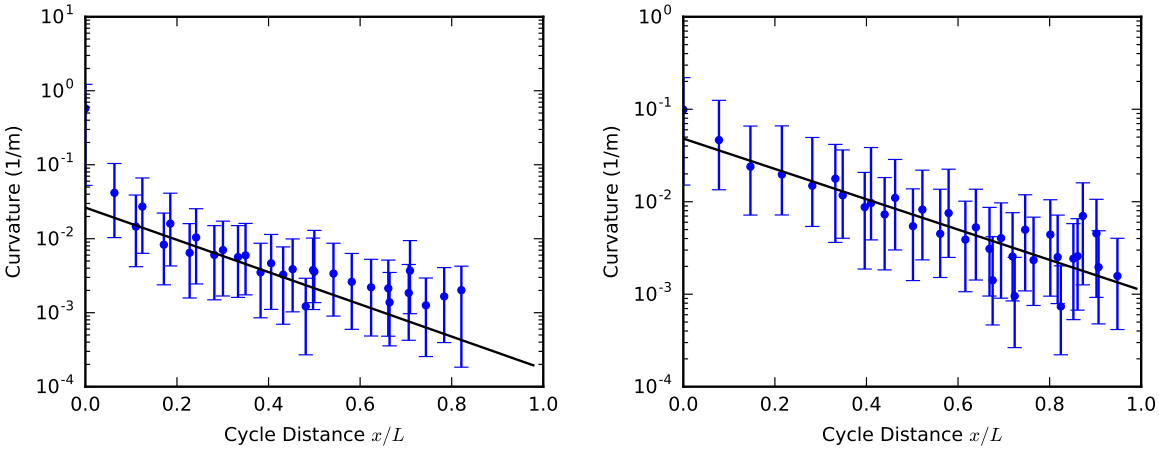

(a) (b)

Figure 4.6: The evolution of the logarithm of curvature over a detonation cell, with the exponential curve-fit traced in black. For experiments a) 13_H2 and b) 0_CH4. One notices the large early-cell curvature value of 0.6m at x=0 in a), which was not included in the fit.

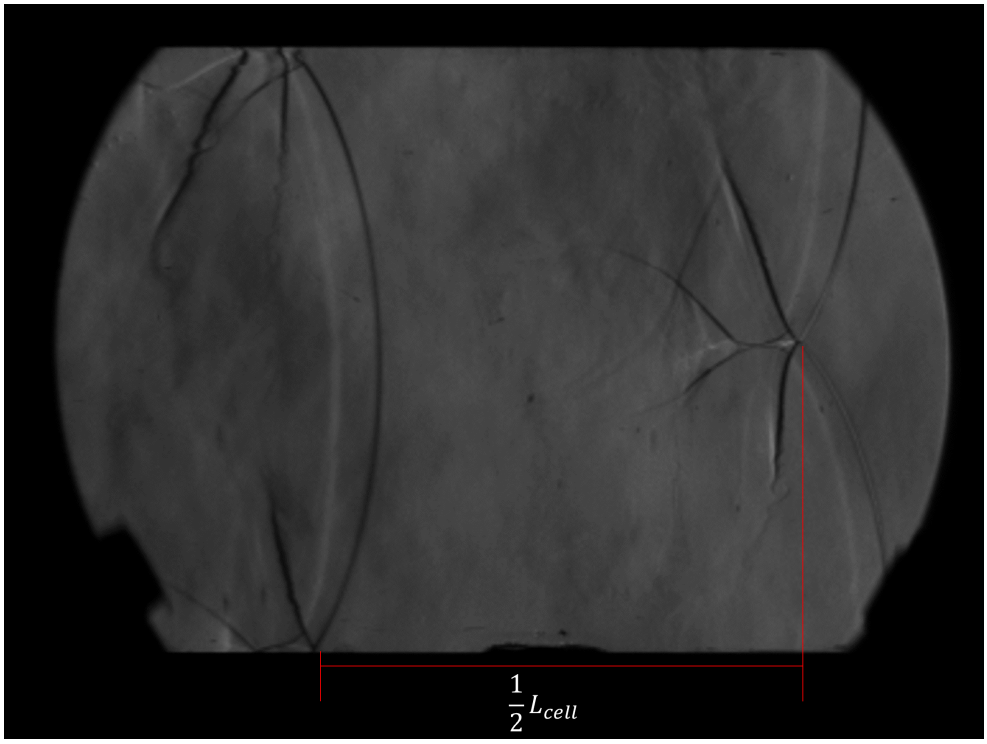

Figure 4.7: Example of the measurement of the cell length from experimental frames.

4.2.3 Cell Length

By the assumption of lateral symmetry in detonation cells, the cycle length is determined by measuring the half-length of the cell from the collision of the triple points at the centreline and at the wall, as shown in Figure 4.7. To compare the cells across all of the experiments, the spatial distances are normalized using the measured cyclic length L_{cell} of each experiment. Once normalized, the shock speed and curvature can be plotted over a cycle distance ranging from 0 at the beginning of the cycle to 1 at its end, seen in figures 4.9 and 4.8. These figures contain a comparison of all the experiments performed in the argon-diluted hydrogen-oxygen mixture, and plots a curve representative of all the data. This average curve is found to closely follow the evolution of the experiment 13_H2.

Normalizing the distance by the cell length allows for a meaningful comparison of the evolution of variables throughout the cellular cycle between experiments. One sees that despite the quantitative differences between experiments, similar trends are followed with a deviation around the average speed of $\pm 13\%$ and $\pm 30\%$ in the velocities at the beginning and end of the cycle, respectively. Similarly, the curvature evolution of each experiment follows a decreasing trend, however the deviation associated with this evolution is significantly higher as measuring experimental curvature accurately remains a challenge. It is interesting to note that experiments which begin with higher velocities (19_H2 for example), tend to decay at noticeably higher rates than cells with lower peak velocities, with two experiments reaching velocities under 800 m/s at the end of the cell.

4.2.4 Average Propagation Speed and Velocity Deficit

The average propagation velocity of the detonation cell can be calculated either from the curve-fit velocity evolution presented in section 4.2.2, or by directly measuring the average velocity from the visualized frames. The first method consists of finding the average of the

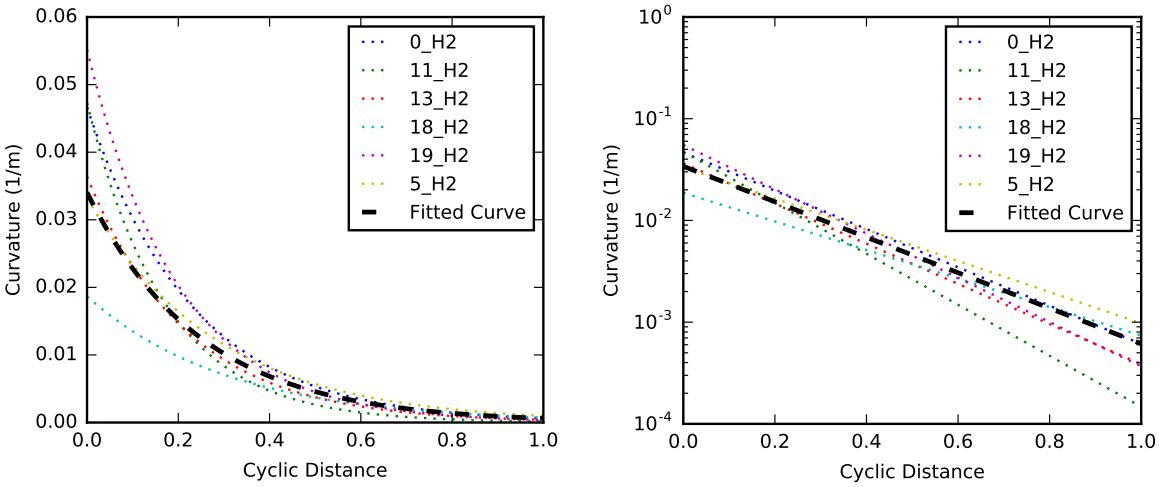

Figure 4.8: The curve-fit evolution of the curvature plotted over the cell length, for the experiments performed in argon-diluted hydrogen-oxygen. A curve fit representative of the average evolution of curvature is also presented.

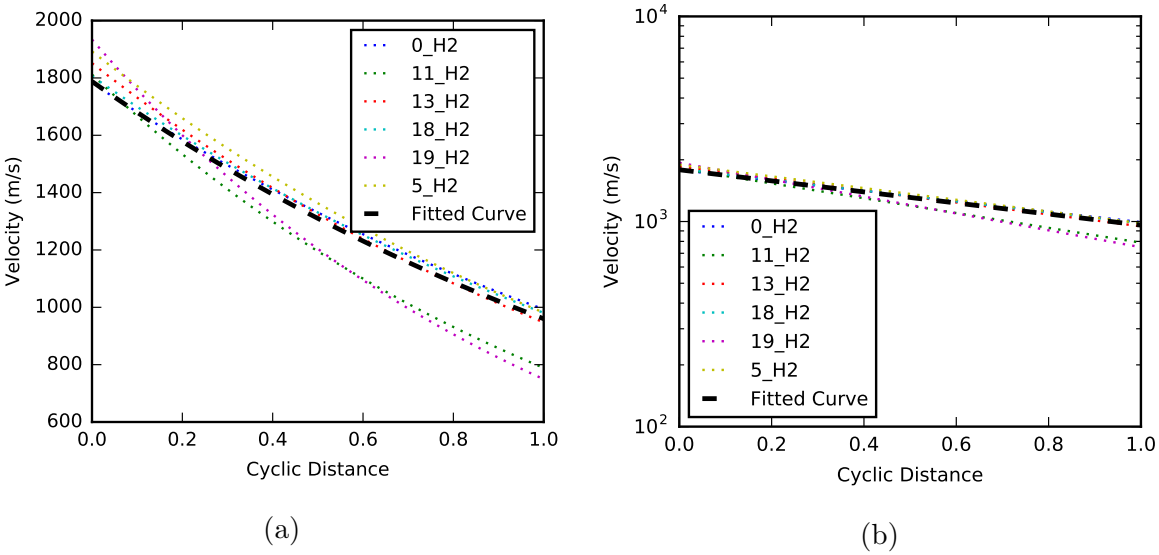

Figure 4.9: The curve-fit evolution of the lead shock velocity plotted over the cell length, for the experiments performed in argon-diluted hydrogen-oxygen. A curve fit representative of the average evolution of the lead shock is also presented.

exponential fit presented in section 4.2.2. This is found from the expression

$$\bar{D} = \frac{L_{cell} - 0}{t_{cell} - 0}, \tag{4.9}$$

with t_{cell} found by integrating the velocity

$$\frac{dx}{dt} = D(x) = D_0 e^{-ax}, \tag{4.10}$$

which can be recast as

$$\int_0^{L_{cell}} \frac{dx}{D_0 e^{-ax}} = \int_0^{t_{cell}} dt. \tag{4.11}$$

Solving this integral yields

$$t_{cell} = \frac{1}{a}\left[\frac{1}{D(L_{cell})} - \frac{1}{D_0}\right]. \tag{4.12}$$

This cell time gives an expression for the average speed of

$$\bar{D} = aL_{cell}\frac{D_L D_0}{D_0 - D_L}, \tag{4.13}$$

with $D_L = D(L_{cell})$. For the experiment 0_H2, an average velocity of 1310 m/s is found from $D_0 = 1783$ m/s, $a = 1.8$, and $L_{cell} = 0.325$ m/s taken from Table 4.2 and $D_L = 993$ m/s calculated from (4.7).

Another method to verify the accuracy of the fit curves is available by measuring an average propagation velocity directly from the experimental frames. For this measurement, an early frame near a triple point collision is chosen for an unambiguous measurement of the lead shock location. If a frame is chosen containing a wave slightly before the triple point collision, the second frame chosen will also contain a wave slightly before a triple point collision. The height of the incident shock/Mach shock should be similar in both frames. The location of the wave is measured for the top and bottom wall independently, as well as the timespan between the frames associated with each measurement. An average

Table 4.3: Detonation cell scales and average propagation velocities.

Experiment	$\bar{D}_{fit}$ (m/s)	$\bar{D}_{meas}$ (m/s)	$\frac{\bar{D}_{meas}}{D_{CJ\ fit}}$	$\frac{\bar{D}_{meas}}{D_{CJ\ meas}}$	L_{cell} (m)	t_{cell} (s)
0_H2	1310	1280	0.82	0.80	0.325	0.00025
5_H2	1330	1410	0.83	0.88	0.357	0.00025
11_H2	1160	1320	0.72	0.82	0.396	0.00030
13_H2	1300	1400	0.81	0.87	0.368	0.00026
18_H2	1310	1380	0.82	0.86	0.355	0.00026
19_H2	1130	1240	0.71	0.78	0.331	0.00027
0_CH4	1880	1870	0.84	0.83	0.374	0.00020

propagation velocity for the top and bottom half of the cell is calculated as

$$\bar{D} = \frac{x_2 - x_1}{\Delta t}, \tag{4.14}$$

and subsequently averaged to obtain the average propagation velocity of the overall wave. This measurement of velocity is also shown in Table 4.3, with an average velocity of 1280 m/s measured for experiment 0_H2.

The average propagation velocity found using both methods are within 138 m/s of one another for every experiment, which is the uncertainty associated with measurements of velocity. Xiao and co-workers measured the average velocity using a time-of-arrival method with wall-mounted pressure transducers separated by a distance of over 1 meter, reporting an average velocity deficit of $0.83D_{CJ}$ for 0_H2 [1]. Maxwell reports a velocity deficit of $0.83D_{CJ}$ for experiment 0_CH_4 [3]. Both these reported velocity deficits are in excellent agreement with both measurements presented for calculating the velocity deficit, and further validates the method used to reconstruct the detonation cells presented in section 4.2.2.

4.3 Shock Change Equation

The shock change equation contains two competing terms, best seen under the assumption of a strong shock (2.13). As previously discussed in section 2.1, the rate of lateral strain due to changing curvature and the shock unsteadiness terms are only a function of the initial state, and the velocity and curvature of the shock front. We can now compare them throughout the cycle. At the beginning of the cycle, the ratio of both terms begins on the order of 1, with the unsteadiness term being slightly larger than the rate of lateral strain of the lead shock. This is the case for both studied mixtures. The rate of lateral strain quickly decreases to become smaller by an order of magnitude at around half the cycle length as seen in Figure 4.10. Horizontal dotted lines are plotted to show the critical ratio of these terms at which quenching of the post-shock reaction occurs. The quenching of the post-shock reactions will be discussed in more details in section 5.1.

From Figure 4.10, one notices that quenching of the post-shock reaction occurs in both mixtures when the rate of lateral strain is an order of magnitude smaller than the shock unsteadiness, with the critical rate being a factor of 3 larger in the methane-oxygen mixture. This may be linked to the highly unstable mixture's higher sensitivity to fluctuations in temperature than the weakly unstable mixture. As quenching occurs in both mixtures when the magnitude of the lateral strain rate becomes much smaller than the unsteadiness, one can infer that the quenching mechanism is not solely a function of the decay of the strength of the lead shock. The change in lead shock curvature plays an important role in the ignition processes. However, as the shock flattens and the rate of lateral strain becomes negligible in the latter portion of the cycle, the curvature ceases to be an important effect in controlling the dynamics of the lead shock, which is then dominated by the lead shock's decay rate.

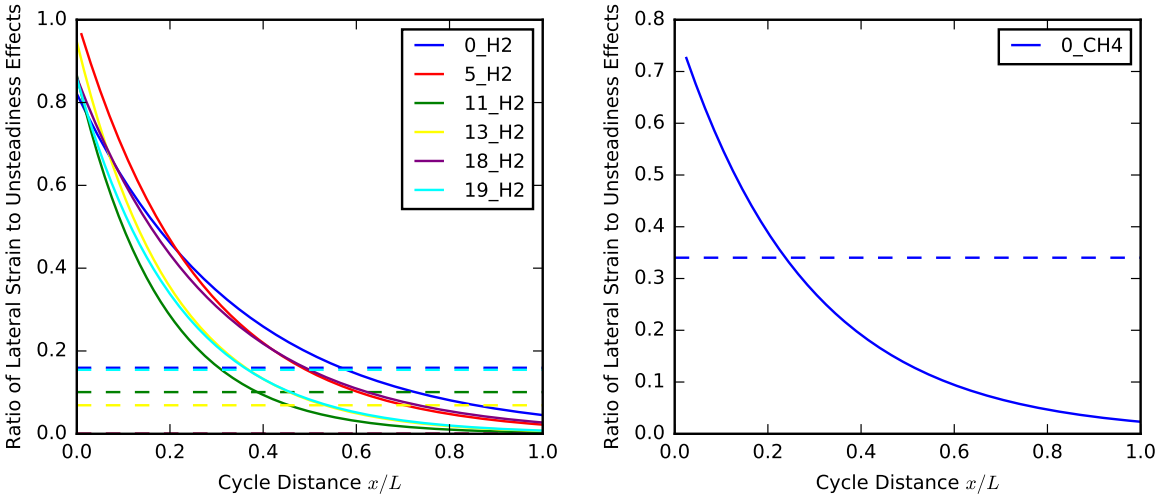

(a) (b)

Figure 4.10: Ratio of lateral strain rate to unsteadiness terms, with the horizontal intersection with the critical ignition limit of each cycle as a dotted line of the same colour. For a) argon-diluted hydrogen-oxygen, and b) stoichiometric methane-oxygen.

Chapter 5

Discussion

5.1 Ignition with Full Chemistry

We now study the evolution of the ignition process occurring in the post-shock state throughout a detonation cell cycle. As described in section 2.2.1, the initial state and the volumetric expansion rate of a Lagrangian particle crossing the lead shock at a given instant is calculated from the Rankine-Hugoniot shock jump equations and the shock change equations, respectively. The required measurements to describe the dynamics of the lead shock were presented in section 4.2, i.e., the lead shock speed, shock decay rate, and its curvature. The detonation cell was reconstructed and lead shock dynamics were curve-fit in section 4.2.2. This reconstruction of the detonation cell and fitting of the shock dynamics allows one to calculate the post-shock state and volumetric expansion for any particle path which crosses the lead shock.

Figures 5.1 a) and b) show the evolution of temperature along a particle path as a function of time, for particles crossing the lead shock at increasing cell distances. Two general behaviours appear, which depend on the cell distance at which the particle path crosses the lead shock - quenching of the post-shock reactions occurring later in the cell and the occurrence of an ignition process occurring early in the cell. These two behaviours

are separated by a critical path, which is taken as the final particle path which sees the occurrence of ignition in the post-shock region. Studying the particle paths which cross the lead shock early in the cell cycle, one sees that the post-shock temperature slowly decreases throughout the induction zone until a drastic increase in temperature occurs. This temperature increase is large enough to cause the thermal runaway associated with ignition events. Once the energy has been released, the predicted temperature slowly decreases until either the maximum integration time is reached or until the temperature decreases to the 323 K temperature floor of the combustor simulation. This behaviour is similar to the evolution of temperature shown in Figure 2.1 a), associated with a small non-zero volumetric expansion rate. As the volumetric expansion rate increases, the peak temperature decreases and time elapsed until the peak temperature is attained also increases. The rate at which the temperature decays prior to ignition and after the completion of the combustion process also increases with the post-shock expansion rate.

When the post-shock expansion is increased past a critical threshold, as in the largest volumetric expansion rate plotted in Figure 2.1, the second behaviour of quenched reactions is seen. This begins with the particle path plotted in bold purple in Figures 5.1 a) and b), and continues for the remainder of the cell. Particle paths with quenched post-shock reactions see a decreasing temperature throughout the post-shock region due to the absence of the thermal runaway process which occurs during ignition. The rate of energy release is unable to overcome the expansion cooling imposed on the particle in the post-shock state. This decrease in temperature continues until the 323 K temperature floor of the combustor simulation is reached.

The critical path, plotted as a bold black curve in Figure 5.1, represents the last particle path along which a Lagrangian particle crossing the lead shock will ignite. This critical path shares the characteristic rise in temperature occurring during ignition with all previous particle paths in the cell. Due to the substantial effect of expansion cooling compared to previous particle paths which were subjected to smaller volumetric expansion rates in

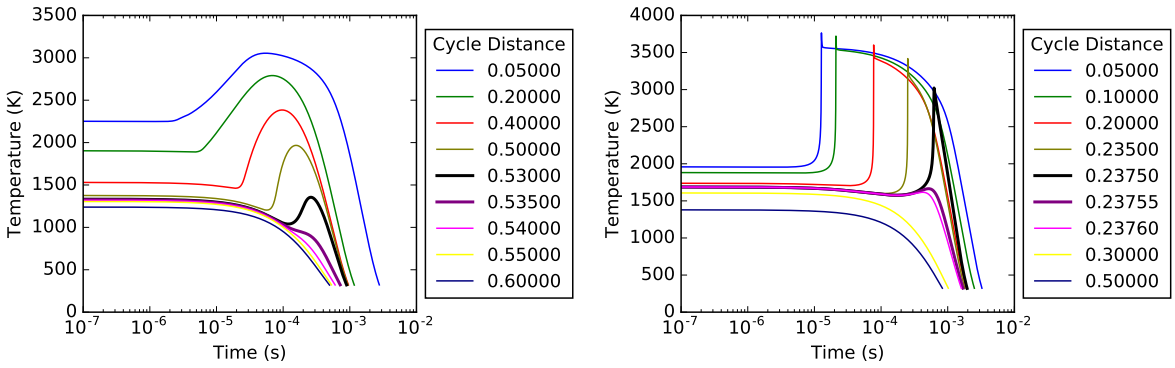

(a) (b)

Figure 5.1: Plot of the evolution in time of the temperature in the post-shock state, for selected particle paths labelled at the location of crossing of the lead shock. Plotted experiments are 13_H2 and 0_CH4, for which the critical ignition limit is associated with the particle paths $0.5300L_{cell}$ and $0.2375L_{cell}$.

the post-shock region, this critical path is associated to the longest ignition delay of any particle path crossing the lead shock. The change in behaviour occurs very abruptly after this critical path, with a particle path crossing the lead shock at a distance of $0.005L_{cell}$ after the critical path clearly having quenched post-shock reactions, as seen in Figure 5.1.

Similar to the evolution of temperature, the evolution of the rate of heat release, or thermicity, over a detonation cell can also give insight as to the ignition behaviour along a particle path. Figure 5.2 shows the evolution of thermicity, as a function of time along the same particle paths as plotted in Figure 5.1. The thermicity associated with particle paths crossing the lead shock early in the cell sees a significant release of heat occurring around the ignition point, with a peak thermicity generally over 4-orders of magnitude greater than the pre-ignition thermicity. The peak thermicity appears as a very sharp increase in the highly unstable mixture, whereas this high heat release rate occurs over much longer times in weakly unstable mixtures. The peak thermicity is the most convincing method of tracking the ignition time of a particle, and this tracking method will be used for the remainder of this work. The peak thermicity attained along particle paths associated with quenched post-shock reactions is orders of magnitude lower than the peak thermicity attained along particle paths crossing the lead shock prior to the critical path.

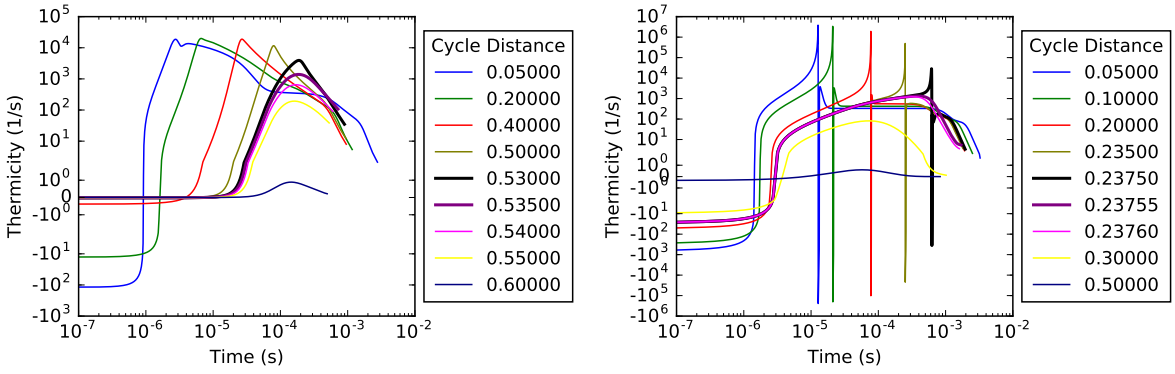

(a) (b)

Figure 5.2: Plot of the evolution in time of the thermicity in the post-shock state, for selected particle paths labelled at the location of crossing of the lead shock. Plotted experiments are 13_H2 and 0_CH4, for which the critical ignition limit is associated with the particle paths $0.5300L_{cell}$ and $0.2375L_{cell}$.

The evolution of thermicity allows for a clear differentiation of behaviour between two particle paths, but it alone cannot be used to determine the quenching along a particle path. This is especially true for ignition in argon-diluted hydrogen-oxygen, as the peak thermicity of the critical path ($\mathcal{O}(10^4)$) is similar to the following particle paths with quenched post-shock reactions ($\mathcal{O}(10^3)$). If one compares Figures 5.2 a) and b), despite a peak thermicity on the order of 10^4 being associated with ignition in argon-diluted hydrogen-oxygen, a similar peak thermicity value is associated with quenching in methane-oxygen. This reinforces the need for another method for determining whether ignition occurs along a particle path.

A more convincing method to differentiate between particle paths associated with post-shock ignition and quenching appears when studying the evolution of the mass fractions of various chemical species as a function of time in the post-shock state. Figure 5.3 shows the evolution of the mass fraction of the fuel specie, be it H_2 in a) or CH_4 in b), shown for the same particle paths as previously studied in this chapter. The difference between the particle paths which ignite and those which are quenched is very striking, with the reactant mass fraction suddenly decreasing during the ignition process. By contrast, particle paths

associated with quenched reactions do not have this sudden drop in reactant mass fraction, with the final mass fraction of the reactants remaining comparable to the initial mass fraction of the reactants in the post-shock state. The critical path evolves similar to the earlier particle paths, reinforcing that ignition occurs along this selected path. Conversely, the following particle path (plotted in bold purple) with quenched post-shock reactions behaves as the subsequent particle paths reinforcing that no ignition occurs along this particle path.

Intermediate species, such as H, O, and the radical OH, are very reactive and essential in the chain-branching reactions which can cause the overall chemical reaction to occur very rapidly. Intermediate species are consumed during chain-propagating and chain-termination elementary reactions. Previous studies have used the formation of OH radical as indicative of ignition. A relevant example which is applicable to both currently-studied mixtures is the elementary reaction

$$\mathrm{H} + \mathrm{OH} + X \longrightarrow \mathrm{H_2O} + X, \tag{5.1}$$

in which two intermediate species are consumed to form a product specie in the presence of a third molecule X. The evolution of the mass fraction of the intermediate radical OH is shown in Figure 5.4. A noticeable increase in the OH mass fraction occurs during ignition. The particle paths associated with ignition in Figure 5.4 a) have a peak mass fraction on the order of 10^{-2} before decreasing near the end of the simulation. Meanwhile, the mass fraction of OH along particle paths with quenched post-shock reactions remain fairly insignificant, however they show that the radical is not consumed by chain-branching or chain-termination elementary reactions. A similar trend is observed in Figure 5.4 b). Particle paths along which an ignition process occurs have a very sharp increase in the OH mass fraction, reaching an order of 10^{-1} before being consumed later in the simulation. Conversely, the particle paths associated with quenching have insignificant OH mass

fractions, which are not consumed by chain-branching or chain-termination elementary reactions.

The final species which can be studied is the products of reaction, notably CO_2 in the case of hydrocarbon combustion and H_2O. The evolution in time of the mass fraction of a product specie, H_2O, is shown in Figure 5.5. In both hydrogen and methane combustion, the product mass fraction begins at a negligible level, and increases with time. Lagrangian particles which undergo an ignition process have a product mass fraction which becomes very significant, reaching an order of 10^{-1} to 1. Additionally, one notices an overlapping of product mass fraction curves for the cases with ignition, due to near complete combustion, whereas the product mass fraction is distinctly lower in absence of ignition.

A very convincing argument for ignition or quenching along a particle path can be made by comparing the mass fraction of the product and reactant species. In the presence of ignition, the mass fraction of the products will exceed that of the reactants by the end of the integration. This is not the case when the reactions are quenched, as the reactant mass fraction will remain much larger than that of the products throughout the integrated post-shock state. The first quenched particle path has a final product mass fraction on the order of 10^{-2} in the hydrogen system and 10^{-1} in the methane system, compared to a final reactant mass fraction on the order of 10^{-1} in the hydrogen system and 10^{-1} in the methane system. In contrast, the critical path has a product mass fraction on the order of 10^{-1} for both the hydrogen and methane systems, compared to a final reactant mass fraction on the order of 10^{-2} and 10^{-7} for the hydrogen system and methane system, respectively.

The designation of a specific particle path as the critical path was not convincing when solely studying the evolution of temperature or thermicity in the post-shock state. In Figure 5.1 b), a rise in temperature still occurs for the first post-critical path associated with $x = 0.23755L_{cell}$, whereas the peak thermicity attained by the first post-critical path associated with $x = 0.535L_{cell}$ in Figure 5.2 a) is comparable to the peak thermicity attained

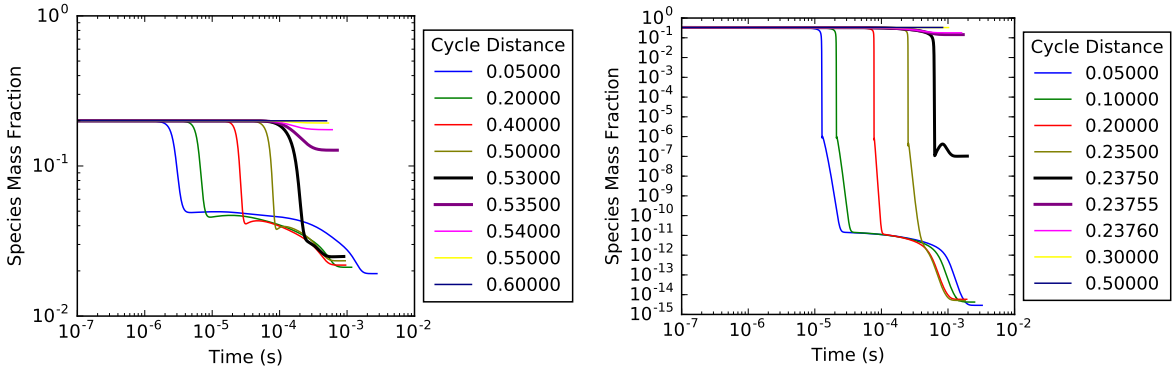

(a) (b)

Figure 5.3: The evolution in time of the fuel species mass fraction (H_2 and CH_4), shown for selected particle paths. Plotted experiments are a) 13_H2 and b) 0_CH4, for which the critical ignition limit is associated with the particle paths $0.5300L_{cell}$ and $0.2375L_{cell}$.

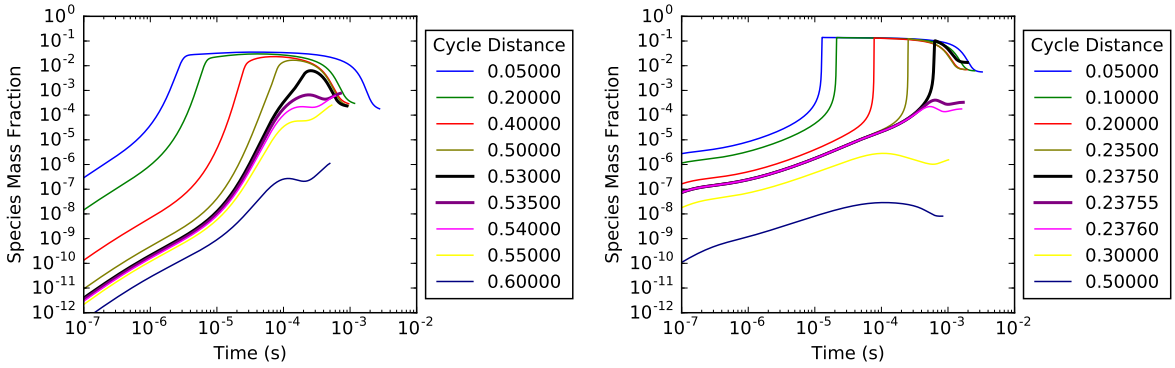

(a) (b)

Figure 5.4: The evolution in time of an intermediate species mass fraction (OH), shown for selected particle paths. Plotted experiments are a) 13_H2 and b) 0_CH4, for which the critical ignition limit is associated with the particle paths $0.5300L_{cell}$ and $0.2375L_{cell}$.

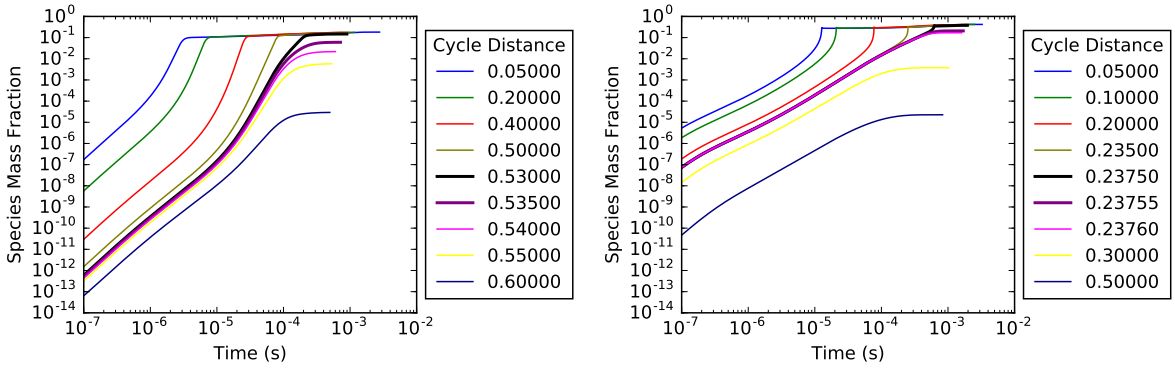

(a) (b)

Figure 5.5: The evolution in time of a product species mass fraction (H_2O), shown for selected particle paths. Plotted experiments are a) 13_H2 and b) 0_CH4, for which the critical ignition limit is associated with the particle paths $0.5300L_{cell}$ and $0.2375L_{cell}$.

along the critical path. However, when studying the evolution of the species mass fraction along these two paths, it becomes very clear that a Lagrangian particle propagating along the critical path ignites whereas a particle propagating along the first post-critical path does not. The occurrence of ignition along the critical path is supported by 1) the final mass fraction of the fuel species decreasing by an order of magnitude during ignition, 2) the mass fraction of the intermediate species increasing to a non-negligible level during the chain-initiation and chain-branching elementary reactions and subsequently decreasing during chain-termination elementary reactions which sees the formation of product species, and 3) the final mass fraction of the products of combustion exceeding the final mass fraction of the reactants. None of these statements hold true when studying a particle path which is linked to quenched post-shock reactions, despite certain similarities between the evolution of temperature or thermicity along these selected particle paths.

5.1.1 Critical Ignition

Throughout the Cantera simulations, the peak rate of heat release is saved as a tracker for the ignition time. This remains the most convincing method of measuring the ignition delay, however studying the evolution of the species mass fraction remains necessary to

distinguish between igniting and quenched particle paths. The ignition delay is plotted in Figure 5.6 over the length of a detonation cell, showing an ever-increasing ignition delay as the lead shock weakens. The ignition delay without expansion, t_{is}, is plotted alongside the ignition delay of a particle subjected to a volumetric expansion in the post-shock state, t_{ig}. The effect of expansion cooling is clearly seen as a vertical asymptote within the first half of the detonation cell. This asymptote represents the critical ignition limit of the cell, taken as the last particle path along which a Lagrangian particle will ignite. This clearly separates the cellular cycle into two distinct sections with the very different ignition behaviours seen in section 5.1, be it an ignition regime prior to the critical ignition limit and a quenching regime after the limit. Physically, the compression of a particle caused by crossing the lead shock prior to this asymptote is strong enough to induce ignition, despite the expansion cooling affecting the particle throughout the post-shock region. Past this ignition asymptote, the lead shock has weakened and the volumetric expansion has increased to the point that the compression offered by the lead shock is unable to overcome the expansion cooling felt by a Lagrangian particle crossing the lead shock and induce auto-ignition. In experiments, secondary initiation mechanisms are necessary to ensure the ignition of these gases, such as the turbulent mixing of unburnt gases and heating by transverse shocks as seen in the experimental frames presented in section 4.1. The average critical ignition limit of the experiments performed in argon-diluted hydrogen-oxygen is situated around 53% of the cell cycle and around 24% of the cell cycle for the studied methane-oxygen experiment. This agrees with previous findings of quenching within the first half of the cell cycle. This also confirms that an accurate model for detonations must consider the lower heat release rate of secondary combustion mechanisms, as these mechanisms govern the energy release for the majority of the detonation cell.

Numerical artefacts may appear when measuring the time to peak thermicity past the critical ignition limit, in the quenched reaction region. These are caused by the difficulties associated with capturing the peak thermicity during numerical integrations of the post-

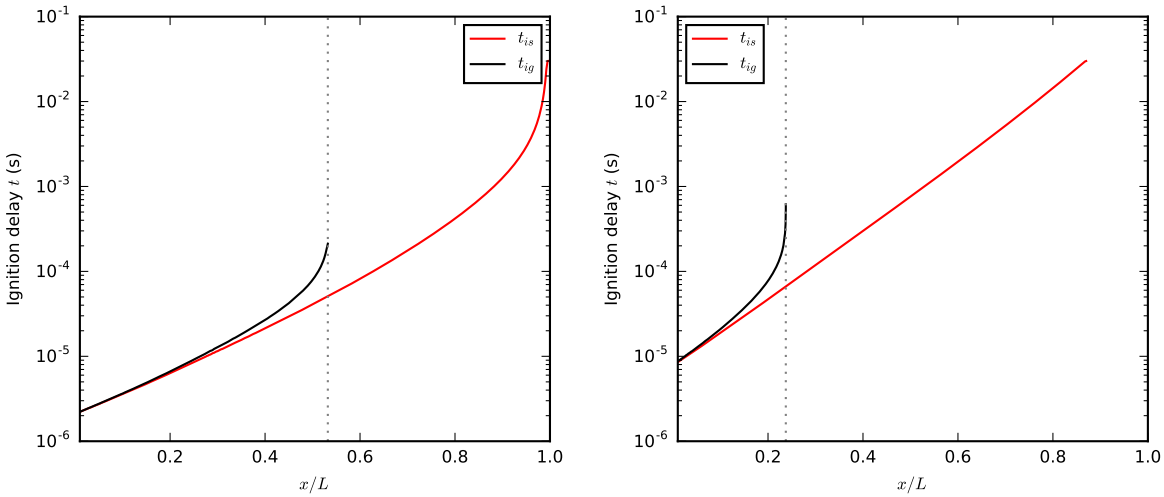

(a) (b)

Figure 5.6: Evolution of the ignition delay over a detonation cell, with the critical ignition limit appearing as a vertical asymptote beyond which quenching of the post-shock ignition occurs. The effect of expansion cooling on the ignition delay is clearly seen when comparing the calculated ignition delays in the presence and absence of post-shock expansion. Plotted experiments are a) 13_H2, and b) 0_CH4.

shock state for Lagrangian particles whose post-shock reactions are quenched. The time elapsed until the peak thermicity decreases immediately after the critical ignition limit is reached, and subsequent difficulties in capturing the peak thermicity appear once it becomes difficult to distinguish it from average thermicity. This is the case near the end of the cell, for particle paths affected by very large volumetric expansion rates. The particle paths crossing the lead shock immediately after the critical ignition limit were studied in detail, and the evolution of the species mass fraction confirmed no that ignition occurred along these particle paths. Despite these numerical artefacts, the time elapsed until reaching the peak thermicity remains a good measure of the ignition delay for particle paths prior to the quenching of post-shock reactions.

5.1.2 Critical Ignition with Simplified Models

Critical ignition can also be studied using simplified chemistry models to reduce the need for full chemistry calculations. To apply these models as presented in sections 2.2.2 and 2.2.3, it is necessary to calculate how the inverse activation energy ϵ and the controlling parameter ζ vary for different particles in cell cycle. From the performed simulations, one can calculate

$$\epsilon = \frac{RT_s}{E_a}, \tag{5.2}$$

with R the gas constant of the quiescent detonable mixture and T_s the post-shock temperature. The activation energy is calculated as the slope of an Arrhenius plot of the ignition delay against the inverse of the temperature, while keeping density constant,

$$Ea = \frac{\log t_{ig}^{+} - \log t_{ig}^{-}}{\log T_s^{+} - \log T_s^{-}}, \tag{5.3}$$

with $T_s^{\pm}$ a perturbation of the post-shock temperature at constant density, and $t_{ig}^{\pm}$ the ignition delay associated with its respective temperature perturbation. The controlling parameter is calculated as

$$\zeta = \left(\frac{E_a}{RT_s}\right)(\gamma - 1)\alpha t_{is}, \tag{5.4}$$

with γ the ratio of specific heats in the post-shock state, α the expansion calculated using the shock change equation, and t_{is} is the induction time without any expansion.

The model parameters are plotted in Figure 5.7 throughout the cell cycle. One can expect the ignition of a Lagrangian particle which crosses the lead shock at locations whose corresponding value of ζ satisfies the ignition criterion developed in section 2.2.6, notably that $\zeta < 1$. The intercept for the critical ignition asymptote, located at $\zeta = 1$ is plotted shown as a dotted line intercepting the x-axis at the predicted critical path. This path is located around $x/L = 0.55$ and $x/L = 0.25$ for experiments 13_H2 and 0_CH4, respectively. One immediately notices the excellent agreement between this prediction and the

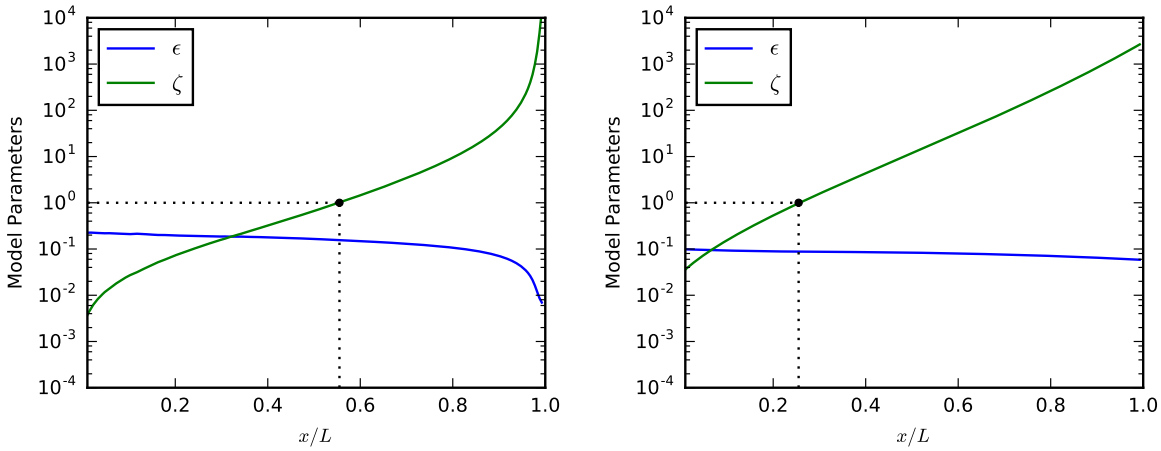

Figure 5.7: Evolution of the modelling parameters ϵ and ζ used in simplified combustion models plotted over a detonation cell. For experiments a) 13_H2 and b) 0_CH4. The dotted lines show the critical ignition asymptote predicted by the ignition criterion $\zeta < 1$.

critical ignition limit shown in Figure 5.6, calculated using a detailed chemical kinetics description of the post-shock reactions. As the modelling parameter monotonically increases throughout the cell, this criterion also models the quenching of post-shock reactions past the critical ignition limit, while allowing Lagrangian particles crossing the lead shock at distances prior to the critical ignition limit to ignite in finite time. For the majority of the cell cycle, representing a region of $0.2 < x/L < 0.8$, the controlling parameter and inverse activation energy can accurately be described by an exponential curve in space.

Using these calculated model parameters, one can meaningfully compare the ignition delay predicted by simplified chemical models and that calculated using a detailed chemistry model. Figure 5.8 shows the evolution of the non-dimensionalized ignition delay over a detonation cell, with the full set of figures included in Figure B.8. One immediately notices that the implicit solution to the two-step model given by (2.45) best captures the ignition delay across both mixtures. This was also concluded in section 2.2.5 when comparing the ignition delay predicted by simplified models with that calculated using detailed chemistry in the context of ignition behind a shock propagating at its CJ velocity. The approximate 2-step model obtained by linearizing the implicit 2-step model in the limit

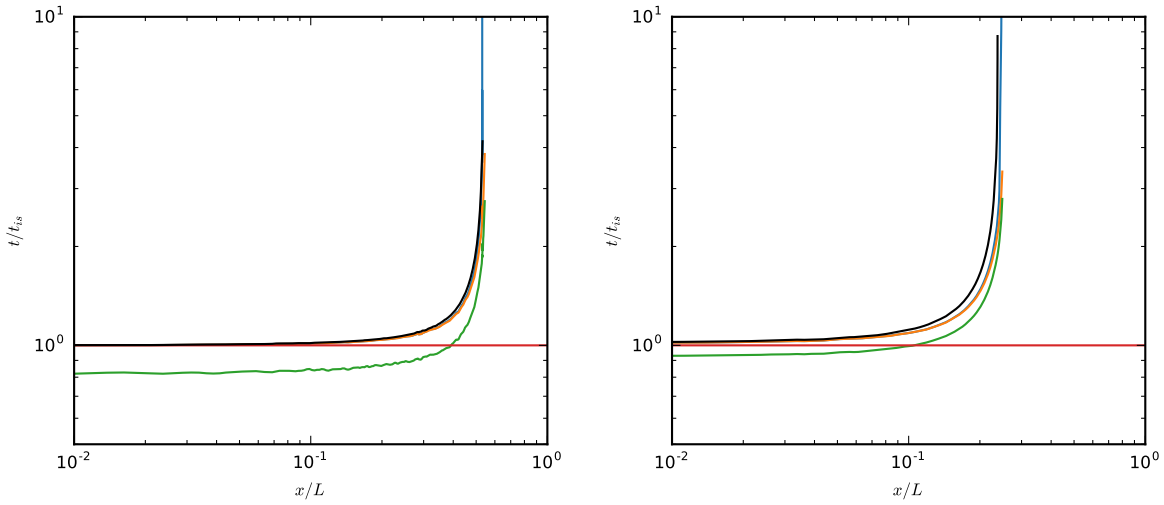

(a) (b)

Figure 5.8: Comparison of the ignition delay evolution over a detonation cell calculated using a detailed chemistry model with those predicted by simplified models derived from 1-step and 2-step chemistry. For experiments a) 13_H2 and b) 0_CH4. Blue : Implicit 2-step solution given in (2.45) for $n_i = \mathcal{O}(1)$. Green : Approximate solution for 2-step chemistry obtained by linearizing the implicit solution in ϵ, given in (2.48). Orange : 1-step and 2-step solutions in the limit of $\zeta = \mathcal{O}(1)$ given in (2.30) and (2.54). Black : solution obtained by integrating the post-shock state using a detailed chemical model. Red : ignition delay without expansion t_{is}.

of small ϵ captures the ignition delay the least well of any model, however the critical ignition asymptote is recovered within 3% of that obtained using detailed chemistry. The final model obtained in the limit of $\zeta = \mathcal{O}(1)$ accurately predicts the ignition delay in the beginning of the cell, and recovers the critical ignition asymptote within the same 3% as the approximate model. This not only supports the use of the critical ignition criterion developed in section 2.2.6 in the context of detonations, but also supports using simplified chemical models in the context of cellular detonations as an alternative to integrating a detailed chemical kinetics model.

Chapter 6

Conclusion: Contributions to the State of the Art

6.1 Summary

The present part of this thesis provided two main contributions: the development of a solution methodology to predict the ignition delay behind decaying shock waves, and the application of this theoretical treatment to assess the ignition mechanism in detonation cells.

The ignition behind decaying shock waves was modelled in two parts. The volume expansion rate along a particle path behind the shock was expressed in terms of the shock dynamic parameters (speed, acceleration and curvature) using the shock change equations. This permitted to formulate 0D ignition problems along particle paths using realistic chemistry and simplified models using one or two steps. The latter permitted to solve the problem in closed form and obtain the dependence of ignition delay on the shock dynamics and formulate an auto-ignition limit associated with a critical expansion rate.

The results of the chemical modelling were then applied to gaseous detonations. Shock

tube experiments were performed with Schlieren visualization of low-pressure detonations propagating in the stable mixture of argon-diluted hydrogen-oxygen and the highly unstable mixture of methane oxygen. The extreme differences in stability were chosen such as to span the entire range of known detonation stability in practice. From the photographs taken, the shock dynamics were determined as a function of the speed and curvature of the lead shock along the top wall, centreline, and bottom wall of the shock tube. These measurements allowed the reconstruction of an entire detonation cell. From the shock dynamics, the post-shock state was integrated using a detailed chemical kinetics model and the simple models developed in order to study the post-shock combustion and the quenching thereof inside the detonation cell.

For both mixtures studied, ignition quenching was observed within the first half of the detonation cell. Arguably, this suggests that all detonations in practice are characterized by this universal feature. The experiments showed however that the remainder of the gas crossing the lead shock after the critical ignition limit reacts from secondary initiation mechanisms such as turbulent mixing of unburnt pockets and combustion behind transverse shocks. The gas reacting due to secondary mechanisms comprises at least half the Lagrangian particles which cross the lead shock. This finding suggests that global gasdynamic models relying on lead shock auto-ignition alone are inadequate and further modelling of transverse shock compression and turbulent combustion is required. Future work should extend this model to incorporate the compression of transverse shocks for modelling auto-ignition and turbulent burning of the remaining pockets of gas.

Future work should also provide further validation of the proposed model for calculating the evolution of the ignition delay throughout a detonation cell, particularly the assumption of the constant characteristic volumetric expansion rate $(-D(\ln \rho)/Dt)$ along a particle path. This validation is a challenging task in experiments. Although the experiments provide the instantaneous reacting fields, ignition is a convected phenomenon along particle paths, and the trajectory of particle paths is required in order to determine the time at

which the particles crossed the shock. This requires the detailed velocity field and its time evolution or models.

6.2 Novel Contributions to the State of the Art

The current thesis has made the following novel contributions to the state of the art :

- This is the first treatment of ignition behind a decaying shock which links the information taken from the dynamics of the lead shock to the post-shock ignition dynamics. This was done by performing a local analysis at the lead shock which considered both the shock curvature and lead shock decay at the moment of crossing of a Lagrangian particle. This analysis gives the characteristic rate of expansion of that particle throughout the post-shock state, allowing for the integration of the conservation equations using this volumetric change in time as a forcing function. This function is the link between the ignition dynamics and the dynamics of the lead shock.

- The derivation of a simplified model using a 2-step chemical kinetics description of the post-shock state offered a novel treatment of critical ignition behind a decaying shock wave. The ignition delay is defined implicitly from this derivation for a reaction order $n_i = 1$. This model was then studied in the limit of $\zeta = \mathcal{O}(1)$ and $\gamma - 1 = \mathcal{O}(1)$ and an explicit definition of the ignition delay was obtained. The resulting equation was found identical to that obtained by deriving the ignition delay from 1-step chemistry. This equality reconciles the observations of the ignition delay behind a decaying shock made by Lundstrom & Oppenheim with those made by Eckett and co-workers and by Radulescu & Maxwell.

- The predictions obtained for the simplified models were validated against real gas calculations; very good agreement was found suggesting that both 1 step and 2 step

models can be reliably used in reactive gasdynamics models characterized by large deformations possibly leading to ignition quenching.

- A unique criterion describing the occurrence or quenching of ignition behind the lead shock is presented, notably

$$\zeta = \frac{E_a}{RT_s}\left(\gamma - 1\right) t_{is}(T_s) \left(\frac{-6}{\gamma + 1}\frac{\dot{D}}{D} - 2D\kappa\frac{\gamma - 1}{\left(\gamma + 1\right)^2} \right) < 1.$$

  This criterion generalizes the result of Eckett et al. and Radulescu & Maxwell by accounting for the shock curvature.

- The experiments performed in a weakly unstable mixture of argon-diluted hydrogen-oxygen combined with the aforementioned analysis showed that there is decoupling of the lead shock with the post-shock reaction within the first half of the cell cycle. This is a novel finding for weakly unstable mixtures, as previous findings of such occurrences was limited to the highly unstable mixture of stoichiometric methane-oxygen.

Part II

Optical Fibre-based Shock Thickness Measurement

Chapter 7

Introduction

Shock waves propagate at supersonic velocities, with characteristic pressure jumps occurring over a very small spatial region with a thickness on the order of microns to tens of microns [5]. This high velocity means that the shock presents a very short residence time for measurement apparatus. In turn, the small spatial length scales require a measurement tool with both a high spatial resolution and high sampling frequency. Fibre-optic probe hydrophones can fulfil both these requirements, with a measurement frequency in the gigahertz-range, and a spatial resolution on the order of a few microns (i.e. the diameter of the optical fibre core). Fibre optics are commonly used systems in the field of communications due to very low signal losses (typically on the order of 0.5 dB per kilometer of fibre), and high transmission speeds which typically reach 20 Gbps, or 20 GHz [26].

Measurements of shockwaves are essential for improving the understanding of blast induced neuro-trauma. The review article on this subject by Cernak and Noble [27] covers the experiments performed to study the effects of repeated exposure to weaker shocks and the effects of a single strong incident shock. In previous works consisting of experiments studying the interaction of blast waves with animals and cell cultures within shock tubes, the pressure threshold for blast-induced neuro-trauma is found to be around 100 kPa - 350 kPa [28] [29]. Radulescu notes that this pressure threshold is consistent with a shock wave

whose thickness is on the order of the characteristic cell dimension of a neuron [30], and hypothesizes that the mechanism for blast-induced neuro-trauma is linked to the shearing of neurons rather than their isotropic compression.

For such theories to be tested, a measurement technique that can accurately measure the pressure profile and thickness of shock waves is required. Fibre-optic probe hydrophones are well suited for this task, and previous works have been successful in measuring strong ultrasound waves and shock waves using such apparatus. Parsons and co-workers elaborated a cost-effective fibre-optic probe hydrophone [31]. This hydrophone incorporates a 1 W laser diode and manages to accurately reproduce pressure waves generated by an ultrasonic transducer placed near the probe. It is also shown in this study that the measurements are not sensitive to the angle formed between the fibre-optic probe and incident acoustic waves, unlike traditional pressure probes who are sensitive to the angle of incident waves. This tool is found to have a sensitivity of 0.7 mV/MPa with a 50 MHz measurement bandwidth. Lewin and co-workers have developed a similar system, improved by the addition of an avalanche photodetector [32]. This system has an increased sensitivity of 4.3 mV/MPa with a measurement bandwidth of 100 MHz, and a noise floor of 34 kPa [33]. The measure of interest when comparing measurement systems is the noise floor given in units of $\mathrm{V}/\sqrt{\mathrm{Hz}}$ or $\mathrm{Pa}/\sqrt{\mathrm{Hz}}$, however, this measure is absent in all previous studies.

Staudenraus and Eisenmenger performed a comparison of the measurements taken by traditional polyvinylidene difluoride (PVDF) needle hydrophones, membrane hydrophones, and fibre-optic hydrophones [34]. The pressure profiles obtained from shock wave measurements show that fibre optic hydrophones can measure stronger rarefactional pressures than traditional hydrophones due to a higher cavitation threshold. A good agreement is found between measurements of peak compressional pressures between measurements taken by a fibre-optic probe hydrophone and acoustically-calibrated PVDF hydrophones. The difference in measurements arises from the much higher bandwidth and smaller physical dimension of the active measurement surface, imparting a higher physical and temporal

resolution to the fibre probe hydrophone. Unlike traditional hydrophones, cavitation at the end-tip will cause a tremendous jump in reflectivity at the end-tip, which can damage the photodiode if not properly protected, and cause erroneous pressure measurements due to different material refractive indices occurring in the vapor bubbles.

The sensitivity of this measurement technique in air is much higher than that in water, due to the difference in piezo-optic constants and of the refractive indices of each material. Previous work has aimed at increasing the sensitivity of the fibre-optic probe hydrophone. Staudenraus and Eisenmenger have performed experiments with various fibre tip coatings, increasing the sensitivity up to 7 times using clear silicone rubber, or up to 30 times using opaque silicone coatings [34]. Coleman and co-workers studied a similar fibre-optic hydrophone, coated with a thin polymer film, generating shocks using a lithotripter [35]. An acoustic resonance is found corresponding to the thickness of the polymer film, and the addition of this film is theorized to increase the sensitivity by a factor of 1.5 compared to measurements performed using the bare fibre. Wilkens and Koch designed a fibre tip which is coated with fifteen dielectric layers, finding a theoretical sensitivity increase of a factor 300 compared to an uncoated fibre [36]. It is noted that important manufacturing challenges arise due to the uncertainty associated with the thicknesses of the fifteen coating layers, changing the sensitivity and the optimal wavelength for the system. Interestingly, depending on which layer has a change in thickness, the sensitivity can be increased due to manufacturing tolerances.

Here we document the assembly of a fibre-optic probe hydrophone tailored for the measurements of shock waves propagating through water. Water is chosen as the fluid of interest because its viscosity is close to that of cytoplasm [37], and the fitting parameters used in the stiffened gas equation to describe water are also close to those used for biomaterials [38]. We show that the spatial and time resolution of such a system is well-suited for the measurement of shock waves. Finally, a detailed analysis of the system noise is performed to study the resolution of the system in terms of the minimum detectable

pressure, which is found to be too high to resolve the post-shock pressures of shock waves associated with blast-induced neuro-trauma.

Chapter 8

Methodology

The experimental setup studied in this work, shown in Figure 8.1, consists of a Thorlabs 2x2 fibre optic coupler with a 50:50 split (model TN785R5F2). Attached to the four ends of this coupler is a Thorlabs compact laser diode and temperature controller (model CLD1015) mounting a Thorlabs 785nm-wavelength Fabry-Perot laser diode (model FPL785-250) and a photodetector. Two different photodetectors are studied here, a Thorlabs Si-amplified fixed-gain photodetector (model PDA10A2) and a Hamamatsu Avalanche Photodetector (model C5658). Both the laser diode and the photodetector are mounted on the same side of the 2x2 fiber coupler, whereas the pressure vessel measurement tip and a laser dump (model FTAPC1) are placed on the other side of the coupler. The setup is inspired by the setup elaborated by Parsons and co-workers [31]. Presently there is no isolator present in the system, although this can be added between the coupler and the laser diode to reduce laser noise. A monitoring photodetector can be added instead of the laser dump at the fourth end-tip, allowing for the measurement (and subsequent subtraction from signal) of laser fluctuations. The oscilloscope connected to the photodetector used are either a Digilent Analog Discovery 2 or a Lecroy 24XS-A, and can both be operated in either AC-coupled or DC-coupled modes. The specification sheets for the equipment used can be found in Appendix E.

Referring to Figure 8.1, one sees the optical path taken by the light from the laser to the photodetector. The light first leaves the laser with a given optical power, P_{laser}, until reaching the 2x2 coupler. The optical power is then split when passing through the optical fibre coupler depending on the coupling ratio, $P_{3,I}$ is the optical power incident to the fibre tip, and P_4 the optical power incident to the laser dump tip. The incident light, $P_{3,I}$, reflects at the end tip according to Fresnel's Law, depending on the refractive indices of the material on the other side of the interface and the fibre core. The refractive index of the fluid in the pressure vessel is pressure-dependant, allowing for the measurement of pressure based on the amount of refracted light at the end-tip. Whether the photodetector or the dump is installed at the end of the fibre, the amount of light reflected by the dump, $P_{4,R}$, is negligible. In the former case, light will pass through an attenuator of 36 dB, in addition to a very high return loss at the photodetector itself. In the latter case, Thorlabs fibre optic light traps improve the return loss to better than 50 dB. The reflected light, $P_{3,R}$ returns to the coupler, and is split again into two equal components following the previous 50:50 ratio, with equal parts of the reflected light directed to the laser diode and the photodetector. Finally, the light impinges the photodetector with optical power P_2. This detector converts the optical power to a voltage recorded by the oscilloscope. The components used for the setup are summarized in Table 8.1. The physical setup of the measurement system is shown in figure 8.2. A Fabry-Perot type laser diode is used in this setup due to its high power output. The high power output is required for the current setup due to the small amount of light reflected at the measurement tip, despite the higher noise of Fabry-Perot lasers when compared to alternative kinds of lasers such as distributed feedback (DFB) lasers or vertical cavity surface-emitting lasers (VCSEL). These alternatives generally either have lower optical power or produce a multimode signal at higher optical powers. Both of these drawbacks make these other laser types unsuitable for the current study.

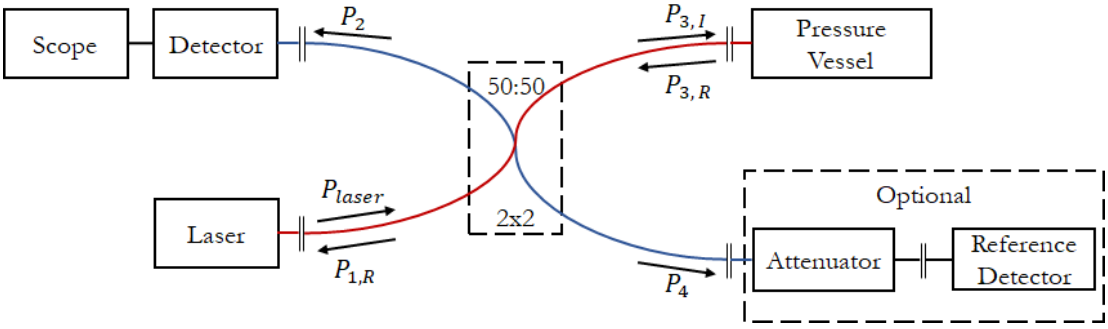

Figure 8.1: Schematic of the optical measurement system setup. PD represents the photodetector. The optional components can be replaced by a laser dump. Fibre connections are shown as two vertical bars.

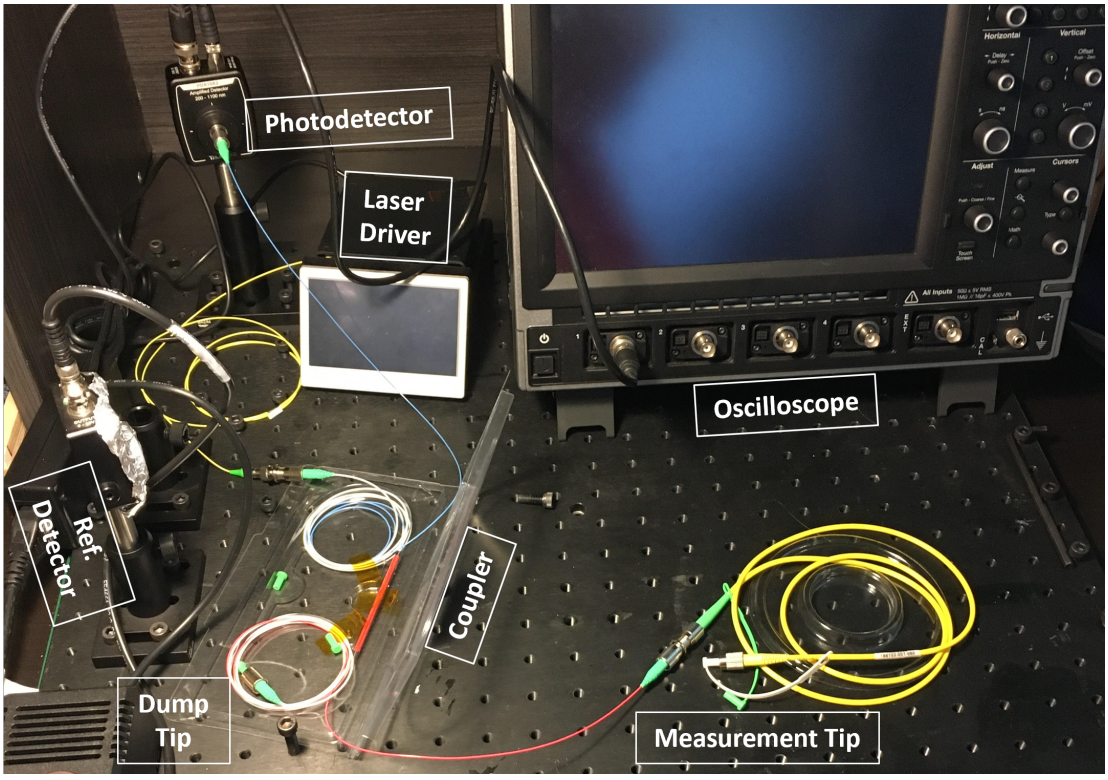

Figure 8.2: Physical setup of the assembled measurement system. The optional reference photodetector is shown on the bottom left-hand side of the image.

Table 8.1: Components used to assemble the measurement system. Components marked as *Alternatives* were not used to take measurements but were considered during the calculation of the noise floor.

Component Type	Manufacturer	Model	Notes
Oscilloscope	Lecroy	Wavesurfer 24Xs-A	
Oscilloscope	Digilent	Analog Discovery 2	Alternative
Photodetector	Thorlabs	PDA10A2	
Photodetector	Hamamatsu	C5658	Alternative
Laser Driver	Thorlabs	CLD1015	
Laser Diode	Thorlabs	FPL785S-250	
2x2 Coupler	Thorlabs	TN785R5A2	
Laser Dump	Thorlabs	FTAPC1	

8.1 Transfer Function

Given the optical setup detailed above, it's possible to elaborate a transfer function which gives the change of voltage measured by the oscilloscope as a function of the pressure at the fibre end-tip. The optical power transmitted along the same fibre in the 2x2 fiber optic coupler is reduced by a coefficient $\mathbb{C}_1$, for the light propagating from the laser diode to the measurement tip, whereas the optical power of the light propagating across fibres is reduced by a coefficient $\mathbb{C}_2$. The laser power at the fibre end-tip and the dump tip are thus

$$P_{3,I} = \mathbb{C}_1 P_{laser}, \tag{8.1}$$

$$P_4 = \mathbb{C}_2 P_{laser}, \tag{8.2}$$

with P_{laser} the optical power produced by the laser diode, $P_{3,I}$ the optical power incident to the fibre tip, and P_4 the optical power incident to the laser dump tip. As the optical power of the light transmitted through the optical coupler is conserved,

$$\mathbb{C}_1 + \mathbb{C}_2 = 1. \tag{8.3}$$

The reflected light, $P_{3,R}$, is a factor R of the incident light at the end-tip,

$$P_{3,R} = P_{3,I}R. \tag{8.4}$$

The light reflected from the fibre tip which is returned to the photodetector after another reduction in optical power of a factor $\mathbb{C}_2$ is

$$P_{1,R} = \mathbb{C}_1 P_{3,R} = \mathbb{C}_1 P_{3,I} R = \mathbb{C}_1^2 P_{laser} R. \tag{8.5}$$

$$P_2 = \mathbb{C}_2 P_{3,R} = \mathbb{C}_2 P_{3,I} R = \mathbb{C}_1 \mathbb{C}_2 P_{laser} R. \tag{8.6}$$

The contribution of the reflected light made from the tip with either the dump or the monitor detector is negligible if these are properly installed. The amount of light reflected at the end tip follows Fresnel's Law, which is dependent on the refractive indices of the fibre and the material on the other side of the interface, as per Equation 8.7, in which n_g denotes the glass' refraction index and n_m denotes the material's refraction index.

$$R = \left(\frac{n_g - n_m}{n_g + n_m} \right)^2. \tag{8.7}$$

The transfer function will allow the conversion of a change in pressure to a change in voltage, thus allowing the transformation of measurements taken into the physical pressure change measured. This ratio can be expressed by

$$\frac{\partial p}{\partial V} \left[\frac{Pa}{V} \right] = \frac{\partial p}{\partial n} \frac{\partial n}{\partial V} = \frac{\partial p}{\partial n} \left(\frac{\partial n}{\partial R} \frac{\partial R}{\partial V} \right). \tag{8.8}$$

The piezo-optic coefficient $\partial n / \partial p$ of silica is at least two orders of magnitudes smaller than that of water or air, thus one can neglect changes of the index of glass, and consider only changes of the index in the fluid under test

$$\frac{\partial p}{\partial V} \left[\frac{Pa}{V} \right] = \frac{\partial p}{\partial n_m} \frac{\partial n_m}{\partial V} = \frac{\partial p}{\partial n_m} \left(\frac{\partial n_m}{\partial R} \frac{\partial R}{\partial V} \right). \tag{8.9}$$

In the previous equation, $\frac{\partial p}{\partial n_m}$ represents the inverse of the change of refractive index with pressure, $\frac{\partial n_m}{\partial R}$ the inverse of the change of reflected light at the end-tip as a function of the refractive index, and $\frac{\partial R}{\partial V}$ the inverse of the change of voltage as a function of reflected light. Deriving Fresnel's law by the change on the material refractive index, one obtains

$$\frac{\partial R}{\partial n_m} = \frac{\partial}{\partial n_m}\left(\frac{(n_g - n_m)^2}{(n_g + n_m)^2}\right). \tag{8.10}$$

Applying the quotient rule, followed by the chain rule, and simplifying the result, one obtains

$$\boxed{\frac{\partial R}{\partial n_m} = \frac{4n_g(n_m - n_g)}{(n_g + n_m)^3}.} \tag{8.11}$$

The change of voltage with reflectance, $\frac{\partial V}{\partial R}$, can be found using the specifications of the photodetector and Equation 8.5. Expanding the terms in this equation and considering the light reflected from the dump tip is negligible, one obtains,

$$P_{det_{\text{ideal}}} = \mathbb{C}_1\mathbb{C}_2 P_{laser} R_3. \tag{8.12}$$

The amount of light at the photodetector is affected by optical losses in the system, therefore one can apply a general attenuation term $A_{loss} \approx 1$ to this equation, obtaining

$$P_{det} = \mathbb{C}_1\mathbb{C}_2 P_{laser} R_3 A_{loss}. \tag{8.13}$$

The loss term comprises all the non-negligible optical losses, notably up to 1.5 dB transmission loss [39] at each connection (shown as vertical double lines in Figure 8.1), and the 0.16 dB and 0.24 dB optical loss through the coupler, for a total loss of up to 6.4 dB. This loss is the maximum which can affect the system, therefore we consider an average loss of 3.2 dB ± 3.2 dB. Using the specification sheet values, one can convert the optical power measured to the voltage output of the photodetector. Thus, the equation for the voltage read by the photodetector, V_{det}, is

$$\begin{aligned} V_{det} &= P_{det}\mathbb{R}\mathbb{G}S_F \\ &= \mathbb{C}_1\mathbb{C}_2 P_{laser} R_3 \mathbb{R}\mathbb{G} A_{loss} S_F, \end{aligned} \tag{8.14}$$

with $\mathbb{R}$ the responsivity of the photodetector in A/W, $\mathbb{G}$ the detector gain in V/A, and S_F the scaling factor of the photodetector, given by Thorlabs as

$$S_F = \frac{Z_{\text{Load}}}{Z_{\text{Load}} + Z_S}, \tag{8.15}$$

with Z_S the 50 Ω series resistor within the photodetector, and Z_{Load} the oscilloscope load. This relationship can also be used to measure the static pressure. The change in voltage with respect to a change in reflectance is found by deriving the above equation, such that

$$\boxed{\frac{\partial V}{\partial R} = \mathbb{C}_1\mathbb{C}_2 P_{laser}\mathbb{R}\mathbb{G}A_{loss}S_F.} \tag{8.16}$$

Substituting equations (8.11) and (8.16) into equation (8.8),

$$\frac{\partial p}{\partial V} = \frac{\partial p}{\partial n}\left[\frac{(n_g + n_m)^3}{4n_m(n_g - n_m)}\right]\left[\frac{1}{\mathbb{C}_1\mathbb{C}_2 P_{laser}\mathbb{R}\mathbb{G}A_{loss}S_F}\right]. \tag{8.17}$$

From the specification sheet, one obtains $\mathbb{G} = 5$ kV/A for a 50 Ω load, or 10 kV/A for a 1 MΩ load. A high-impedance load is used in this setup. The responsivity is $\mathbb{R} = 0.421$ A/W for a wavelength of 785 nm. Additionally, the indices of refraction used are $n_g = 1.455$ for the Thorlabs fibre, and $n_m = 1.333$ for water or $n_m = 1.000$ for air. The coupler used splits the light equally such that $\mathbb{C}_1 = \mathbb{C}_2 = 0.5$. The mid-range value of $\partial n/\partial p = 1.49 \times 10^{-4}$ MPa^{-1} is used, from the extreme values of $\partial n/\partial p = 1.32 \times 10^{-4}$ MPa^{-1} and $\partial n/\partial p = 1.66 \times 10^{-4}$ MPa^{-1} used by Parsons [31] for water such that the error from this range of values is symmetrical. The value of $\partial n/\partial p = 2.637 \times 10^{-3}$ MPa^{-1} used by Xu [40] is taken for air. The simplified transfer function is thus,

$$\boxed{\left(\frac{\partial p}{\partial V}\right)_{water} = \frac{-410 \pm 240}{P_{laser}} \frac{\text{MPa}}{\text{V}},} \tag{8.18}$$

$$\boxed{\left(\frac{\partial p}{\partial V}\right)_{air} = \frac{-4.2 \pm 3.0}{P_{laser}} \frac{\text{MPa}}{\text{V}},} \tag{8.19}$$

The sensitivity of the measurement tool can also be expressed as the inverse of the transfer function above. This represents the voltage change induced by a pressure change, commonly written in units of $\frac{mv}{Pa}$. Taking the inverse of the transfer function, one obtains

$$\boxed{\left(\frac{\partial V}{\partial P}\right)_{water} = [-2.5 \pm 1.5]\, P_{laser} \frac{\text{mV}}{\text{MPa}},} \tag{8.20}$$

$$\boxed{\left(\frac{\partial V}{\partial P}\right)_{air} = [-240 \pm 170]\, P_{laser} \frac{\text{mV}}{\text{MPa}}.} \tag{8.21}$$

with P_{laser} the laser power in Watts. These transfer functions allow for the conversion of a signal measured in voltage to a pressure felt at the end-tip.

The transfer function obtained has a relatively large uncertainty associated with certain terms which are required in its derivation. Due to the very large variability in literature values for piezo-optic coefficient, $\partial n/\partial p$, one can expect an inherent error of ±9% associated to this parameter for water, and ±20% in air [41]. Additionally, neglecting the change of the

fibre refractive index n_g with pressure adds an additional source of error of around $\pm 3.6\%$ [33, 34]. Finally, one can expect a source of error due to the small amount of optical reflection which occurs at each connection in the system, notably at the photodetector's and the laser diode's connection to the coupler. These effects are neglected due to the small percentage of optical power being reflected, this being further decreased by the use of angled polished connectors (APC), which have a typical reflection of 60 dB (0.1%). These internal reflections will add stray light to the system, which can interfere with laser operation, especially considering the lack of an optical isolator between the coupler and the laser diode due to cost constraints. For single-mode lasers with far-field reflections, it has been found that the laser output power varies with stray light amplitude. Additionally, a single mode laser will oscillate in multimode with increasing stray light [42]. In this case, resonant peaks would appear in the frequency response at frequencies related to the round-trip time of the reflected light.

Most importantly, one must consider the contribution of the potential 6.4 dB loss from the fibre connections. Of this value, 3.2 dB is included in the transfer factor shown in (8.17), whereas the other 3.2 dB is included as a symmetric error of $\pm 48\%$. The connection error changes whenever a connection is replaced, though the exact contribution of this source of uncertainty can be determined through a static pressure measurement. If one neglects the uncertainty from this error, the transfer factor and sensitivity of the system using water as the measurement fluid becomes

$$\left(\frac{\partial p}{\partial V}\right)_{water} = \frac{-410 \pm 51}{P_{laser}} \frac{\text{MPa}}{\text{V}}, \tag{8.22}$$

$$\left(\frac{\partial V}{\partial P}\right)_{water} = [-2.5 \pm 0.3]\, P_{laser} \frac{\text{mV}}{\text{MPa}}, \tag{8.23}$$

whose uncertainty is representative of the system once connector losses are measured.

The measurement bandwidth is currently limited to 150 MHz by the Thorlabs photodetector, whereby the Lecroy oscilloscope is capable of measurements up to a frequency of

200 MHz. An avalanche photodetector manufactured by Hamamatsu with a measurement bandwidth of 1 GHz and a Lecroy WaveSurfer 4000HD 1 GHz oscilloscope can be installed to increase the bandwidth of the overall system to 1 GHz.

The current measurement tip, consisting of an optical fibre held in place within a pressure vessel by a fibre chuck, is susceptible to damage caused by the passing of strong shock waves and cavitation. To detect damage, one can take measurements of the static pressure between experiments, as fibre damage will significantly change the amount of light reflected at the measurement tip [34]. Upon identification of fibre damage, re-cleaving the fibre-tip offers a cost-effective way of replacing damaged segments of optical fibre, with the long-term stability of the system ensured through the use of precision cleaving apparatus.

8.1.1 Reference Photodetector

The coupler's fourth end-tip, which is shown in Figure 8.1 as an optional dump tip which absorbs the incident light, but allows for the addition of a reference photodetector to the system. This photodetector can either be a differential input photodetector linked to the second end-tip to provide a reference of the power output of the laser diode, or can be another single-ended photodetector. The addition of this photodetector is important for monitoring the laser instabilities, caused notably by the lack of an isolator protecting the laser diode from stray light. In the latter case of two single-ended photodetectors, two oscilloscope channels are needed and elimination of laser instabilities (i.e. mode hopping) is done in post-processing. When using a monitor detector installed on right side of the coupler shown in Figure 8.1, an attenuator is required to prevent the damage to the photodiode from the strong incident light and exceeding the photodetector's saturation limit. This attenuation is calculated as

$$A = 20 \log_{10} \frac{P_{2,A}}{P_{2,i}}, \tag{8.24}$$

in which $P_{2,A}$ is the optical power including the attenuator, and $P_{2,i}$ is the incident power at the photodetector without the attenuator as seen in Figure 8.1. Considering that the maximum output voltage of the detector is 5 V at a 50 Ω load, then

$$V_{2,i} = P_{det} \mathbb{R} \mathbb{G} S_F, \tag{8.25}$$

with

$$P_{det} = \mathbb{C}_2 P_{laser}, \tag{8.26}$$

The maximum optical power at the photodetector at its saturation limit is thus

$$P_{det} = \frac{5V}{0.421 \cdot 5000} = 2.375 \text{ mW}. \tag{8.27}$$

Considering a maximum laser power of 300 mW, one can calculate the required attenuation. As a portion of the laser power is lost through the coupler before reaching the photodetector, the optical power at the photodetector is

$$P_{2,i} = \mathbb{C}_2 P_{laser}. \tag{8.28}$$

Recalling (8.24), the optical attenuation required ahead of the photodetector is thus

$$A = 20 \log_{10} \frac{2.375 \text{ mW}}{150 \text{ mW}} = -38 \text{ dB}. \tag{8.29}$$

Chapter 9

Performance Limit Analysis

Before performing experiments, it is necessary to determine the limits of the experimental setup in terms of the noise floor, bandwidth, and spatial resolution. When measuring shock waves, the minimum detectable pressure represents the smallest change in fluid pressure which can be measured and distinguished from the noise produced by the measurement system. Additionally, the minimum detectable power is independent of the conversion factors introduced by physical equipment such as the gain and the responsivity, allowing for meaningful comparisons between measurement systems. In this analysis, the spatial and temporal resolution of the measurement tool system will be calculated and compared with the time and length scales associated with shock waves. Following this scale study, the noise floor of the system will be analysed on a component by component basis and compared to the experimentally measured system noise. Finally, the sources of noise will be compared to identify the limiting noise source and study the capability of the system to measure shock waves.

9.1 Resolution Study

Consider a pressure wave with a finite thickness Δ, as shown in Figure 9.1, propagating at an arbitrary speed D. A measurement probe with a small active diameter, δ, is placed ahead of the traveling wave such that at $t = t_0$ the leading edge of the wave is in contact with the probe's active surface. The shock speed D and thickness Δ of the pressure wave both are a function of its strength, or Mach Number M_s, which is defined as

$$D = M_s c_0, \tag{9.1}$$

with c_0 the sound speed in the material. The probe fibre tip has two possible orientations to perform measurements of the shock wave, whether it be normal to the incident wave such as in Figure 9.1 a), or parallel to the incident wave such as in Figure 9.1 b). This chapter studies the spatial and temporal limitations of the pressure waves which can be measured by such a probe.

Firstly, one can study the residence time $t_{residence}$ of this wave such that an estimate of the number of points within the wave can be made given a certain measurement bandwidth. The residence time of the wave is related to the shock thickness and speed as

$$t_{residence} = \frac{\Delta}{D}. \tag{9.2}$$

The temporal resolution of the measurement device is given as a function of the measurement bandwidth BW, also known as the sampling rate,

$$t_{resolution} = \frac{1}{\mathrm{BW}}. \tag{9.3}$$

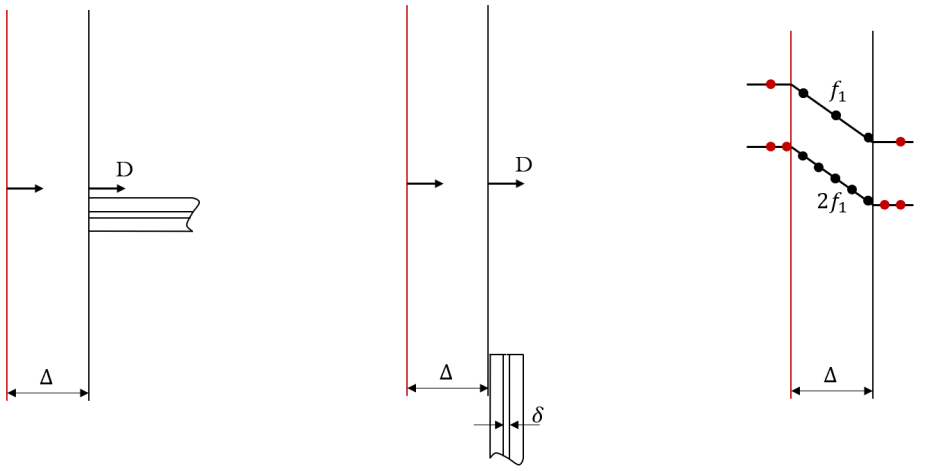

(a) (b) (c)

Figure 9.1: Schematic of a shock wave propagating in a material, with the measurement probe oriented a) Normal to the wave incidence and b) parallel to the wave incidence. c) Schematic plotting measurement points equidistant in time, with black points within the wave thickness and red points outside the wave thickness. All waves are propagate from left to right.

This resolution time is the amount of time between two measurements. The number of measurement points expected within a wave's thickness is thus

$$\boxed{n_{points} = \frac{t_{residence}}{t_{resolution}} = \frac{\Delta \mathrm{BW}}{D}.} \tag{9.4}$$

Equation 9.4 is an important metric. If one seeks to characterize a certain shock of strength M_s, this gives the shock thickness Δ and shock speed D. These two properties can then be used to calculate the required bandwidth to obtain a spatial resolution of n_{points}. For example, to measure a typical shockwave with an overpressure of 400 kPa, with an accuracy of 5 points, one would need a bandwidth of 435 MHz, which decreases to 261 MHz if the spatial resolution is decreased to 3 points.

The temporal resolution is obviously linked to the measurement system bandwidth, but also to the wave thickness (Δ) and speed (D). These two wave parameters are governed by the Mach number, M_s. Thompson [5] includes a derivation of a relationship between the shockwave thickness, material properties, and wave strength, which is valid for weak shocks,

$$\Delta \approx \frac{8}{3}\frac{\mu}{\rho c}\left(\sqrt{\frac{1}{2\gamma}\frac{p_2+p_\infty}{p_1+p_\infty}(\gamma+1)+(\gamma-1)}-1\right)^{-1}, \tag{9.5}$$

in which p_1 and p_2 are the pre- and post-shock pressures, p_∞ is the stiffening pressure, γ is an empirically determined material constant, μ, ρ, and c are the material's viscosity, density, and sound speed. One can find a Rankine-Hugoniot equation for the shock strength as a function of pressure which follows the Stiffened Gas equation, written for the Mach number:

$$M_s = \sqrt{\frac{\left(\frac{p_2+p_\infty}{p_1+p_\infty}\right)(\gamma+1)+(\gamma-1)}{2\gamma}}. \tag{9.6}$$

The approximation for the shock thickness can be re-written to bring the Mach number into evidence, such that

$$\Delta \approx \frac{8}{3}\frac{\mu}{\rho c}\frac{1}{M_s-1}. \tag{9.7}$$

Considering these two parameters, the temporal resolution could approximated as

$$n_{points} \approx \frac{8\mu \mathrm{BW}}{3\rho c_0^2 M_s(M_s-1)}. \tag{9.8}$$

The stiffened gas parameters for water are given by Nakahara and co-workers as $\gamma = 7$ and $p_\infty = 296$ MPa [38]. The viscosity of water is taken as $\mu = 0.0028$ Pa·s, and the density as $\rho = 1000$ kg/m^3.

A limitation on the measurement tool's spatial resolution appears when considering the orientation of the probe (see Figure 9.1). In the first orientation when the fibre is placed normal to the incident shock as in Figure 9.1 a), there is no physical limitation on the shock thickness that can be measured. On the other hand, when the measurement fibre is placed parallel to the incident shock as in Figure 9.1 b), the wave thickness Δ should be larger than the active diameter of the fibre, δ. This restriction is placed to minimize spatial averaging, which becomes important when a thin shock-wave propagates parallel to the end-tip. According to Parsons' study [31], the orientation of the fibre-optic probe relative to the direction of shock propagation does not noticeably affect the measurements of acoustic waves. Due to the wave thinning as a function of pressure, one can infer that as the thickness of the wave becomes comparable to the diameter of the fibre, spatial averaging effects become considerable, and the orientation of the measurement tip will become important. Orienting the probe at an angle between the two extremes shown in Figure 9.1 will impart a limitation similar to that suffered by the parallel orientation with the limiting active diameter depending on the angle between the wave propagation and the fibre tip.

The temporal and spatial resolution limitations are summarized in Figure 9.2. An approximation of the wave thickness and residence time obtained from (9.5) and (9.8) are plotted against the post-shock pressure. Three pressures of interest are outlined on this graph. The first, at around 330 kPa, is associated with a residence time allowing for 3 points to be measured within the wave thickness, considering a measurement bandwidth of 200 MHz. In other words, with a measurement bandwidth of 200 MHz, it is possible to measure at least 3 points within a shock wave if the post-shock pressure is 330 kPa or lower. Conversely, at around 1250 kPa, the limit of a 1 GHz measurement system is reached, for the same 3-points criterion. Finally, the blue line plotted around 950 kPa outlines to the spatial resolution criterion illustrated in Figure 9.1 b), where the ratio of wave thickness to active diameter ($\delta = 5$ μm) reaches unity. For measurements of stronger waves, the effect

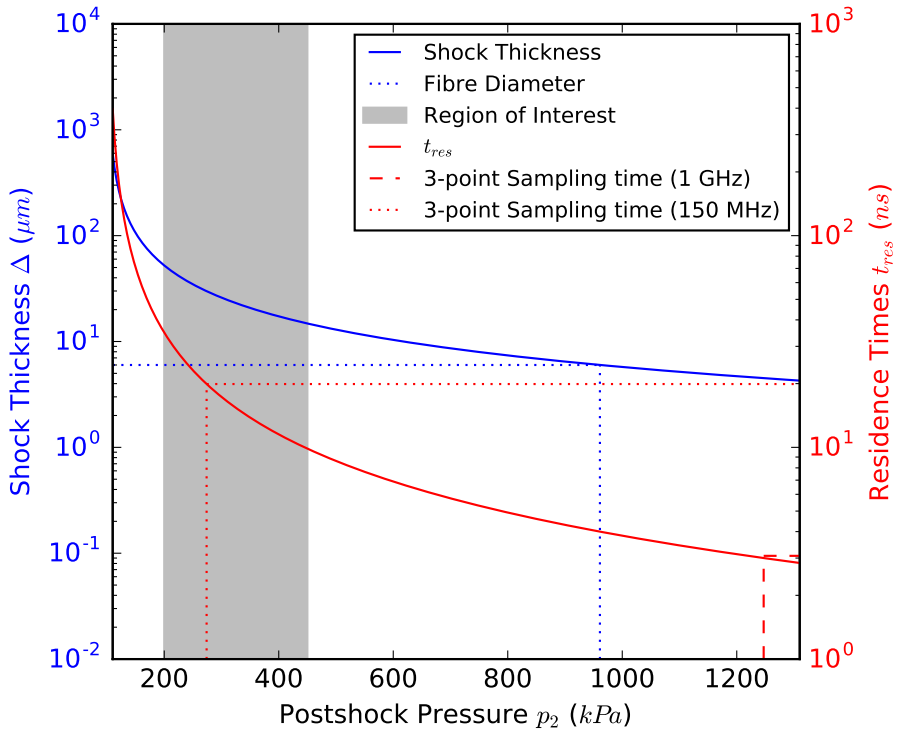

Figure 9.2: Estimated shock wave thickness and residence time for a shock propagating through water as a function of the post-shock pressure, with the limitations of the system identified as dotted and dashed lines. The region of interest for blast-induced neuro-trauma is shaded in grey.

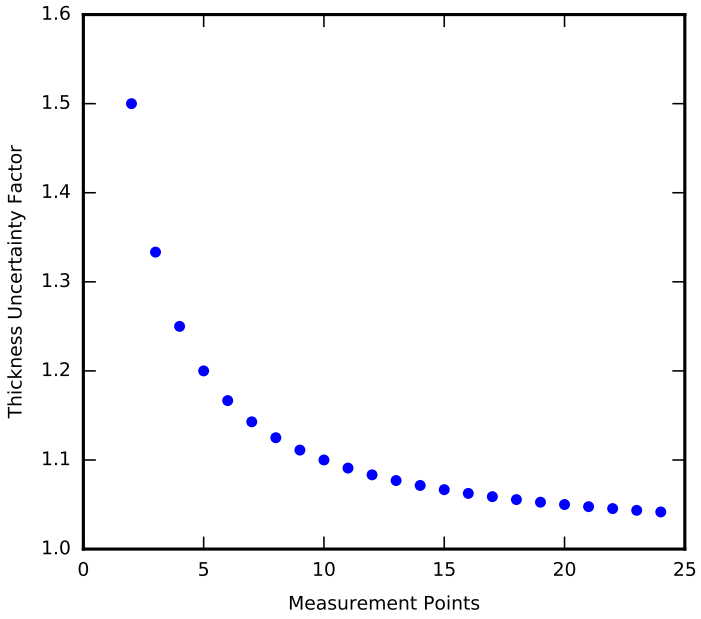

Figure 9.3: Estimated shock wave thickness uncertainty plotted as a function of the number of points which are used to measure the wave thickness.

of probe orientation relative to the shock propagation becomes significant.

Previous studies of neuro-trauma stemming from blast waves consider 100 kPa - 300 kPa as the range of interest, making this tool ideal for such studies as multiple points can be placed within the thickness of the wave at lower pressures. Increasing the number of points placed within the wave decreases the uncertainty on the wave thickness measurement. The "true" thickness of the wave is always thicker than the measured value with a thickness uncertainty associated to one measurement point. Thus, the wave thickness will always be within a factor of two from the measured value, provided at least two points are used to capture the wave. This factor quickly decreases with additional points, reaching a factor of 1.2 with 5 points placed within the wave, shown in Figure 9.3. Adding an additional 5 points only decreases the uncertainty to a factor of 1.1, and any additional points past this will see a slowly decreasing uncertainty. For the remainder of this study, 3 points will be considered as sufficient to accurately capture the wave thickness, for a thickness uncertainty factor of 1.3.

The effect of the measurement bandwidth on the number of points placed within the wave thickness is clearly shown in Figure 9.4. The first curve of 100 MHz have a good resolution for weaker waves, making this frequency ideal for the measurement of acoustic wave, however the frequency is insufficient to resolve waves associated with blast-induced neuro-trauma. A bandwidth of 200 MHz is the minimum required for this study to properly resolve the wave with at least 3 points until post-shock pressures of 330 kPa, representing the weaker half of the shock waves of interest. To properly resolve the entire region, one would require a bandwidth of at least 300 MHz to measure three points. Finally, increasing the bandwidth to 1 GHz yields a measurement of at least 9 points throughout the region of interest, with over 25 points measured for the weaker waves associated with blast-induced neuro-trauma. This would be the ideal measurement bandwidth of those considered, however the noise associated with measurements taken at high frequency will be higher than those at lower frequencies.

9.2 Theoretical System Noise Calculations

Having enough points within the shock wave does not necessarily mean that this system can resolve the pressure variations associated to the shock wave. Pressure resolution is given by the system noise floor, which is equally important, if not more, than the spatial and temporal resolutions discussed in section 9.1. The theoretical noise floor of the system represents the minimum measurable pressure, or voltage, that can be measured and distinguished from the background system noise. An analysis of the noise figure of each system component is required to find the current system limiting noise source, as well as the fundamental possible resolution if all system components are fully optimized. The component noise is studied in detail in sections 9.2.1 - 9.3, and subsequently summarized and compared in section 9.4.

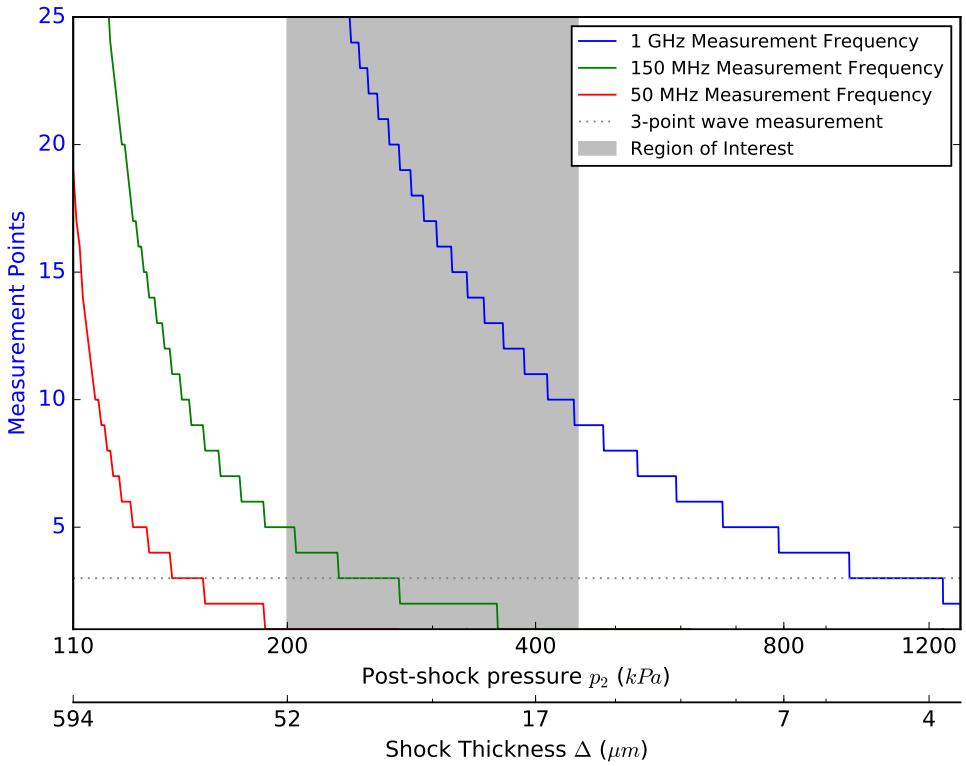

Figure 9.4: The number of measurement points which can be used to measure the thickness of a shock wave as a function of the shock thickness and post-shock pressure, plotted for 50 MHz, 150 MHz, and 1 GHz measurement bandwidths. The region of interest for blast-induced neuro-trauma is shaded in grey. A bandwidth of 150 MHz is sufficient to resolve the weaker half of the region of interest. A bandwidth of 305 MHz is required to measure all shock waves in the region of interest with at least 3 points.

9.2.1 Digitization Limit

The digitization limit is introduced by the conversion of the photodetector analog signal into a digital signal by the oscilloscope. The analog-to-digital converter (ADC) within the oscilloscope performs this conversion with a finite number of bits. A rounding error is introduced, and part of the analog signal is lost. The digitization limit is highly dependent on whether the oscilloscope has tunable input gain, which allows for the amplification of the signal before digitization, and on the bit resolution of the ADC.

From its specification sheet, the Analog Discovery 2 has a 14-bit resolution at its smallest range of -2.7 V to +2.6 V, for a total peak-to-peak voltage of 5.3 V. The other oscilloscope considered, a LeCroy WaveSurfer24Xs-A, has an 8-bit resolution. This resolution determines the bits used in a binary number representation, where each bit takes the value of 0 or 1. As such, 14-bit resolution can represent 2^{14} different numbers whereas 8-bit resolution can represent 2^8 numbers. One can find the voltage corresponding to a single bit as

$$V_{bit} = \frac{V_{pk-pk}}{N_{bits}} \tag{9.9}$$

in which V_{pk-pk} represents the peak-to-peak voltage, and N_{bits} the resolution of the oscilloscope. Applying this equation to the above-mentioned oscilloscopes, one finds the bit noise in voltage

$$V_{bit_{AD2}} = \frac{5.3V}{2^{14}} = \frac{5.3 \text{ V}}{16384} \tag{9.10}$$

$$V_{floor_{AD2}} = 0.00032 \text{ V} \tag{9.11}$$

Using the transfer function previously elaborated in (8.18), one finds a noise floor in pressure units as being

$$p_{\text{bit floor}_{AD2}} = \frac{130}{P_{laser}} \text{ kPa} \tag{9.12}$$

Considering a laser power of 270 mW, the rounding error is thus

$$p_{\text{bit floor}_{AD2}} = 480 \text{ kPa} \tag{9.13}$$

The Lecroy 24Xs-A offers the possibility of amplifying the analog signal before any digital conversion occurs. One can calculate the bit noise of this oscilloscope at its 8-bit resolution and maximum 2mV/div sensitivity as

$$V_{floor_{24Xs}} = \frac{2 \text{ mV/div } 4 \text{ divs}}{2^8} = \frac{8mV}{256} = 31 \ \mu\text{V} \tag{9.14}$$

$$V_{floor_{24Xs}} = \frac{13}{P_{laser}} \text{ kPa} \tag{9.15}$$

Considering a laser power of 270mW, the rounding error is as low as

$$p_{\text{bit floor}_{24Xs}} = 47 \text{ kPa}. \tag{9.16}$$

9.2.2 Detector Noise Equivalent Power

The Noise Equivalent Power (NEP) is a measure of the sensitivity of the photodetector, a function of the minimum detectable power, defined as the power required for the signal-to-noise ratio to be equal to one. From the specifications given by Thorlabs for the photodetector[43], one can calculate the noise this introduces to the system. The NEP can be calculated from the maximum responsivity $\mathbb{R}_{max}$ and the wavelength-specific responsivity $\mathbb{R}(\lambda)$ found in the specification sheet,

$$\mathrm{NEP}(\lambda) = \mathrm{NEP}_{min}\frac{\mathbb{R}_{max}}{\mathbb{R}(\lambda)}, \tag{9.17}$$

$$\mathrm{NEP}(785\mathrm{nm}) = 3.4 \times 10^{-11}\frac{W}{\sqrt{Hz}}. \tag{9.18}$$

Applying the photodetector's gain and responsivity, the voltage equivalent to the NEP is

$$V_{\text{NEP floor}_{\text{PDA10A2}}} = \mathrm{NEP}(785\mathrm{nm})\mathbb{R}\mathbb{G}\left[\frac{W}{\sqrt{Hz}}\right]\left[\frac{A}{W}\right]\left[\frac{V}{A}\right] \tag{9.19}$$

$$V_{\text{NEP floor}_{\text{PDA10A2}}} = 1.4 \times 10^{-7}\frac{\mathrm{V}}{\sqrt{Hz}} \tag{9.20}$$

finally, applying the transfer factor to this voltage, one finds the NEP in units of pressure

$$p_{\text{NEP floor}_{\text{PDA10A2}_w}} = \frac{58}{P_{laser}}\frac{\mathrm{Pa}}{\sqrt{Hz}}, \tag{9.21}$$

$$p_{\text{NEP floor}_{\text{PDA10A2}_a}} = \frac{0.59}{P_{laser}}\frac{\mathrm{Pa}}{\sqrt{Hz}}. \tag{9.22}$$

Considering a laser power of 270 mW and water as the fluid, the noise floor is

$$p_{\text{NEP floor}_{\text{PDA10A2}_w}} = 215\frac{\mathrm{Pa}}{\sqrt{Hz}} \tag{9.23}$$

For example, if the measurement bandwidth is 1 MHz, the integrated noise floor would be

$$p_{NEPfloor_{1MHz}} = 215\frac{\mathrm{Pa}}{\sqrt{Hz}}\sqrt{1000000Hz} = 215kPa. \tag{9.24}$$

If this measurement bandwidth increases to 1 GHz, the integrated noise floor would increase to

$$p_{NEPfloor_{1GHz}} = 215\frac{\mathrm{Pa}}{\sqrt{Hz}}\sqrt{1000000000Hz} = 6.8MPa. \tag{9.25}$$

A similar analysis can be performed for the Hamamatsu C5658 APD Photodetector, which has a higher measurement bandwidth of 1 GHz. From its specification document, this photodetector has a noise level of -48dBm. This gives a noise power relative to 1mw of

$$\text{NEP}_{\text{C5658}} = 1.6 \times 10^{-8}\text{W}. \tag{9.26}$$

As this noise power is integrated across the 1 GHz measurement bandwidth, one obtains a NEP of

$$\text{NEP}_{\text{C5658}} = 5.0 \times 10^{-13}\frac{W}{\sqrt{Hz}}. \tag{9.27}$$

This can be multiplied by the detection sensitivity of $2.5 \times 10^5 \frac{V}{W}$ (equivalent to $\mathbb{RG}$) such that

$$V_{\text{NEP floor}_{\text{C5658}}} = 1.3 \times 10^{-7}\frac{V}{\sqrt{Hz}}. \tag{9.28}$$

Finally, multiplying by a transfer factor which considers this specific detection sensitivity,

$$\frac{dp}{dV}_{w_{C5658}} = -6.8MPa/V, \tag{9.29}$$

$$\frac{dp}{dV}_{a_{C5658}} = -0.071MPa/V, \tag{9.30}$$

one obtains the power spectral density of the photodetector's noise of

$$p_{\text{NEP flooFr}_{\text{C5658}_w}} = \frac{8.6}{P_{laser}}\frac{Pa}{\sqrt{Hz}}, \tag{9.31}$$

$$p_{\text{NEP floor}_{\text{C5658}_a}} = \frac{0.089}{P_{laser}}\frac{Pa}{\sqrt{Hz}}. \tag{9.32}$$

For a laser power of 270mW and water as the test fluid, this gives a noise floor of

$$p_{\text{NEP floor}_{\text{C5658}_w}} = 32\frac{Pa}{\sqrt{Hz}}. \tag{9.33}$$

One notices that this photodetector has a significantly lower noise than the Thorlabs photodetector by an order of magnitude. However, there are inherent weaknesses to avalanche photodiodes. The output voltage varies non-linearly with incident optical power, and the avalanche multiplication effect quickly leads to detector saturation. A substantial reverse bias voltage is also required for operation. From a practical standpoint, the specific avalanche detector that was considered is not optical fibre-coupled and would necessitate a more complex mechanical assembly for measuring light coming out of the optical fibre interferometer.

9.2.3 Optical Shot Noise

The shot noise is a fundamental limit which is caused by the discrete nature of electromagnetic elemental particles, namely electrons and photons. Within an optical measurement system, shot noise is usually caused by fluctuations in the number of photons detected by the photodetector per unit time, or stochastic fluctuations in the number of electrons transmitted in an electrical signal [44]. In an ideal measurement system, this will be the limiting noise source.

In an optical system, the shot noise power spectral density is given by

$$P_{shot} = \sqrt{2h\nu\bar{P}}\left[\frac{W}{\sqrt{Hz}}\right], \tag{9.34}$$

with hv representing the photon energy with h as Planck's constant and $\nu = \frac{c}{\lambda}$ as the laser frequency with c as the speed of light and λ the laser wavelength, and $\bar{P}$ is the average optical power incident on the detector. For the current system, one can calculate the average optical power as

$$\bar{P} = 0.25 P_{laser} R_3 A_{loss}, \tag{9.35}$$

which is taken from (8.13). R_3 takes a value of $R_3 = 0.002$ for water, and $R_3 = 0.034$ in air. For a lossless system with a laser power of 270mW such as that used in the current setup, the average optical power considering water-based measurements is

$$\bar{P_w} = 0.135mW, \tag{9.36}$$

and considering air-based measurements this becomes

$$\bar{P_a} = 2.315mW. \tag{9.37}$$

The shot noise at the photodetector in the current setup then becomes

$$P_{shot} = \sqrt{2 \times 6.6 \times 10^{-34} \times \frac{299000000}{785 \times 10^{-9}} \times 0.14 \times 10^{-3}} \tag{9.38}$$

$$P_{shot} = \sqrt{6.8 \times 10^{-23}} \left[\frac{W}{\sqrt{Hz}} \right] \tag{9.39}$$

$$P_{shot} = 8.3 \times 10^{-12} \left[\frac{\mathrm{W}}{\sqrt{\mathrm{Hz}}} \right] \tag{9.40}$$

Using the transfer factor found previously, this value can be converted to voltage and pressure units by multiplying by the responsivity and gain, such that in water one obtains

$$\boxed{V_{shot} = 3.5 \times 10^{-8} \frac{V}{\sqrt{Hz}},} \tag{9.41}$$

$$\boxed{p_{shot} = \frac{14}{P_{laser}} \frac{Pa}{\sqrt{Hz}}.} \tag{9.42}$$

For a laser power of 270mW, this gives a noise floor of

$$\boxed{p_{shot_{270mw}} = 53 \frac{Pa}{\sqrt{Hz}}} \tag{9.43}$$

From the obtained noise floors for the photodetector shot noise, one notices that the Thorlabs photodetector's noise is higher than the shot noise by a factor of 4. Ideally, however, the Hamamatsu photodetector noise is lower than the shot noise by about a similar factor, meaning that the Hamamatsu photodetector is shot noise-limited, and further reduction of this photodetector's noise floor is not possible.

9.2.4 Oscilloscope Voltage Noise

The fundamental noise limit of the oscilloscope is determined by the shot noise and the Johnson-Nyquist noise. The shot noise is caused by the discrete nature of charge carriers which for the oscilloscope are the electrons transmitted through wires and the random fluctuations in the number of electrons which arrive at the oscilloscope during each measurement period. The Johnson-Nyquist noise is caused by the finite electronic component impedance within the input front end, which affects thermal agitation of charge carriers. For a given component resistance R, the Johnson noise can be mathematically written as

$$V = \sqrt{4 k_B T R} \left[\frac{V}{\sqrt{Hz}} \right], \tag{9.44}$$

in which V is the root mean square of the voltage, k_B is Boltzmann's Constant, and T is the temperature. For the oscilloscope, one expects the Johnson-Nyquist noise to be higher than the shot noise, and thus be the fundamental noise limit.

In addition to fundamental sources of noise, the oscilloscope is affected by other noise, primarily the timing error and the vertical noise induced by the amplifier. The timing error, also called jitter, is the deviation between any given clock cycle and the ideal average clock cycle. Jitter can be transformed into an amplitude noise during measurements of sharp slopes in voltage, such as during the measurement of a shock wave, where a slight offset in measurement time will result in the measurement of a voltage which is either higher or lower than the value at the proper time. The amplifier induces another source of noise during the amplification of the voltage. The noise specification for oscilloscopes can be quite complicated due to the presence of these noise sources, and the specification is rarely given in units of $\mathrm{V}/\sqrt{\mathrm{Hz}}$. The noise of the oscilloscope is therefore measured using a 50 Ω Bayonet Neill–Concelman (BNC) cap placed on the oscilloscope's input. The time trace is shown in Figure 9.5. A Fourier Transform is applied to the time traces and plotted in Figure 9.6 to view the waveform in the frequency domain. A high-frequency noise around 40 $\mathrm{Pa}/\sqrt{\mathrm{Hz}}$ is found. By comparing this value to the optical shot noise of the photodetector, it is easy to conclude that any improvement to the oscilloscope input noise will yield no improvement to the system as the oscilloscope noise is already lower than the optical shot noise.

9.2.5 Laser Noise

The laser diode has no easily accessible noise metric and is negatively impacted by a multitude of effects : intrinsic intensity noise, phase noise interacting with parasitic cavities in the interferometer, and self-mixing noise. These sources of noise are described below, but due to their random and parasitic nature, a direct measurement of the laser noise,

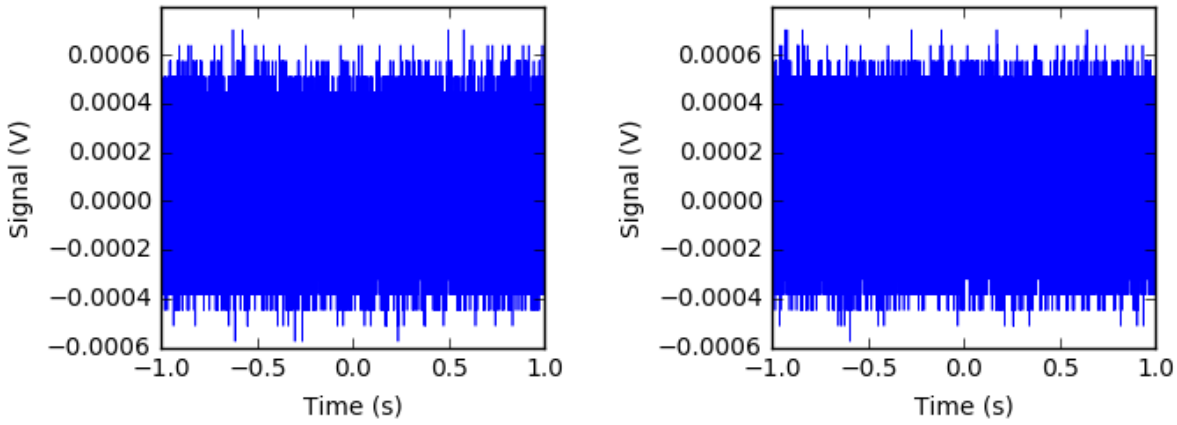

(a) (b)

Figure 9.5: Typical time traces of the voltage signal measured to experimentally characterize the oscilloscope noise. The full collection of traces is available in Appendix C.

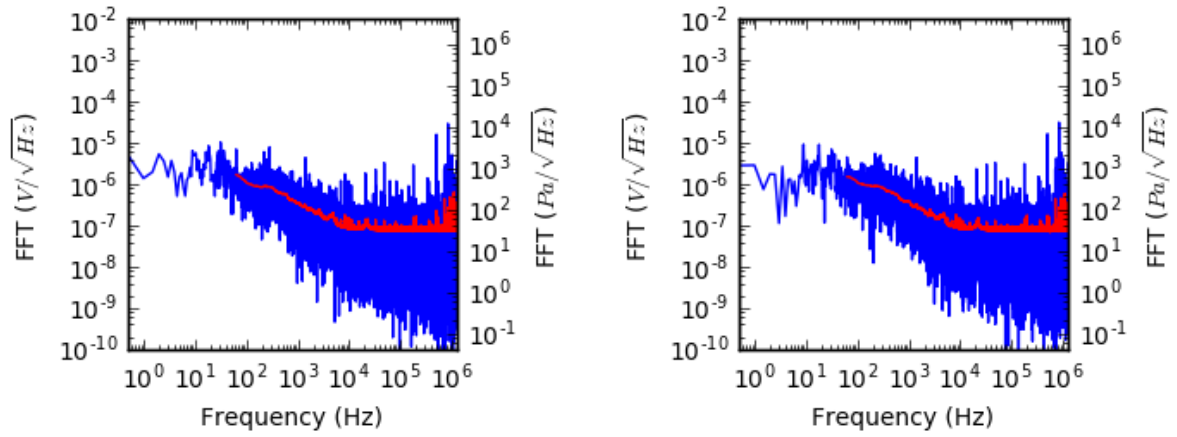

(a) (b)

Figure 9.6: The voltage and pressure spectrum of the oscilloscope noise measurements plotted against the frequency. The red curve is a 256-bin moving average of the FFT spectrum. One notices that white noise is obtained at high frequencies.

interfaced with the rest of the system, is necessary to properly characterize this component and will be presented in section 9.3.

Since the system measures changes of reflectivity at the tip of the optical fibre, the phase noise of the system (i.e. noise that corresponds to changes in wavelength) is theoretically negligible. However, phase noise becomes important for systems with long parasitic cavities, such as those arising from parasitic reflection at the multiple optical fibre connections within the interferometer. These cavities can transform small wavelength shifts into considerable amplitude signal variations that are almost impossible to quantify without a direct measurement.

The self-mixing noise of the system results from stray light reflected back to the laser diode and interfering with the optical gain medium. In this system, due to cost constraints, no optical isolator is present to protect the laser from reflected light. Optical isolators are common at telecommunication wavelengths (such as 1550 nm) but are much more expensive at visible wavelengths such as that used in this setup. As with the phase noise, the self mixing noise influences the measured amplitude of the optical beam. The effect of self-mixing noise on lasers is to reduce coherence of the laser output, as single-mode lasers will oscillate in multimode as the amount of stray light increases, in addition of increasing variation of the laser optical power output [42]. Due to the phase-dependence of self-mixing noise, one can also expect the appearance of resonant peaks in the frequency response located at frequencies related to the round-trip time of the reflected light.

Another effect which further increases the noise of the laser is mode hops. These are sudden changes in the resonator cavity mode of the laser, which can affect the signal amplitude read by the oscilloscope. These phenomena are heavily affected by case temperature and optical feedback and can occur erratically. Lasers that do not present such mode hops are sold as "mode-hop-free", which is not the case for the present system. Mode-hops can be subtracted from the measured signal using a differential detector, or removed in post-processing using the optional photodetector shown in Figure 8.1.

Another source of noise affecting the laser is the laser amplitude noise, normally characterized by the Relative Intensity Noise (RIN). When setting the optical power output of the laser diode, the actual laser power varies around the set power due to effects intrinsic to the laser diode. The RIN characterizes the noise of the laser by comparing these fluctuations in power δP compared to the average power $\bar{P}$, as

$$\text{RIN} = \frac{\delta P}{\bar{P}}. \tag{9.45}$$

This metric must be experimentally measured at the system's set optical power, as the RIN is optical power-dependant. The setup used to measure the RIN consists of the laser diode directly connected to the photodetector, with attenuation placed between the two components if required. For the laser power of 270 mW which is considered in the setup, an attenuation of 42 dB is required to not exceed the photodetector saturation limit of 2.38 mW. Much like optical isolators, fibre-coupled attenuators are also very expensive at visible light wavelengths when compared to telecom wavelengths. A measurement of the RIN could be done by reducing the laser drive current, however this would not be representative of the laser instability at 270 mW. Thus, no measurement of the RIN is performed. The total noise of the assembled system is measured in section 9.3 is used to characterize all the aforementioned effects within the system, in addition to component noise and the fibre noise.

9.3 Measured System Noise

A measurement is taken of the noise produced by the entire assembled system to experimentally quantify the theoretical noise described in section 9.2. Four main sources of noise are automatically included in this measurement : the amplitude and phase noise of the laser, the self-mixing noise of the system, mode-hopping of the laser diode, the component

noise added by the photodetector and the oscilloscope.

To characterize the combined effect of all these noise sources, the system sketched in Figure 8.1 is used, with the measurement tip immersed in water as it is less sensitive to pressure variations caused by any background noise such as vibrations from the oscilloscope fan. A laser dump is connected to the optional tip to minimize light reflection. Multiple 2-second signals are measured at a 250 MHz sampling rate and plotted in Figure 9.7. These signals are measured for a laser power of 270 mW using an AC-coupled input on the oscilloscope, with the fibre-tip immersed in water without any incident pressure waves. By using an AC-coupled input on the oscilloscope, the optical power variation around its average is measured.

The time traces contain a high density of mode hops. These mode hops are partially attributed to the lack of an optical isolator between the laser driver and the remainder of the system, however these would most likely still be present, but with reduced occurrence, with the addition of an isolator. The most effective method of eliminating this noise source is the addition of an additional reference detector or the inclusion of a differential detector and measure the occurrence of this effect.

A Fast Fourier Transfer (FFT) is performed on the measured signals shown in Figure 9.7 to obtain their power spectrum in the frequency domain. This power spectrum is plotted in Figure 9.8. The trace of a 256-point moving average is plotted in red, and is more representative of the noise than the full FFT trace shown in blue. For the current study, one can discard the 1/f low-frequency portion of the FFT as this region is less important to the high-frequency measurements sought, and instead study the high-frequency region consisting of frequencies larger than 10 kHz. The FFT spectrum plotted in Figure 9.8 allows for the measurement of the system noise, with a noise floor around 6.5×10^{-7} $\mathrm{V}/\sqrt{\mathrm{Hz}}$, or 260 $\mathrm{Pa}/\sqrt{\mathrm{Hz}}$, in the high-frequency regime.

From the system noise measured as 260 $\mathrm{Pa}/\sqrt{\mathrm{Hz}}$, and the photodetector noise calculated

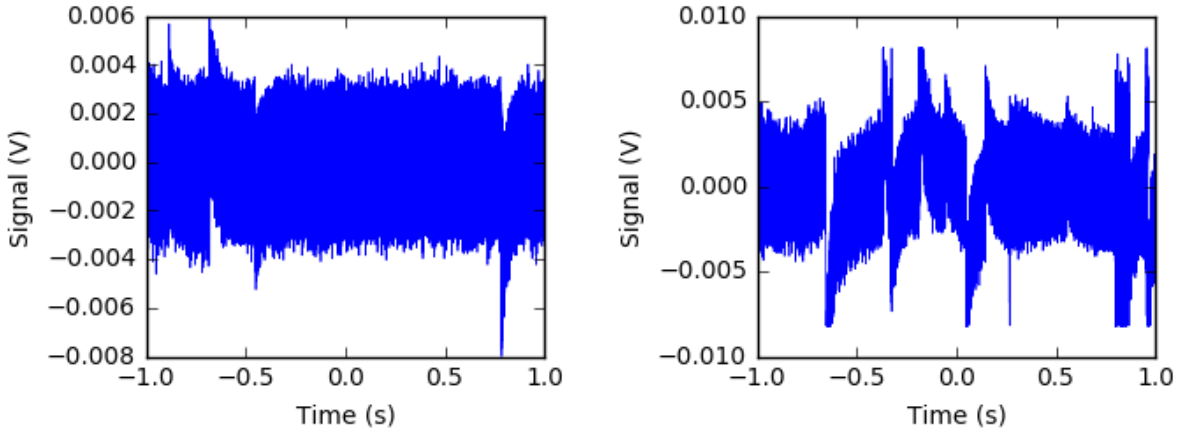

(a) (b)

Figure 9.7: Typical time traces of the voltage signal measured to experimentally characterize the system noise. Note the fairly frequent mode-hops present in the second signal trace, which could be subtracted by using a reference detector. The full collection of traces is available in Appendix C.

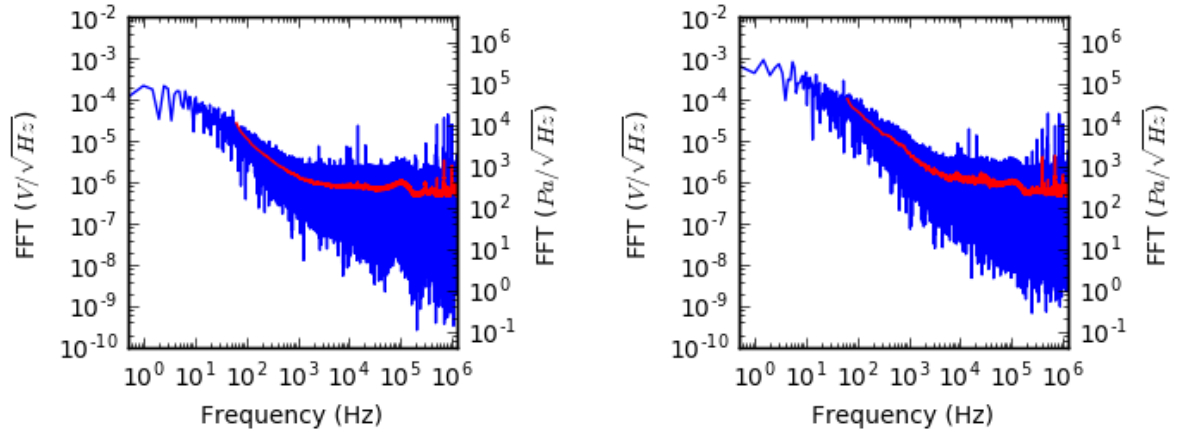

(a) (b)

Figure 9.8: The voltage and pressure spectrum of the system noise measurements plotted against the frequency. The red curve is a 256-bin moving average of the FFT spectrum.

as 215 Pa/$\sqrt{\text{Hz}}$ in section 9.2.2, one can calculate the laser noise as

$$p_{laser} = \sqrt{p_{system}^2 - p_{det}^2} = 150 \frac{\text{Pa}}{\sqrt{\text{Hz}}}. \tag{9.46}$$

The laser noise is thus not the dominant effect limiting the system but is comparable to the photodetector noise. Improvement to the system would need to first improve the photodetector before eliminating the effects discussed in section 9.2.5. The measurement of the system noise used in (9.46) also includes other sources of noise beyond the photodetector and laser noise.

9.3.0.1 Fibre Losses

A potentially important source of noise which has not yet been discussed is the noise introduced by the fibre itself. This loss is the combination of attenuation, material absorption losses, Rayleigh scattering, and waveguide imperfections. Attenuation losses are

The material absorption comes in two forms, be it intrinsic and extrinsic absorption. Intrinsic material absorption refers to the absorption of light by the fused silica. This absorption over long distances, such as in telecommunications will generally add a loss below 0.1 dB/km for the considered wavelength [45]. Extrinsic absorption refers to the absorption of light by impurities in the silica fibre. The material absorption losses are considered negligible in this study due to the short length and high purity of the optical fibres.

Rayleigh scattering appears due to microscopic fluctuations in density appearing during fibre fabrication and is a fundamental fibre loss. This fundamental loss is the dominating source of fibre noise for wavelengths under 1.55 μm [45]. This fluctuation of the refractive index due to changes in density occurs on a scale smaller than the optical wavelength. At the system's wavelength, these losses are around 3 dB/km [45].

Waveguide imperfections also add losses to the measurement system due to the assump-

tion of total internal reflection within the fibre. Near a fibre bend, the angle of incidence of a ray of light reflecting off the core-cladding interface can decrease to become less than the critical angle, and transmit through to the cladding. For single-mode fibres, macroscopic bending losses are negligible.

The fibre loss is included in the measurement of the system noise, as this quantity includes each loss present in the assembled system. However, when calculating the laser noise in (9.46), the fibre losses are not included. As the current system has a fibre length on the order of tens of meters, the fibre losses can be estimated to add around -0.03 dB based on the values given by Agrawal [45], which is negligible in comparison to the oscilloscope and laser noise.

9.3.0.2 Low-Frequency Noise

The noise measurements taken in sections 9.2.4 and 9.3 only consider the high-frequency noise limit of the system. Neglecting the low-frequency noise, also known as the 1/f noise, is justified by the high bandwidth required to resolve a wave in the pressure range of interest. These waves require measurement bandwidths of 86 MHz to 300 MHz to resolve with three measurement points. To verify this assumption, one can integrate the noise floor over the measurement bandwidth for the system noise measurements. Figure 9.9 shows the system noise integrated over the measurement bandwidth, plotted alongside the integrated high-frequency white noise limit. This allows the visualization of the deviation of the system noise from the assumed high-frequency white noise. At low frequencies under 100 kHz, one can see the very large contribution of the 1/f noise to the total noise of the system, as the high-frequency white noise limit fails to properly describe the system noise. However, at frequencies over 100 kHz, the white noise limit is an accurate representation of the system noise, varying from the integrated noise floor by under 3% at 100 kHz, and under 2% over 1 MHz.

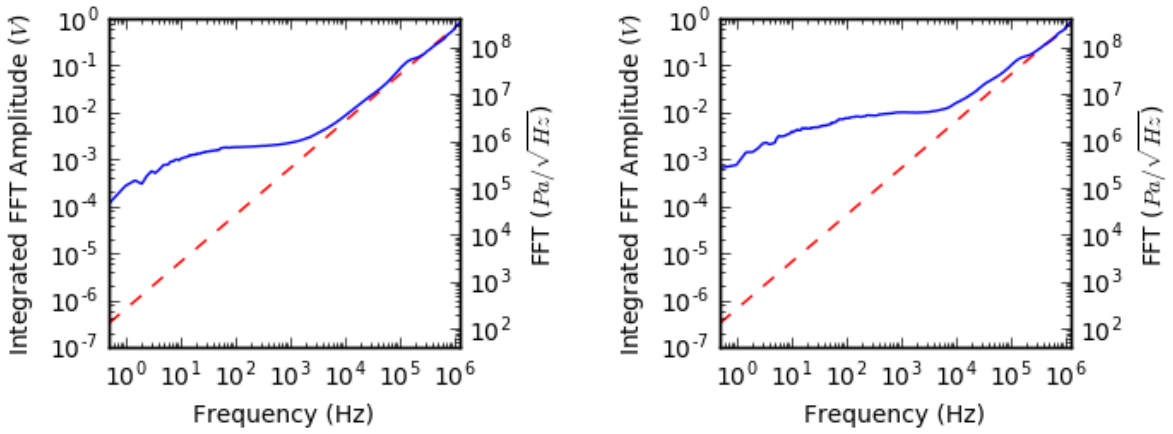

(a) (b)

Figure 9.9: System noise floor integrated over the measurement bandwidth (blue), shown alongside the high-frequency white noise (red), plotted as a function of the measurement bandwidth. For measurement bandwidths above a certain frequency, the high-frequency noise limit is a good approximation of the system noise to within 3%.

9.4 Summary

Table 9.1 summarizes the noise sources of the hydrophone in both pressure units and specified units. The noise limitations of the hydrophone are also graphically summarized in Figure 9.10. Subfigure 9.10 a) presents the noise floor, in kPa, for the assembled system and for each component as a function of the measurement bandwidth. As discussed above in section 9.1, each bandwidth corresponds to a minimum resolvable shock thickness and post-shock pressure, which are also indicated on the x-axis. This relation was discussed in Figure 9.2, but for convenience it is reproduced in Figure 9.10 b) and c). In Figure 9.10 a), The black curve represents a signal-to-noise ratio (SNR) of 1. For the hydrophone to yield a meaningful measurement for the current purpose - i.e., resolving the shock wave thickness - the total noise of the system must be situated under this line, in the unshaded region. This is clearly not the case here.

We therefore conclude that in its current implementation, the hydrophone will not work as is for the purpose of resolving a shock wave associated with the critical threshold for blast-induced neuro-trauma. Moreover, as discussed in more details below, no individual

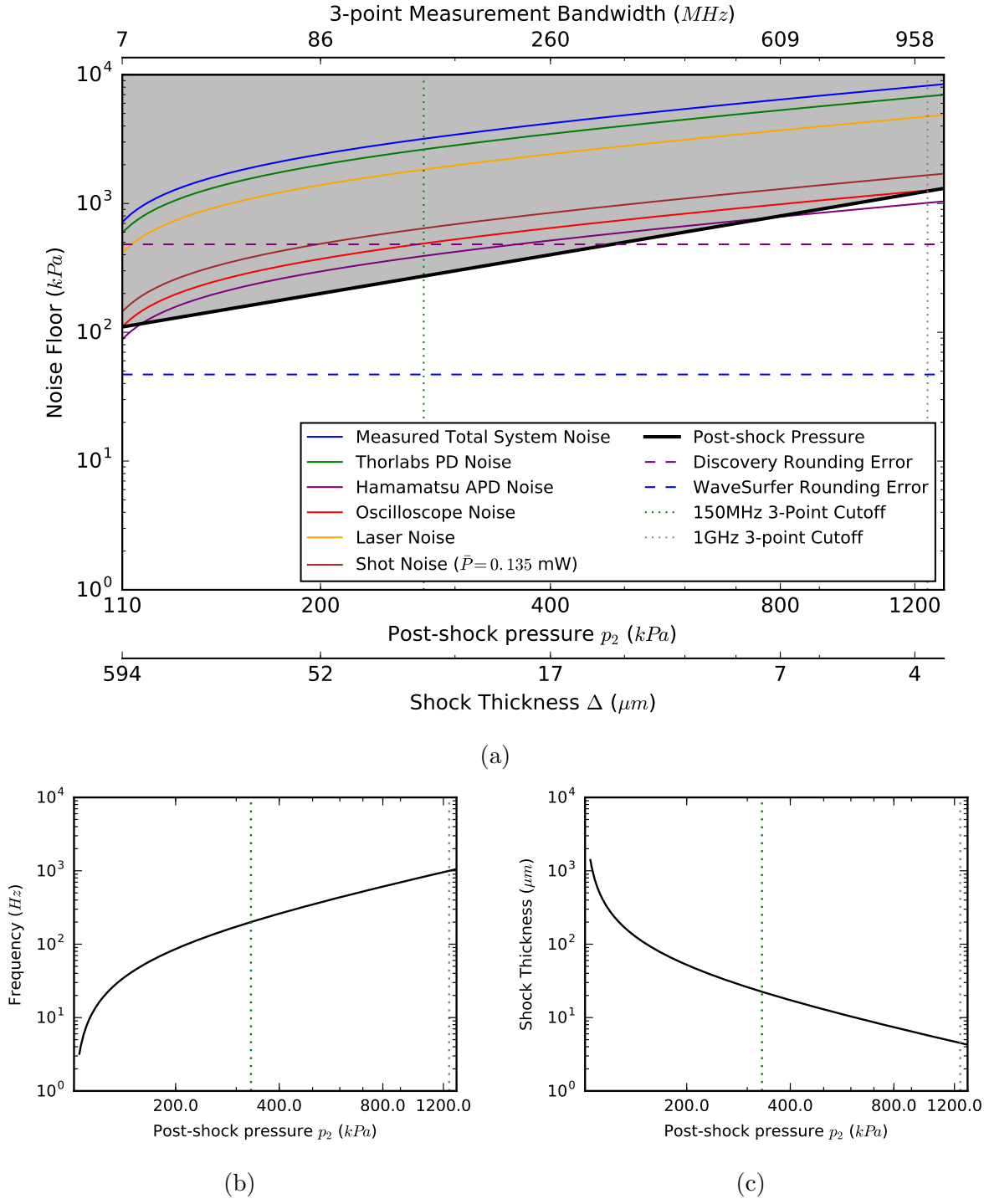

Figure 9.10: a) Integrated noise floor plotted as a function of the shock overpressure. The shock thickness and 3-point measurement bandwidth are shown for reference. Vertical dotted lines are placed at $f = 150$ MHz and $f = 1$ GHz for reference. The total system noise was measured using the Thorlabs photodetector. b) Measurement bandwidth required for a 3-point resolution plotted against the post-shock pressure. c) The shock thickness plotted against the post-shock pressure.

Table 9.1: Summary of the calculated noise contribution of each system component, given in both specified/measured units and converted to pressure units.

Noise Source	Component	Specified units	Pressure units
Oscilloscope Voltage Noise	Oscilloscope (LeCroy)	$9.8 \times 10^{-8}\ \frac{V}{\sqrt{Hz}}$	$40\ \frac{Pa}{\sqrt{Hz}}$
Noise Equivalent Power	Photodetector (C5658)	$5.0 \times 10^{-11}\ \frac{W}{\sqrt{Hz}}$	$32\ \frac{Pa}{\sqrt{Hz}}$
Noise Equivalent Power	Photodetector (APD10A2)	$3.4 \times 10^{-11}\ \frac{W}{\sqrt{Hz}}$	$215\ \frac{Pa}{\sqrt{Hz}}$
Optical Shot Noise	Photodetector	$3.5 \times 10^{-8}\ \frac{V}{\sqrt{Hz}}$	$53\ \frac{Pa}{\sqrt{Hz}}$
Laser Noise	Laser & Fibres	$3.7 \times 10^{-7}\ \frac{V}{\sqrt{Hz}}$	$150\ \frac{Pa}{\sqrt{Hz}}$
System Noise	System	$6.4{\times}10^{-7}\ \frac{V}{\sqrt{Hz}}$	$260\ \frac{Pa}{\sqrt{Hz}}$
Bit Digitization Limit	Oscilloscope (LeCroy)	$31\ \mu V$	$47\ kPa$
Bit Digitization Limit	Oscilloscope (AD2)	$31\ \mu V$	$47\ kPa$

component improvement could potentially improve the system significantly enough to reach a SNR > 1. Even by improving everything down to the fundamental optical shot noise, performance remains at a SNR ≈ 0.1. The shot noise can be reduced by increasing the laser power, but improvements scale slowly, with the square root of the laser power increase. Tuning this knob is therefore unrealistic, given that we already work a laser power that is very high in the context of optical fibre-coupled systems.

The topmost plotted curve in Figure 9.10 a) is the system noise measured in section 9.3, representing the entire system. Immediately under this curve one sees the curve representing the noise introduced by the Thorlabs photodetector, calculated in section 9.2.2. This is the highest noise source associated with a single component, and is therefore system-limiting. Immediately following this curve, however, is the noise associated with the laser. Improving the photodetector would thus yield the greatest effect on the overall system, however both the laser and the photodetector must be improved to reach the system's fundamental noise limit. This limit is the shot noise associated with the photodetector for the average power of 0.135 mW, as calculated in section 9.2.3. This source of noise is only a factor 4 smaller than the Thorlabs photodetector, and reducing the noise of the photodetector past this fundamental limit is not possible. The only way to reach a high enough SNR for meaningful measurements is to improve the V/Pa sensitivity of the sys-

tem by designing a different pressure transduction mechanism, which will be discussed in section 9.4.1.

It is also insightful to look at the other noise source. The rounding error of the oscilloscopes calculated in section 9.2.1, is plotted as horizontal dotted lines. This limiting factor is not bandwidth dependent, and one sees that the Analog Discovery does not offer a resolution which will ever allow for the measurement of the post-shock state within its bandwidth of 100 MHz. In contrast, the Wavesurfer has a rounding error which is smaller than all other noise curves plotted in this graph, meaning that this oscilloscope does not limit the system's noise floor.

The oscilloscope noise measured in section 9.2.4 is slightly smaller than the shot noise of the photodetector, thus any reduction of the oscilloscope noise will not meaningfully improve the system. Finally, one sees the specified Hamamstsu photodetector noise under no illumination is roughly a quarter of the optical shot noise associated with the incident laser power. This component is therefore shot-noise limited and could allow a factor 4 improvement compared to the Thorlabs photodetector that was mainly used in this work. However, drawbacks of using a avalanche photodetector exists, as discussed previously in section 9.2.2. These include non-linear voltage output quickly leading to detector saturation, a substantial reverse bias, and a more complex mechanical assembly.

9.4.1 Sensitivity Enhancement

The only way to reach a high enough SNR is to improve the V/Pa sensitivity of the system by designing a different pressure transduction mechanism; this would affect the transfer factor elaborated in section 8.1 such that the voltage noise, which remains constant, corresponds with smaller pressures. Figure 9.11 a) plots the factor separating the measured system noise and the post-shock pressure curve in Figure 9.10. This is thus the increase in sensitivity required to obtain a signal-to-noise ratio of 1, across the pressure and frequency

range of interest. Due to the bell-shape of the curve, a maximum sensitivity factor increase of 12 is found for a post-shock pressure around 200kPa. However, if one seeks to perform measurements exclusively in the low-frequency range below 10 MHz or in the high frequency range above 800 MHz, a lower sensitivity factor increase of 7 would be required.

As previously mentioned, it is possible to increase the sensitivity and lower the noise floor by increasing the optical power output of the laser diode. For every noise metric calculated in this chapter, the noise calculated in units of $V/\sqrt{\text{Hz}}$ needs to be multiplied by the transfer factor shown in (8.18), which has the laser power in the denominator. The shot noise, which is the fundamental limiting noise source shown in (9.34), increases as the radical of the laser power. Therefore, the pressure noise of the system scales as

$$p_{noise} \propto \frac{1}{\sqrt{P_{\text{laser}}}}. \tag{9.47}$$

Decreasing the noise floor by a factor of approximately 12 is required for a SNR ≈ 1, which is achievable by increasing the laser power by a factor of 144. This is not feasible as a laser power of 39 W would be required. Alternatively, the pressure noise floor can be decreased by increasing the sensitivity. Due to the high sensitivity increase which is required to achieve an SNR ≈ 1, hydrophones assembled using uncoated fibres are unsuitable for the measurement of blast-induced neuro-trauma, despite their good spatial resolution and measurement bandwidth.

Increasing the sensitivity of hydrophones has been done previous works. In their hydrophone, Staudenraus & Eisenmenger used clear silicone and opaque silicone coatings on the fibre end-tip to increase the sensitivity by a factor of 7 and 30, respectively [34]. For much higher sensitivity increases, Wilkens and Koch developed a method of depositing a series of dielectric coatings to form an interferometer at the tip of the optical fibre [36]. Using this technique, a sensitivity increase factor of around 300 for a 15-layer end-tip coating, and around 100 for a 11-layer coating, were reported. Finally, Lewin proposed a method of

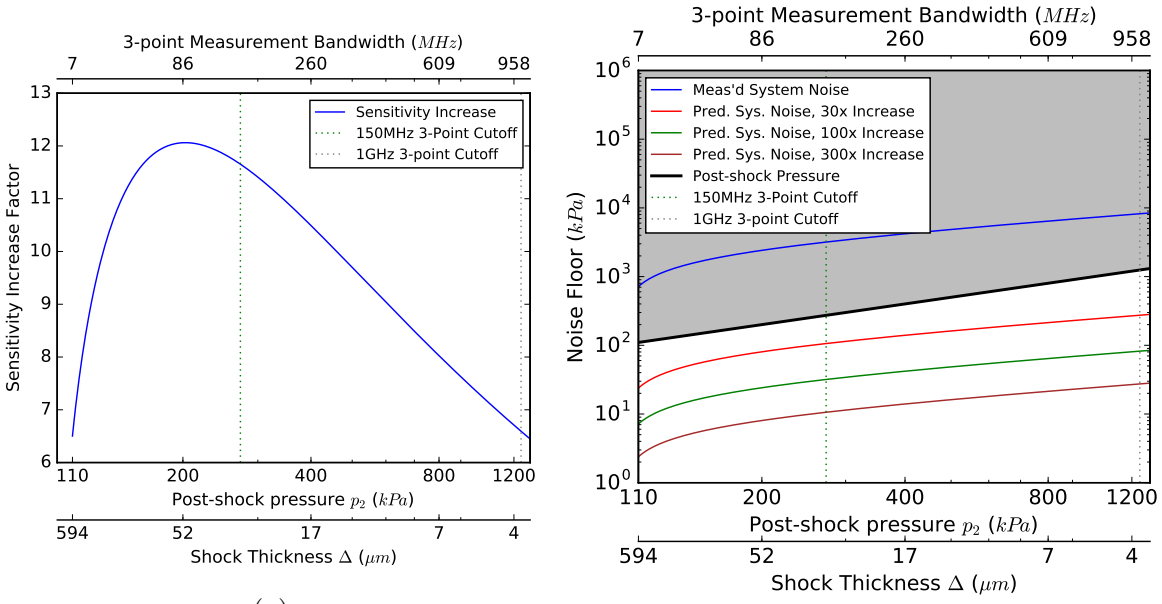

(a) (b)

Figure 9.11: a) Sensitivity increase factor required to reduce the system noise to obtain a signal-to-noise ratio of 1. b) Comparison between the predicted noise floors for specified sensitivity enhancements.

tapering the tip of a multimode fibre to increase the light collection compared to a single-mode fibre [32]. This method is found to offer a sensitivity increase of approximately 20 dB (factor of 100).

An estimation of the system noise considering these sensitivity increasing techniques are plotted in Figure 9.11 b), with the same x-axes as Figure 9.10. Placing an opaque silicon coating on the fibre end-tip increases the sensitivity of the measurement system by a factor of 30, placing the system noise curve slightly under the post-shock pressure. The interferometer coatings and the tapered tip offer a noise floor which are significantly lower than the post-shock pressure, with a sensitivity increase of 300 placing the noise floor at least two orders of magnitude smaller than the post-shock pressure. It is also possible to further improve the noise floor beyond the sensitivity increase factor obtained through end-tip coatings by improving individual system components, recalling that the total system noise is currently a factor 5 higher than the system's fundamental noise limit.

9.5 Current Capabilities

Despite the difficulties encountered when attempting to measure a pressure wave resolved with multiple points within the wave thickness, this sensor is capable of taking pressure readings at very high frequencies. When comparing this system to other fibre-optic hydrophones currently available, notably the FOPH 2000 from RP acoustics and the HFO-690 from ONDA, the measure of interest is the noise equivalent pressure. ONDA gives this metric as 50 Pa/$\sqrt{\text{Hz}}$ at 100 MHz, 95 Pa/$\sqrt{\text{Hz}}$ at 10 MHz, and 175 Pa/$\sqrt{\text{Hz}}$ at 2 MHz bandwidths. These vary between a factor of 1.5 to 5 smaller than the total system noise of the current setup. This system uses fibres which have a diameter of 100 μm, which is much larger than those used in the current system and have a spatial resolution which is much larger than the shock thickness in the range of interest as previously shown in Figure 9.2. The second commercially-available alternative, from Precision Acoustics, has a measurement bandwidth of 50 MHz and a fibre diameter of 10 μm [46]. The noise equivalent pressure is given as 15 kPa at 5 MHz, for a noise of 6.7 Pa/$\sqrt{\text{Hz}}$, which is significantly lower than that of the current system by a factor of approximately 39, however this measurement system is hindered by its low bandwidth in the current context which is incapable of resolving the critical region associated with blast-induced neuro-trauma. Figure 9.12 shows the noise floor of the current tool integrated over its bandwidth, and compares this with specifications available for commercially-available alternatives. It is worth noting that applying a sensitivity enhancement to the fibre tip would decrease the current system noise floor below these commercially-available alternatives, while maintaining an equal or greater measurement bandwidth and a superior spatial resolution.

Other fibre-optic hydrophones which have been developed by research groups have sensitivities comparable to that of the current work, be it Parsons setup's 0.8 mV/MPa or Lewin's 4.3 mV/MPa. Parsons gives a minimum detectable pressure of 900 kPa at the maximum 50 MHz bandwidth [31], yielding a noise of 130 Pa/$\sqrt{\text{Hz}}$. By applying

their reported transfer factor, this becomes to 9.9×10^{-8} V/$\sqrt{\text{Hz}}$, which is smaller by a factor of 6.5 than the current system noise floor of 6.4×10^{-7} V/$\sqrt{\text{Hz}}$. Recalling Figure 9.4, one notes that bandwidths of 50 MHz cannot resolve the waves associated with blast-induced neuro-trauma, and higher bandwidths are required to resolve the region of interest. An alternative measurement system was developed by Mu and co-workers [33], which is also used by Lewin's development of a sensitivity-enhancing down-tapered fibre-tip [32]. Lewin gives a noise floor of -80 dBm for measurements at 4 kHz, yielding a noise floor of 1.5×10^{-13} W/$\sqrt{\text{Hz}}$. Their system was designed for measurements at 100 MHz, however their bandwidth could be extended beyond this value due to the usage of a 1 GHz avalanche photodetector. The current system's shot noise has a level of 8.3×10^{-12} W/$\sqrt{\text{Hz}}$, which is still larger by a factor of 55. This discrepancy is in part caused by of our system's higher laser power on the shot noise metric when expressed as an optical power spectrum, and by the dependence on the average reflected optical power calculated at the end-tip using Fresnel's Law. It is worth noting that a higher laser power has a desirable effect on the noise expressed in units of Pa/$\sqrt{\text{Hz}}$, improving the noise floor as the radical of the optical power. Notwithstanding the differences in laser power and in the refractive indices used to calculate the end-tip reflection, the noise floor of this system is a factor 20 smaller than the shot noise of our current setup.

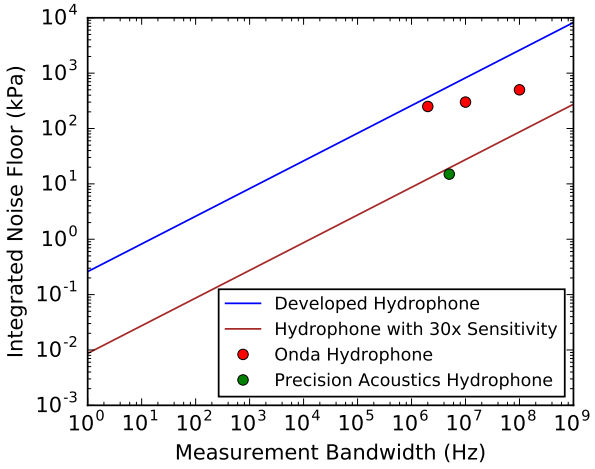

(a)

Figure 9.12: a) Integrated noise floor as a function of the measurement bandwidth, for cases where time-resolved measurements of pressure are not required.

9.6 Conclusion

A fibre-optic hydrophone for resolving shock waves associated with blast-induced neuro-trauma was designed, assembled, and subsequently characterized. A gasdynamic description of shock waves is used to determine the wave thickness and residence time, finding that the assembled system can properly resolve the lengthscales and timescales associated with the 100 kPa - 350 kPa region of interest for blast-induced neuro-trauma. The developed system is able to place multiple measurement points within the thickness of the shock wave in this region, giving an accurate measurement of the wave thickness. A measurement bandwidth of 150 MHz allows 3 points to be placed within a propagating shock wave with an over-pressure of 175 kPa, while a 1 GHz measurement bandwidth increases this to a wave with an over-pressure of over 1100 kPa.

To better quantify the performance of our measurement system, a detailed analysis of the various sources of noise is performed. The photodetector found to be the system-limiting component, although its noise floor is only a factor 4 higher than the universal shot noise limit at our operating optical power. The greatest possible noise floor improvement from component upgrades would only be a factor 5, and would be achieved by using a shot-noise limited photodetector and a low-noise laser diode. As such, we find that a bare-fibre hydrophone is unable to resolve the wave pressure profile in our range of interest, since the hydrophone minimum detectable pressure is typically 12 times higher than the wave post-shock pressure. Nevertheless, our measurement tool is capable of resolving the time and length scales required when measuring shock waves, which is not the case for commercially-available alternatives despite these alternatives having lower noise equivalent pressures than the current tool. For resolving pressure, previous works on hydrophones have studied sensitivity-enhancing fibre coatings, enabling an increase of 30× - 300×. Future work implementing such end-tip coatings will be essential for resolving pressures in the range of interest, while maintaining the already-suitable spatial resolution and bandwidth.

APPENDICES

Appendix A

Experimental Visualization of Shock Tube Experiments

A.1 Hydrogen Experiments

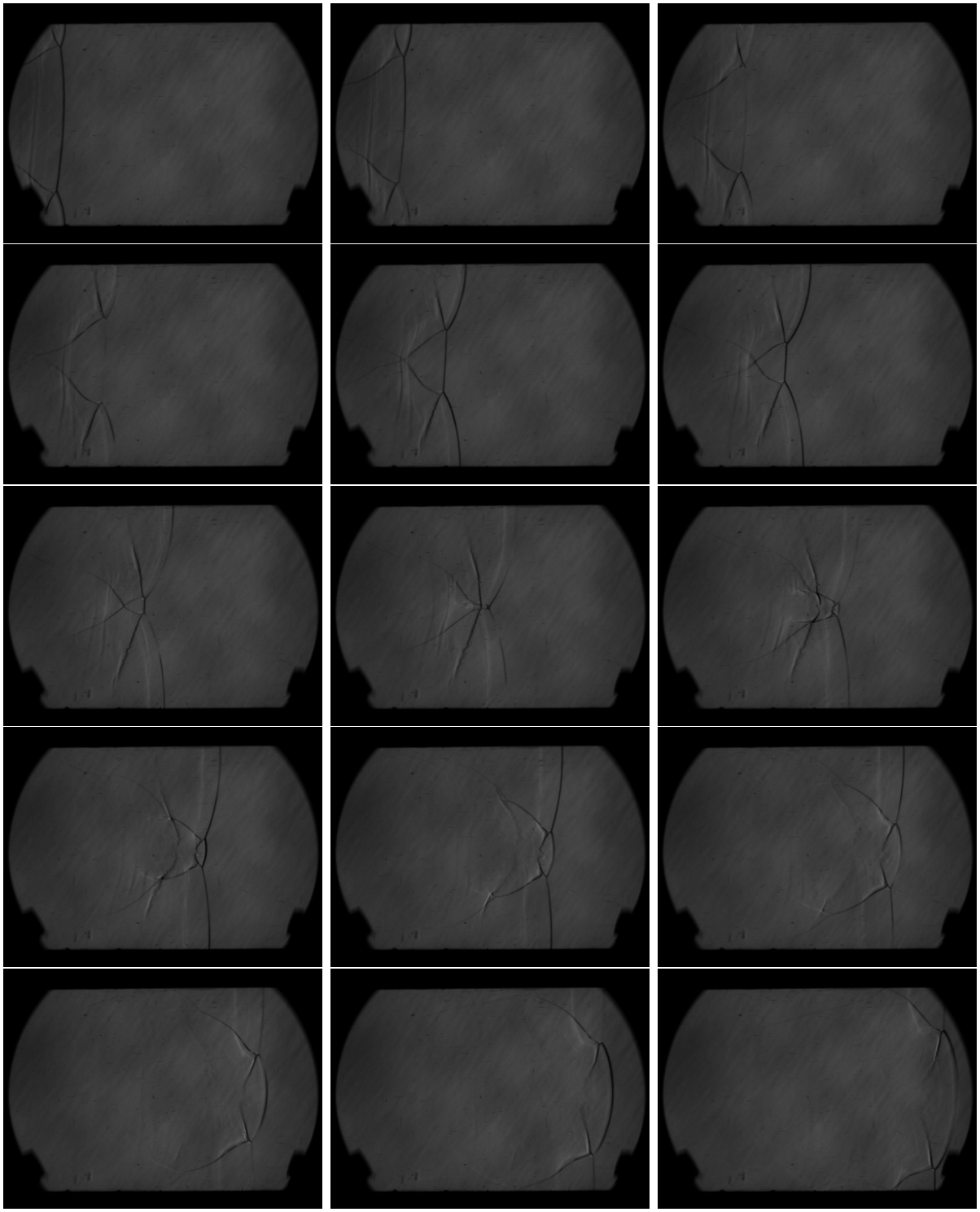

Figure A.1: Summary of an experiment 0_H2 performed in $2H_2 + O_2 + 7Ar$. Taken from Xiao and co-workers [1].

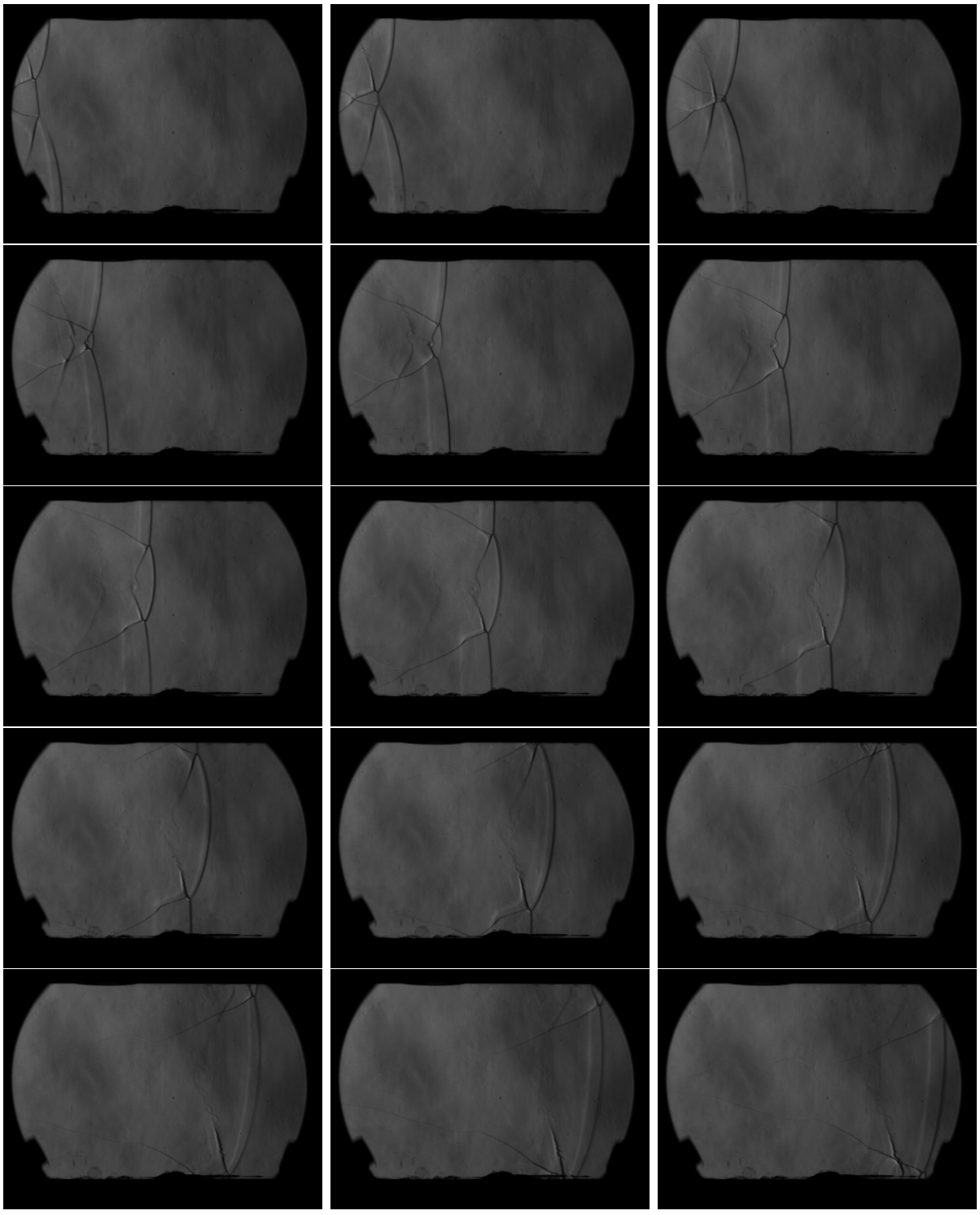

Figure A.2: Summary of experiment 5_H2 performed in $2H_2 + O_2 + 7Ar$.

A.2 Methane Experiments

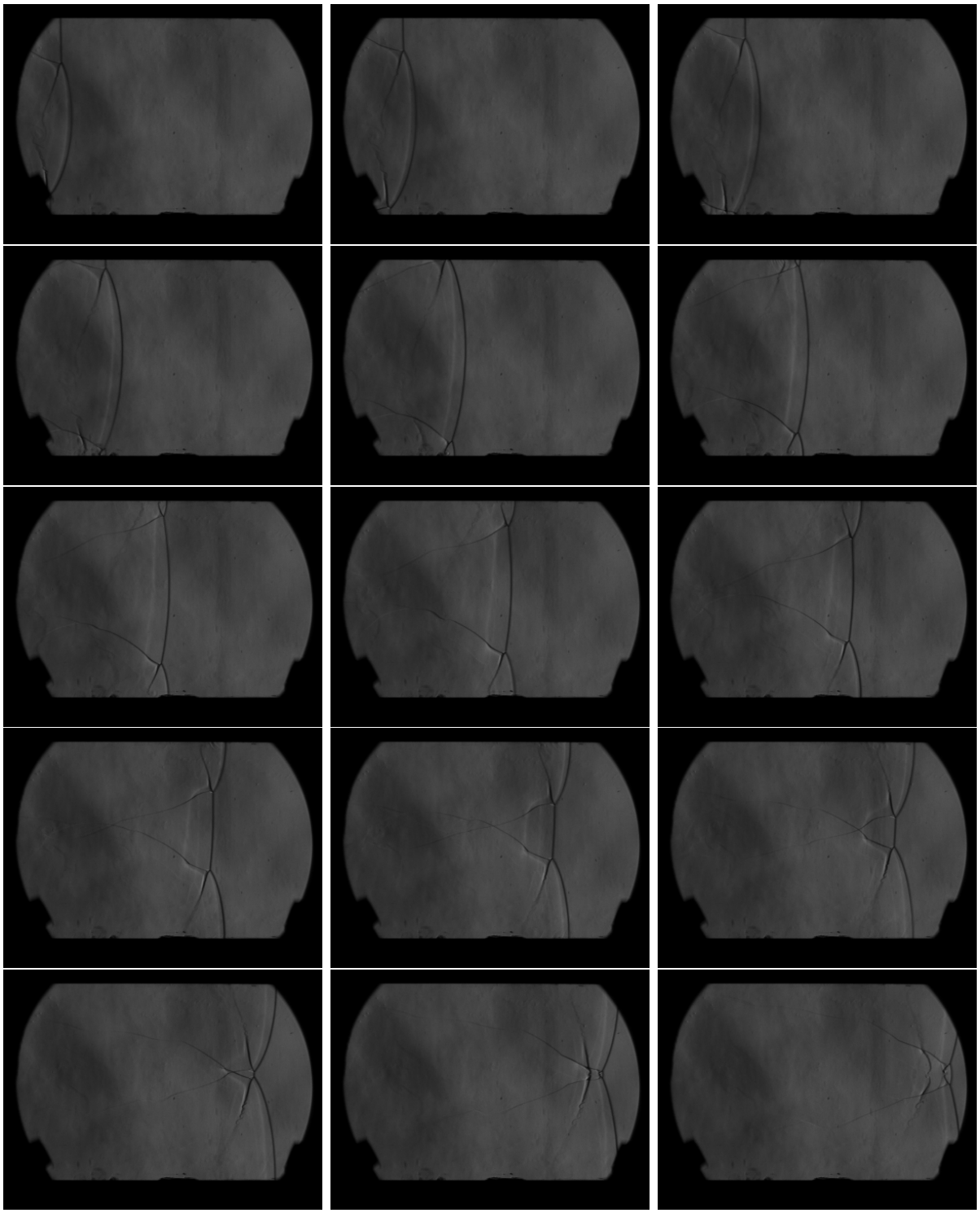

Figure A.3: Summary of experiment 11_H2 performed in $2H_2 + O_2 + 7Ar$.

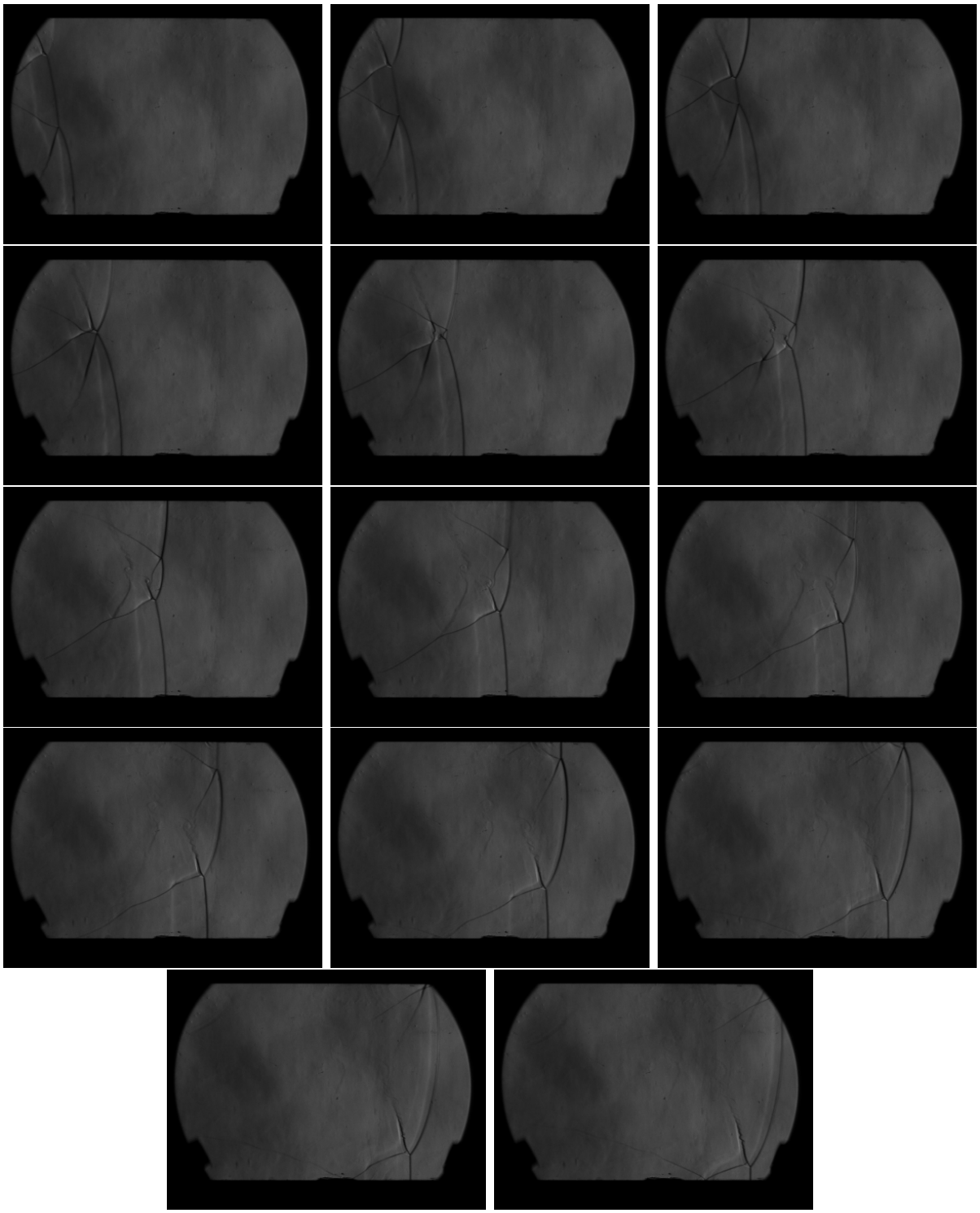

Figure A.4: Summary of experiment 13_H2 performed in $2H_2 + O_2 + 7Ar$.

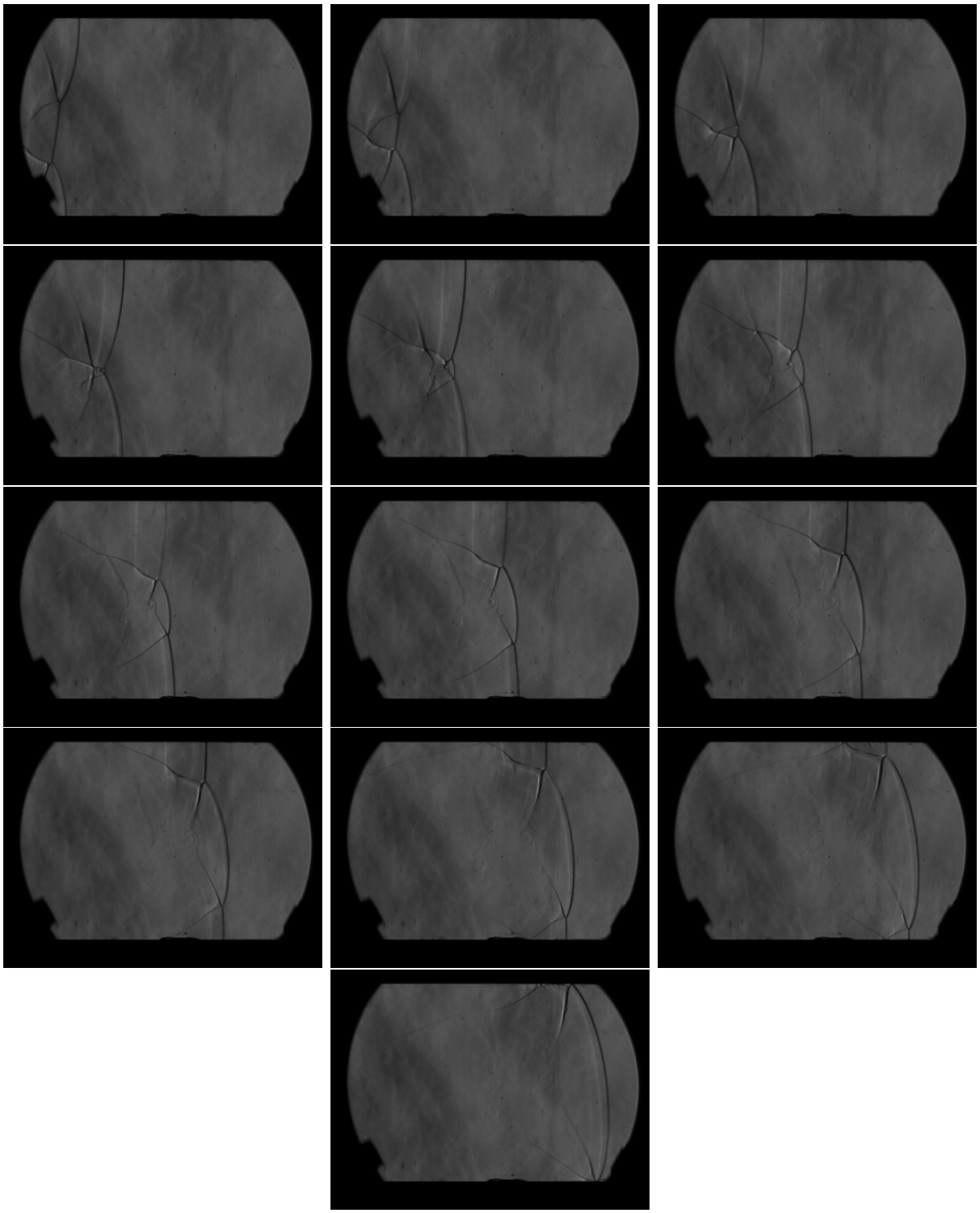

Figure A.5: Summary of experiment 18_H2 performed in $2H_2 + O_2 + 7Ar$.

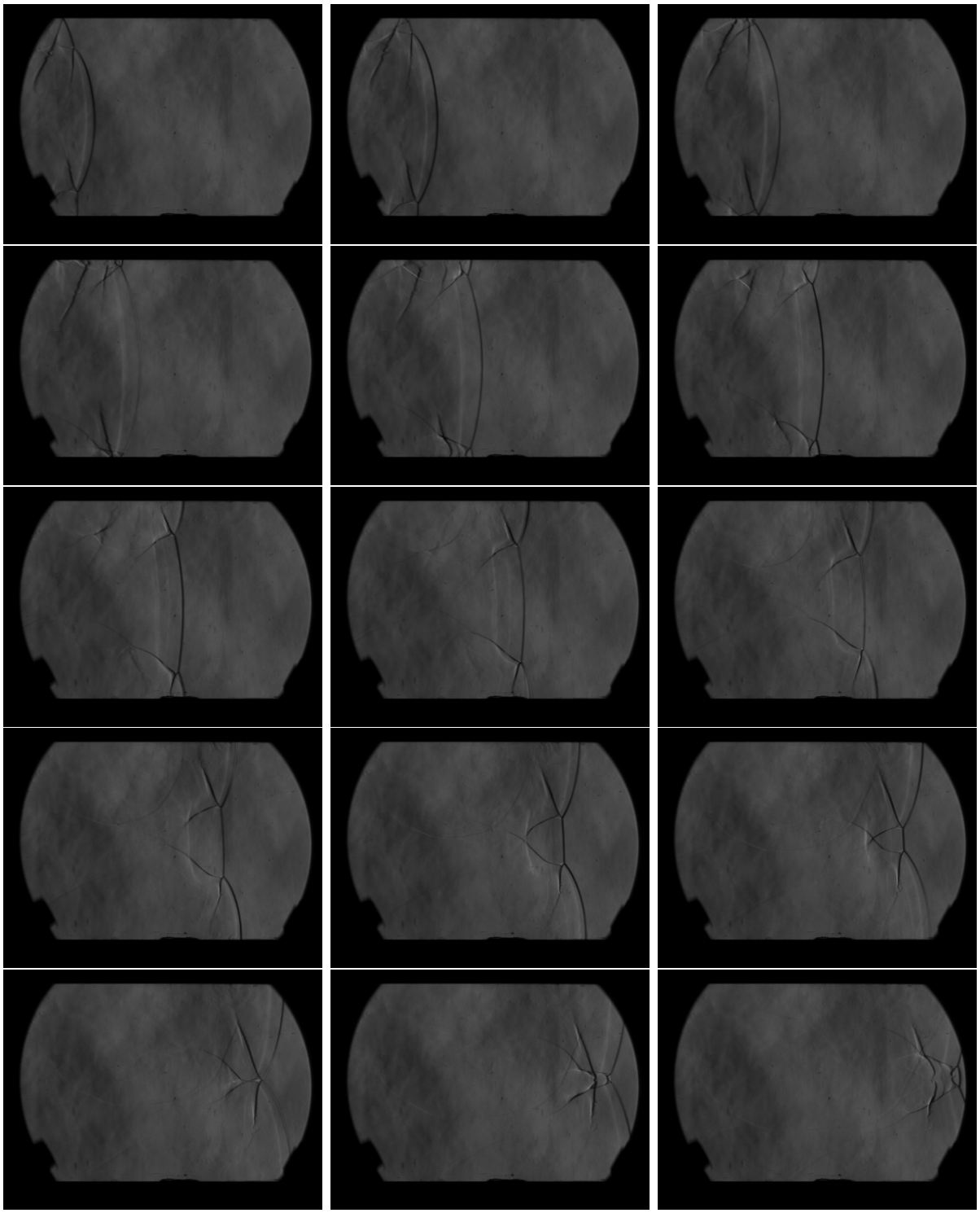

Figure A.6: Summary of experiment 19_H2 performed in $2H_2 + O_2 + 7Ar$.

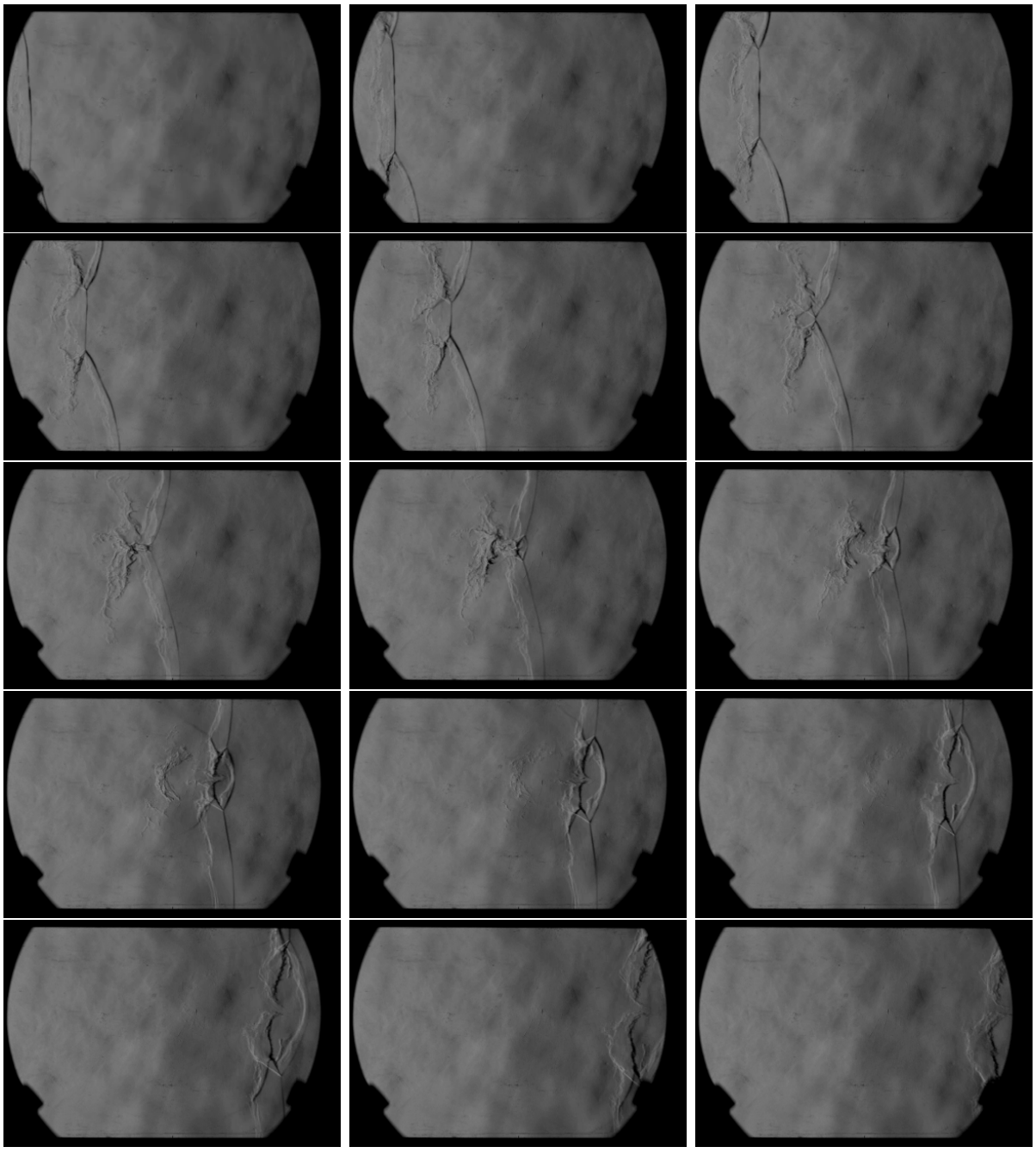

Figure A.7: Summary of experiment performed in $CH_4 + 2O_2$. Taken from Maxwell and co-workers [3]

Appendix B

Results of the Multiple Species Real Gas Calculation

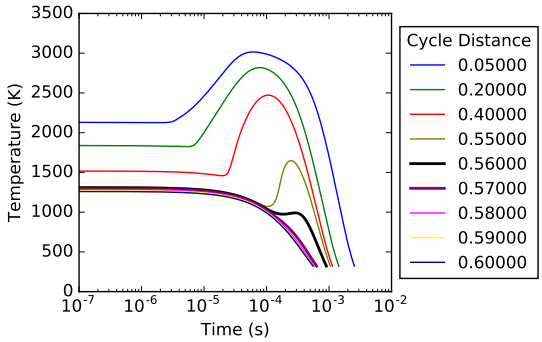

(a) Experiment 0_H2

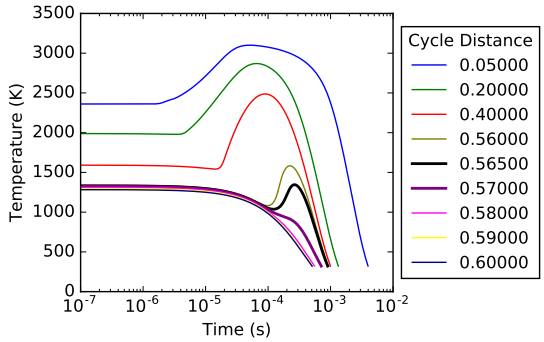

(b) Experiment 5_H2

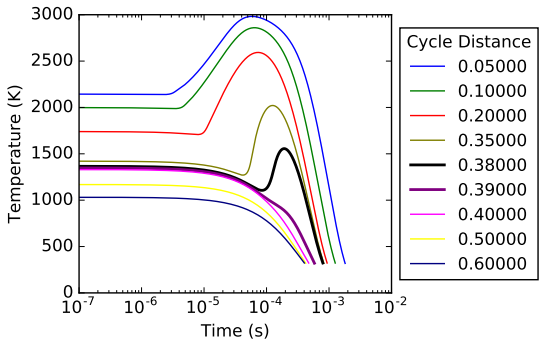

(c) Experiment 11_H2

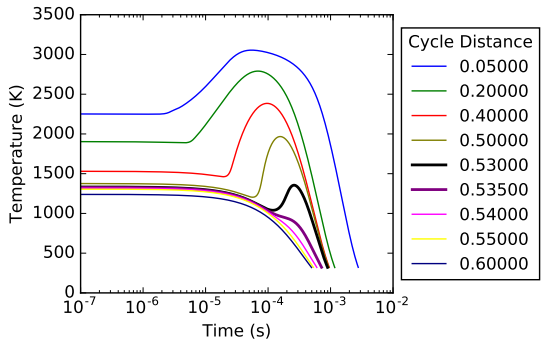

(d) Experiment 13_H2

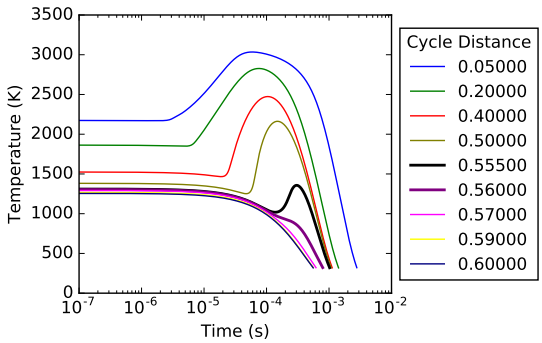

(e) Experiment 18_H2

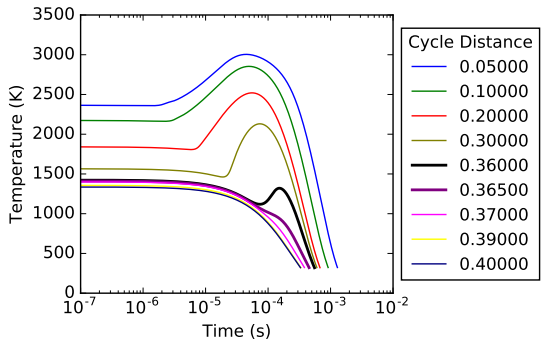

(f) Experiment 19_H2

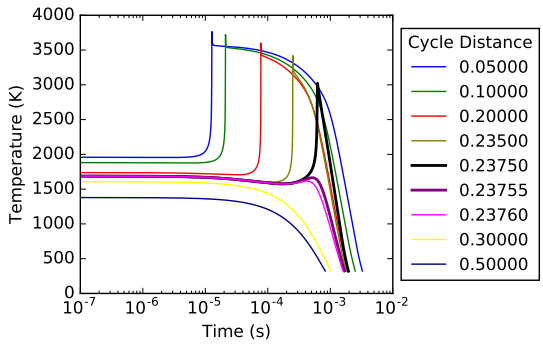

(g) Experiment 0_CH4

Figure B.1: Evolution of the temperature with time, for selected Lagrangian particle paths

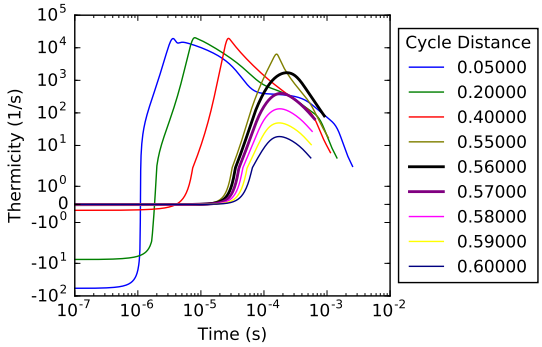

(a) Experiment 0_H2

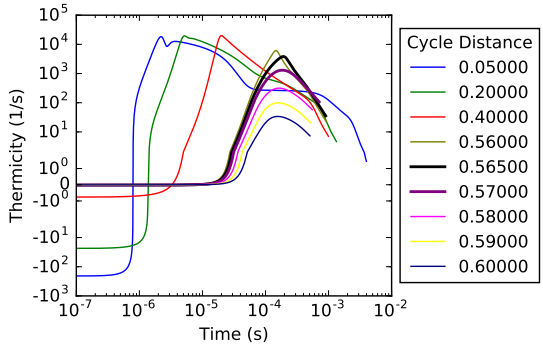

(b) Experiment 5_H2

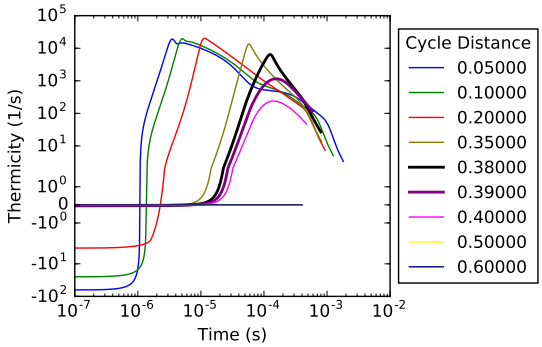

(c) Experiment 11_H2

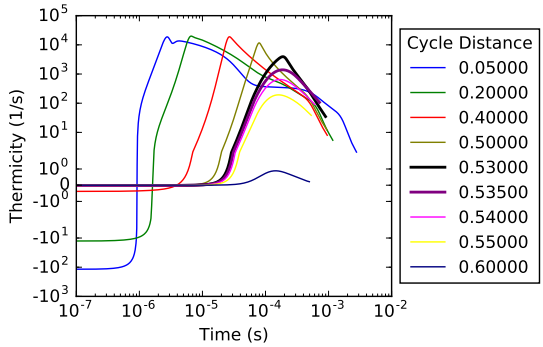

(d) Experiment 13_H2

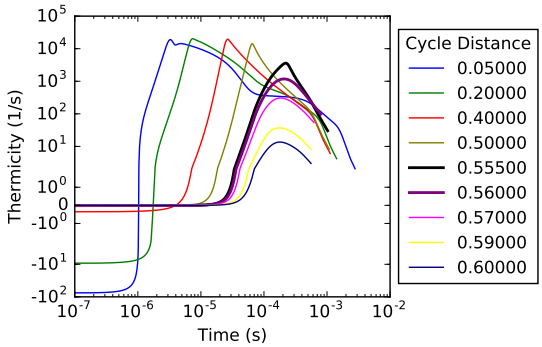

(e) Experiment 18_H2

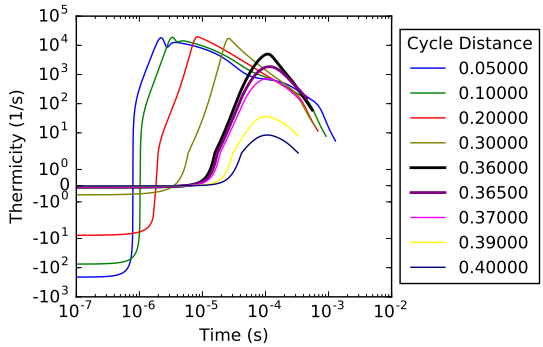

(f) Experiment 19_H2

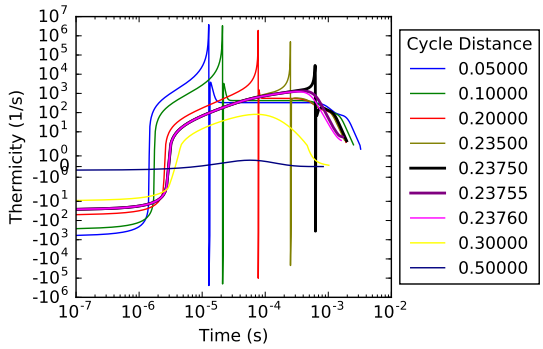

(g) Experiment 0_CH4

Figure B.2: Evolution of the thermicity with time, for selected Lagrangian particle paths

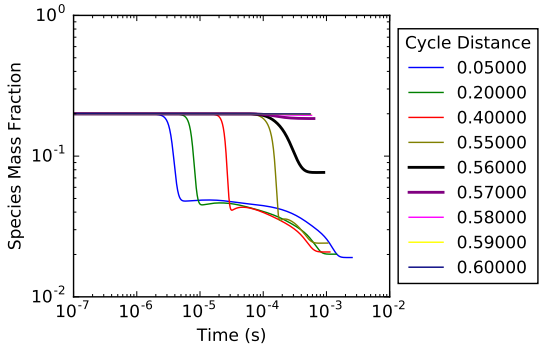

(a) Experiment 0_H2

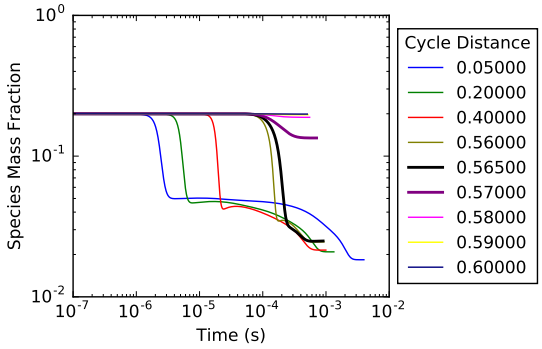

(b) Experiment 5_H2

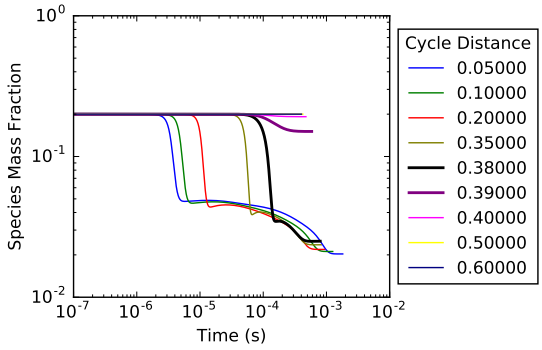

(c) Experiment 11_H2

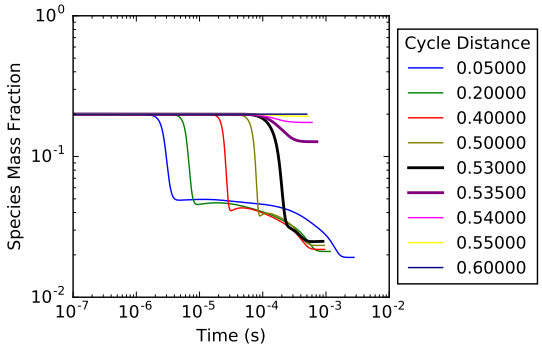

(d) Experiment 13_H2

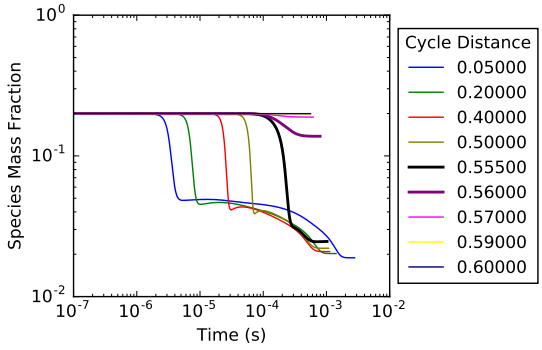

(e) Experiment 18_H2

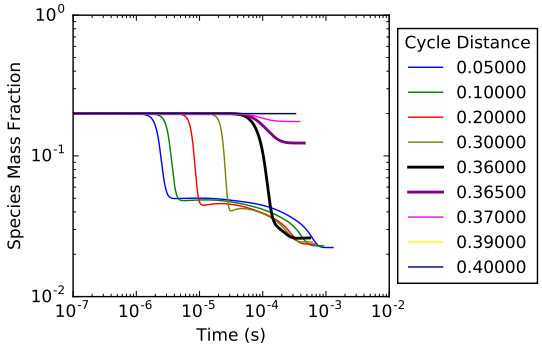

(f) Experiment 19_H2

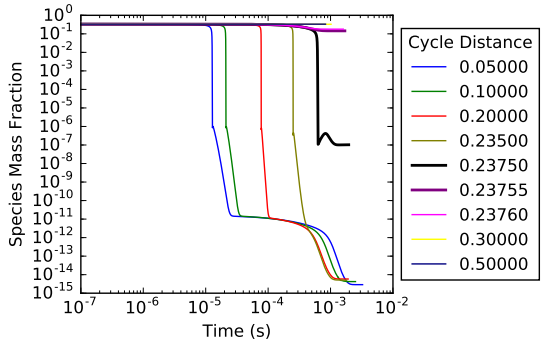

(g) Experiment 0_CH4

Figure B.3: Evolution of the fuel species mass fraction with time, for selected Lagrangian particle

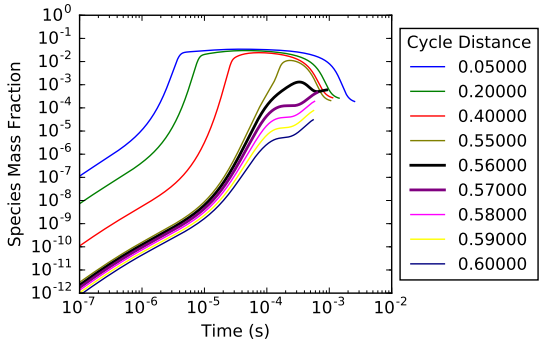

(a) Experiment 0_H2

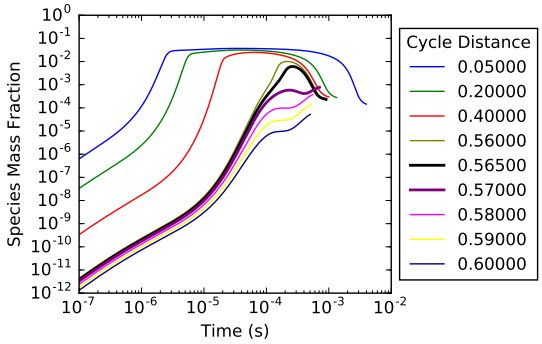

(b) Experiment 5_H2

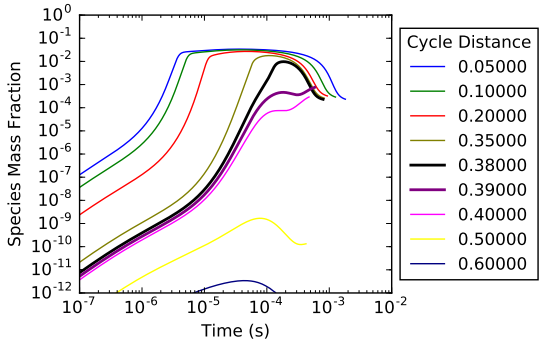

(c) Experiment 11_H2

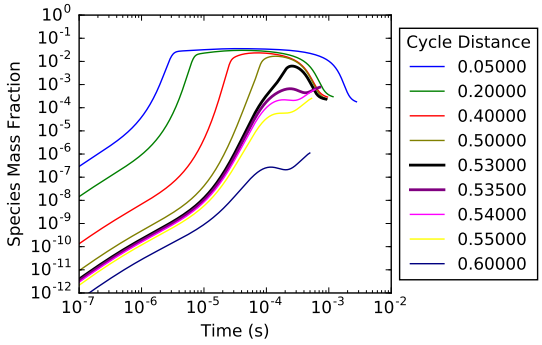

(d) Experiment 13_H2

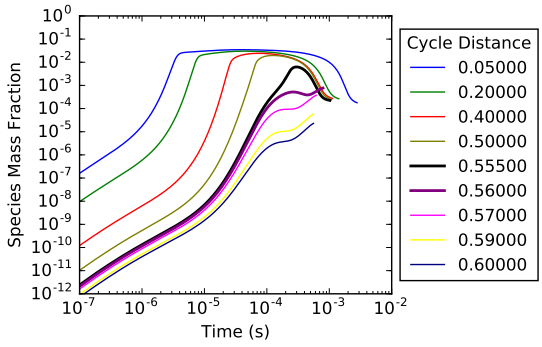

(e) Experiment 18_H2

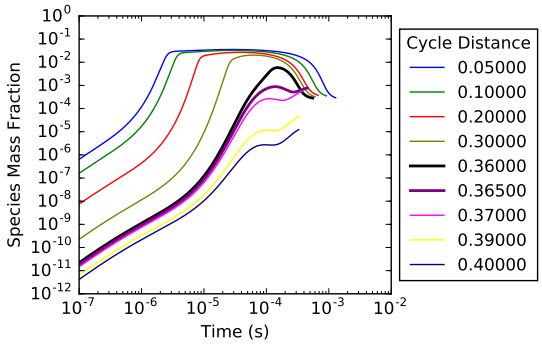

(f) Experiment 19_H2

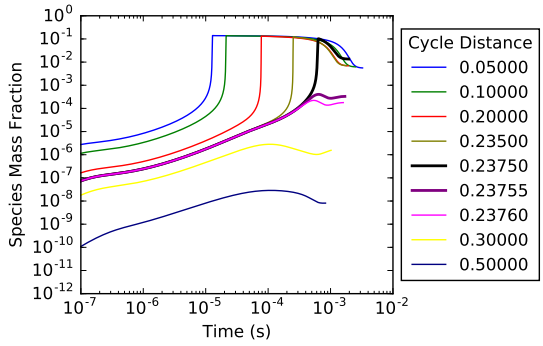

(g) Experiment 0_CH4

Figure B.4: Evolution of the OH mass fraction with time, for selected Lagrangian particles

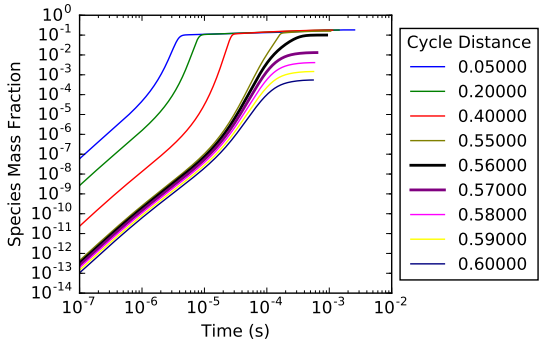

(a) Experiment 0_H2

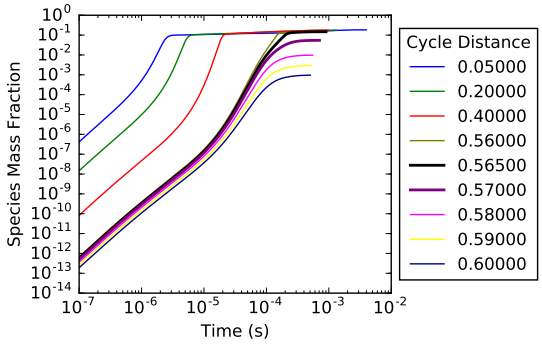

(b) Experiment 5_H2

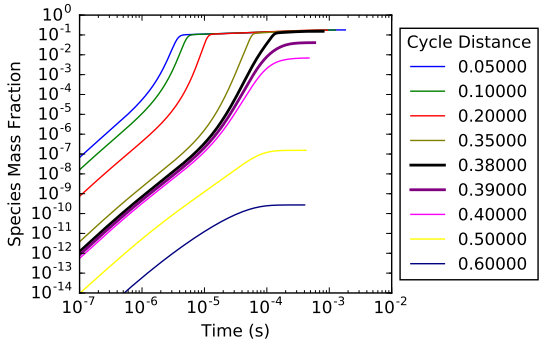

(c) Experiment 11_H2

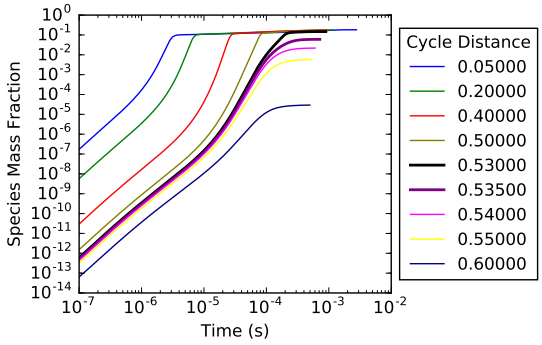

(d) Experiment 13_H2

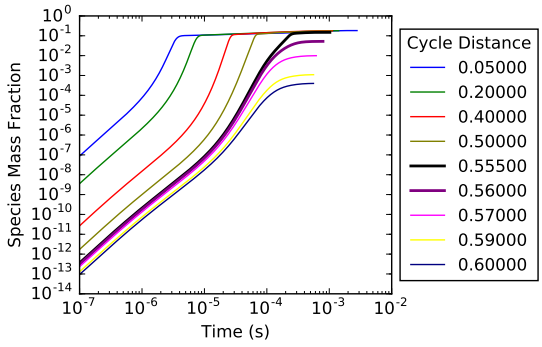

(e) Experiment 18_H2

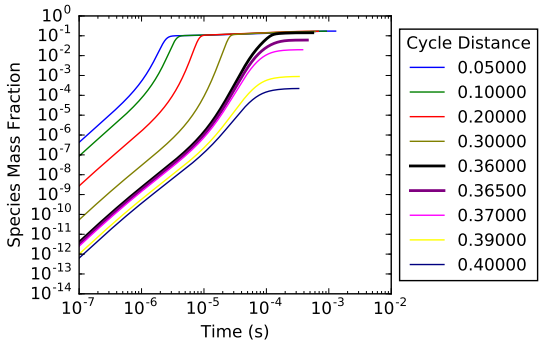

(f) Experiment 19_H2

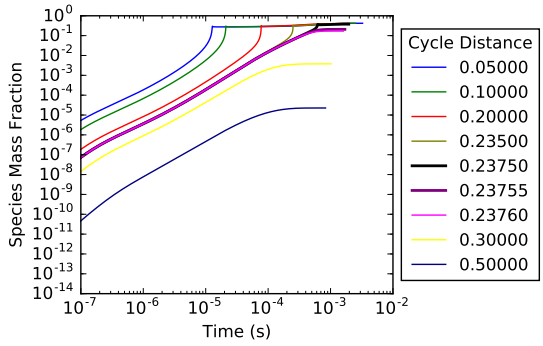

(g) Experiment 0_CH4

Figure B.5: Evolution of the H_2O mass fraction with time, for selected Lagrangian particles

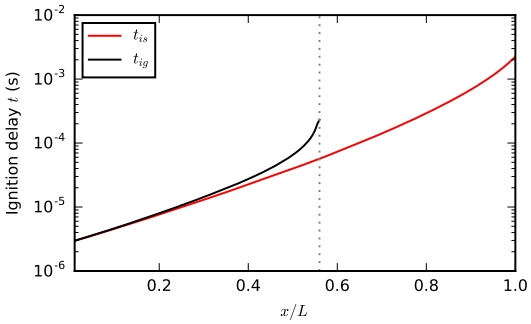

(a) Experiment 0_H2

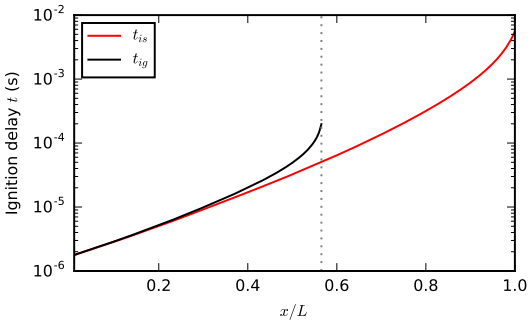

(b) Experiment 5_H2

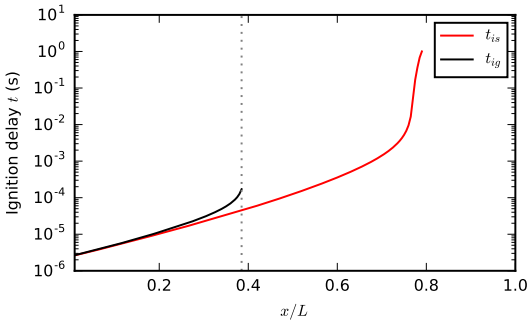

(c) Experiment 11_H2

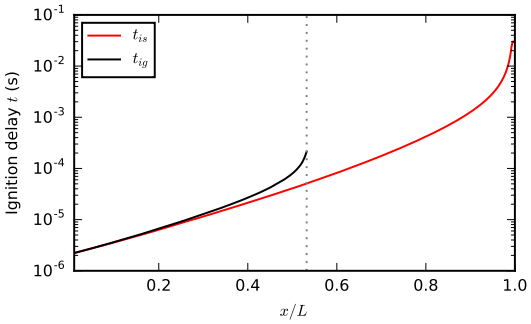

(d) Experiment 13_H2

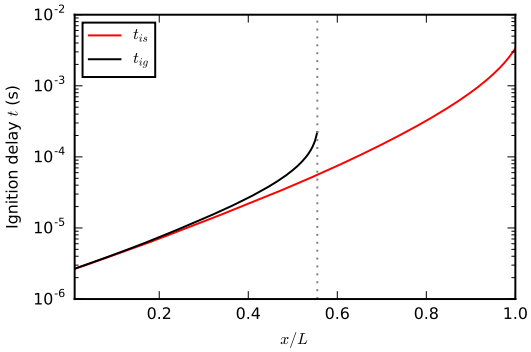

(e) Experiment 18_H2

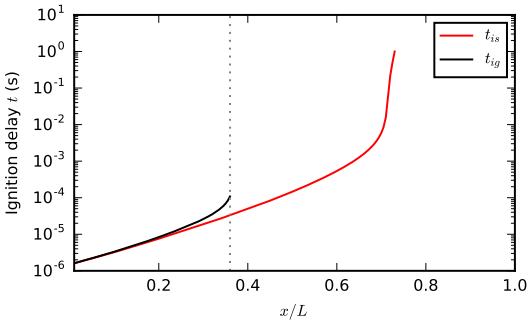

(f) Experiment 19_H2

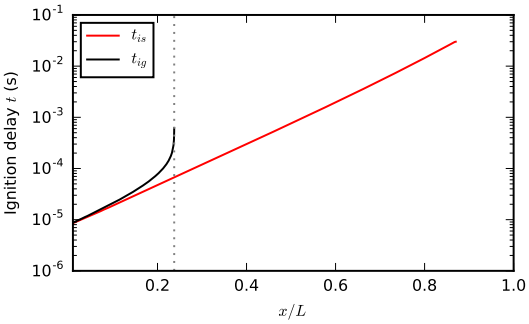

(g) Experiment 0_CH4

Figure B.6: Evolution of the ignition delay with expansion (black) and in the absence of expanison (black), across the length of a detonation cell. The dotted line represents the critical ignition limit.

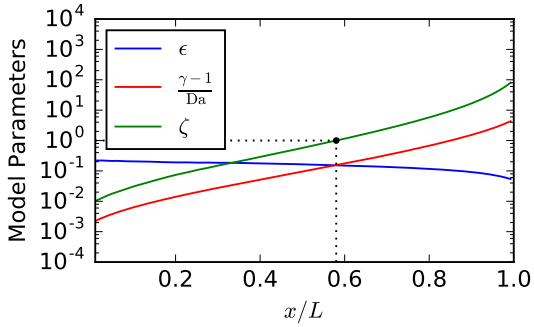

(a) Experiment 0_H2

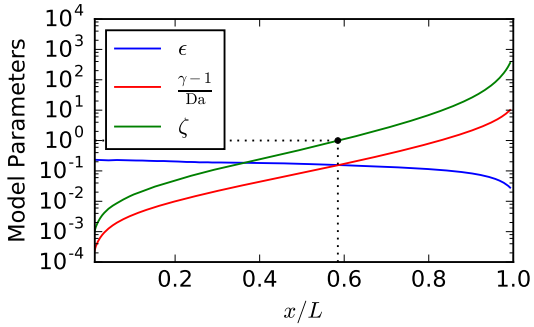

(b) Experiment 5_H2

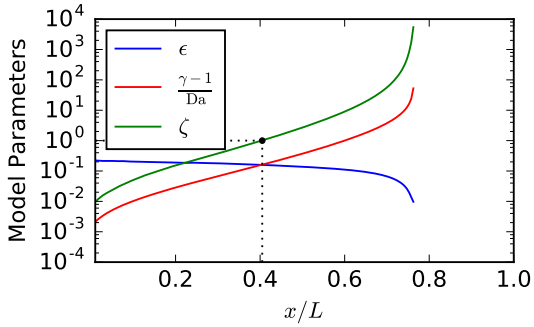

(c) Experiment 11_H2

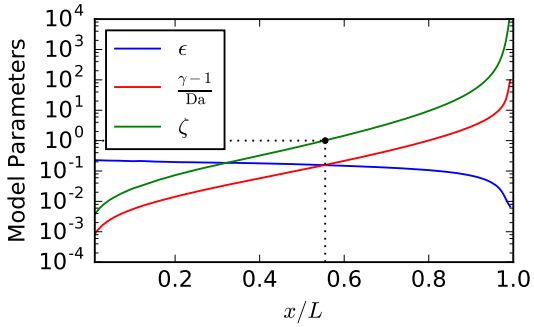

(d) Experiment 13_H2

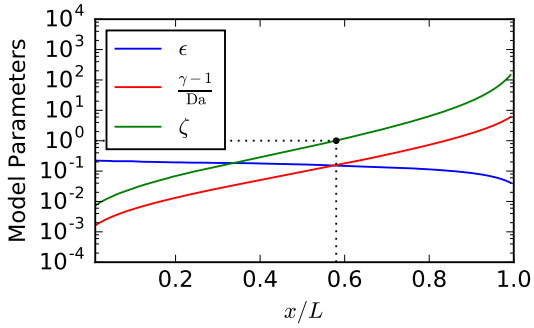

(e) Experiment 18_H2

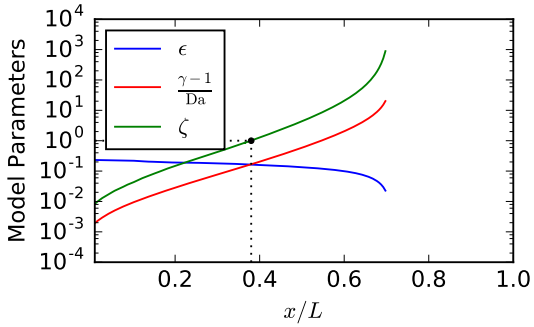

(f) Experiment 19_H2

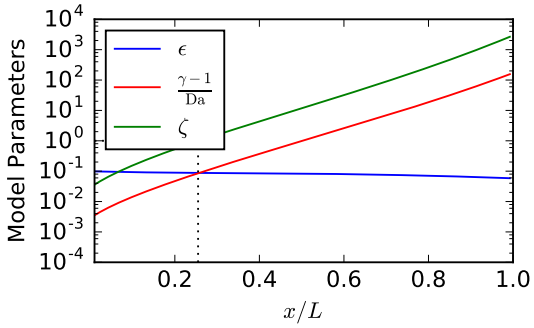

(g) Experiment 0_CH4

Figure B.7: Evolution of the model parameters with time, for selected Lagrangian particles. The dotted lines show the critical ignition criterion predicted by $\zeta = 1$.

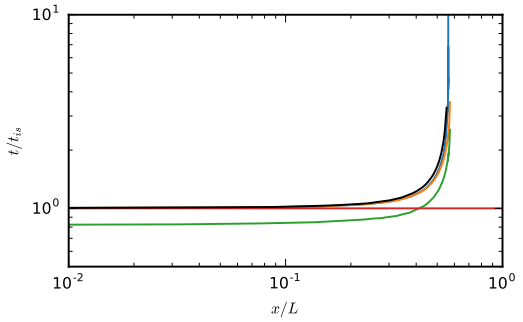

(a) Experiment 0_H2

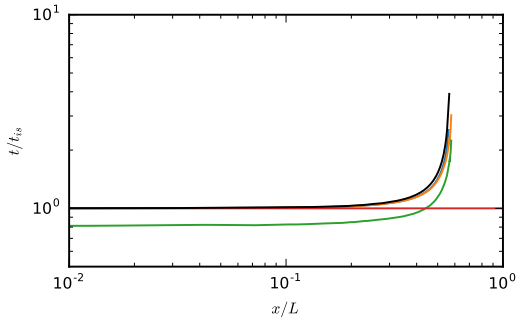

(b) Experiment 5_H2

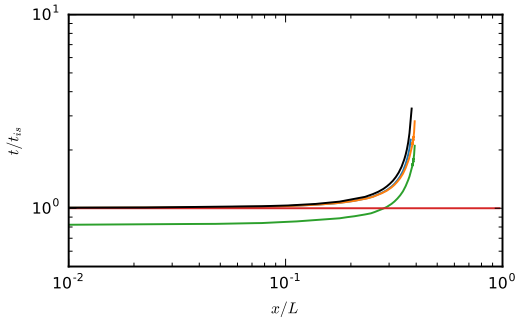

(c) Experiment 11_H2

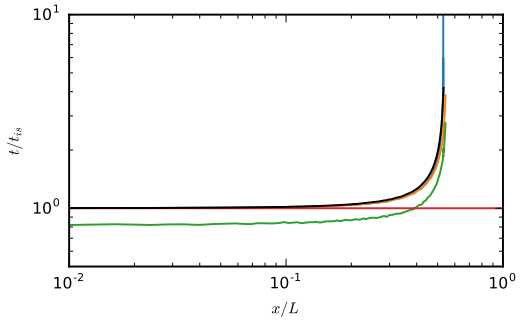

(d) Experiment 13_H2

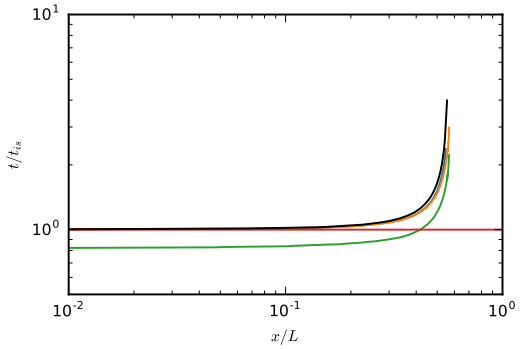

(e) Experiment 18_H2

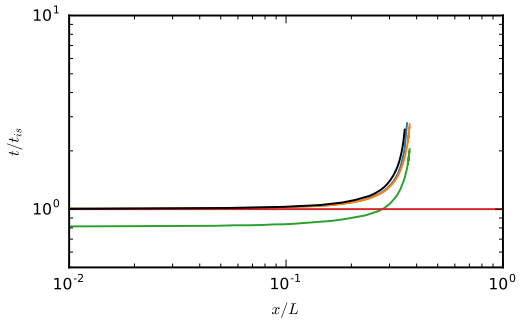

(f) Experiment 19_H2

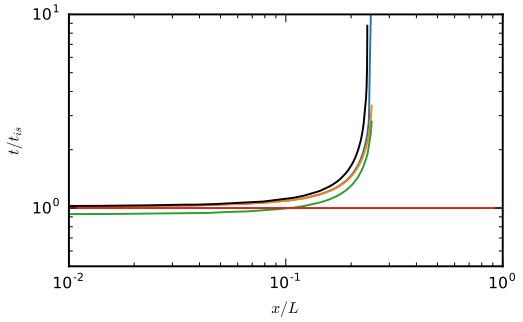

(g) Experiment 0_CH4

Figure B.8: Predicted Ignition delay evolution over a detonation cell. Black: t_{ig} from detailed chemistry. Red: t_{is} from detailed chemistry. Blue: Implicit 2-step (2.45). Green: Approximate 2-step (2.48). Orange: Solution in the limit of $\zeta = \mathcal{O}(1)$ (2.30) & (2.54).

Appendix C

Experimental Noise Measurements

C.1 System Noise Measurements

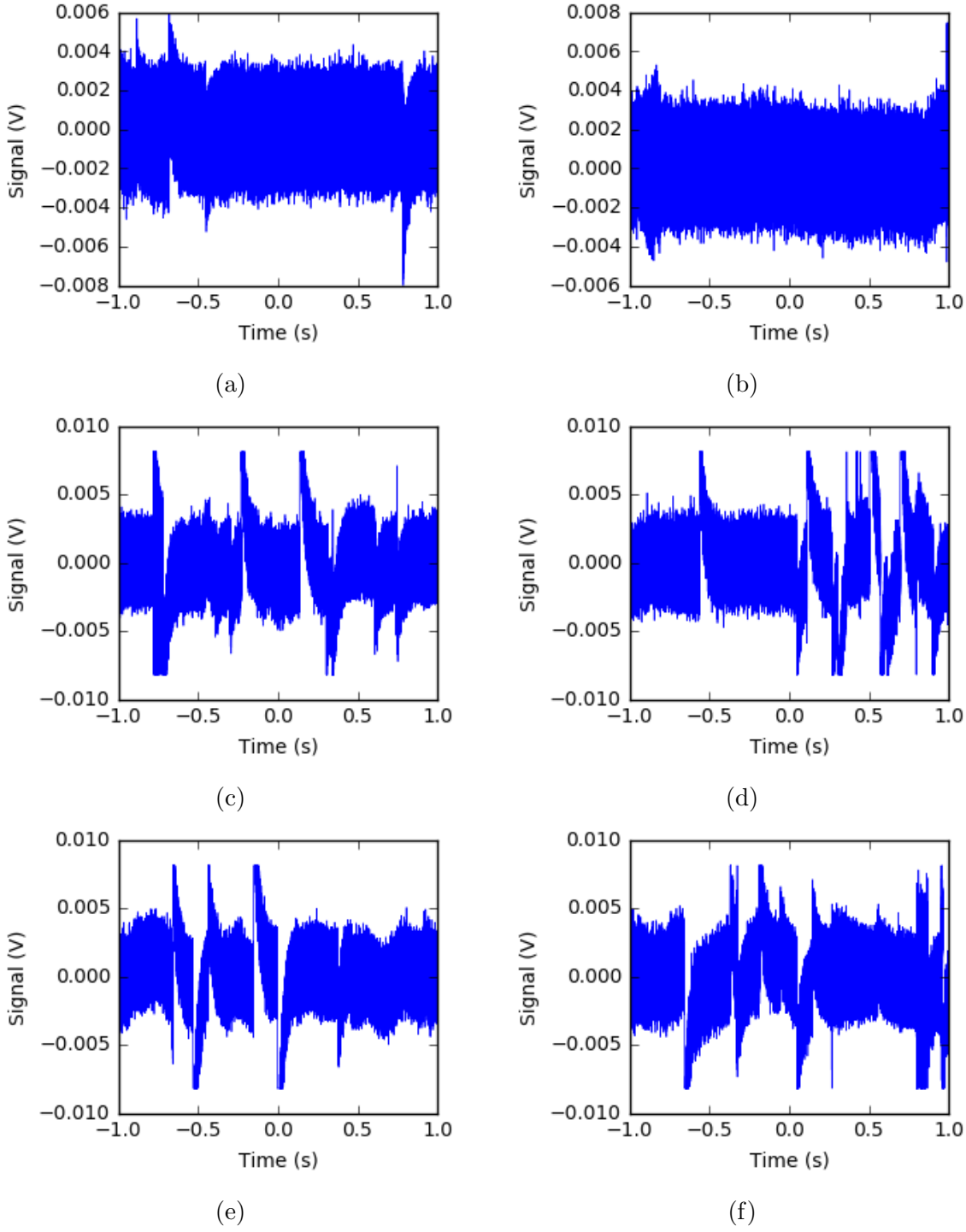

Figure C.1: Time-trace of signals measured to perform the experimental noise measurements of the overall system. Note the fairly frequent mode-hops present in this signal, which can be substracted by using a reference detector.

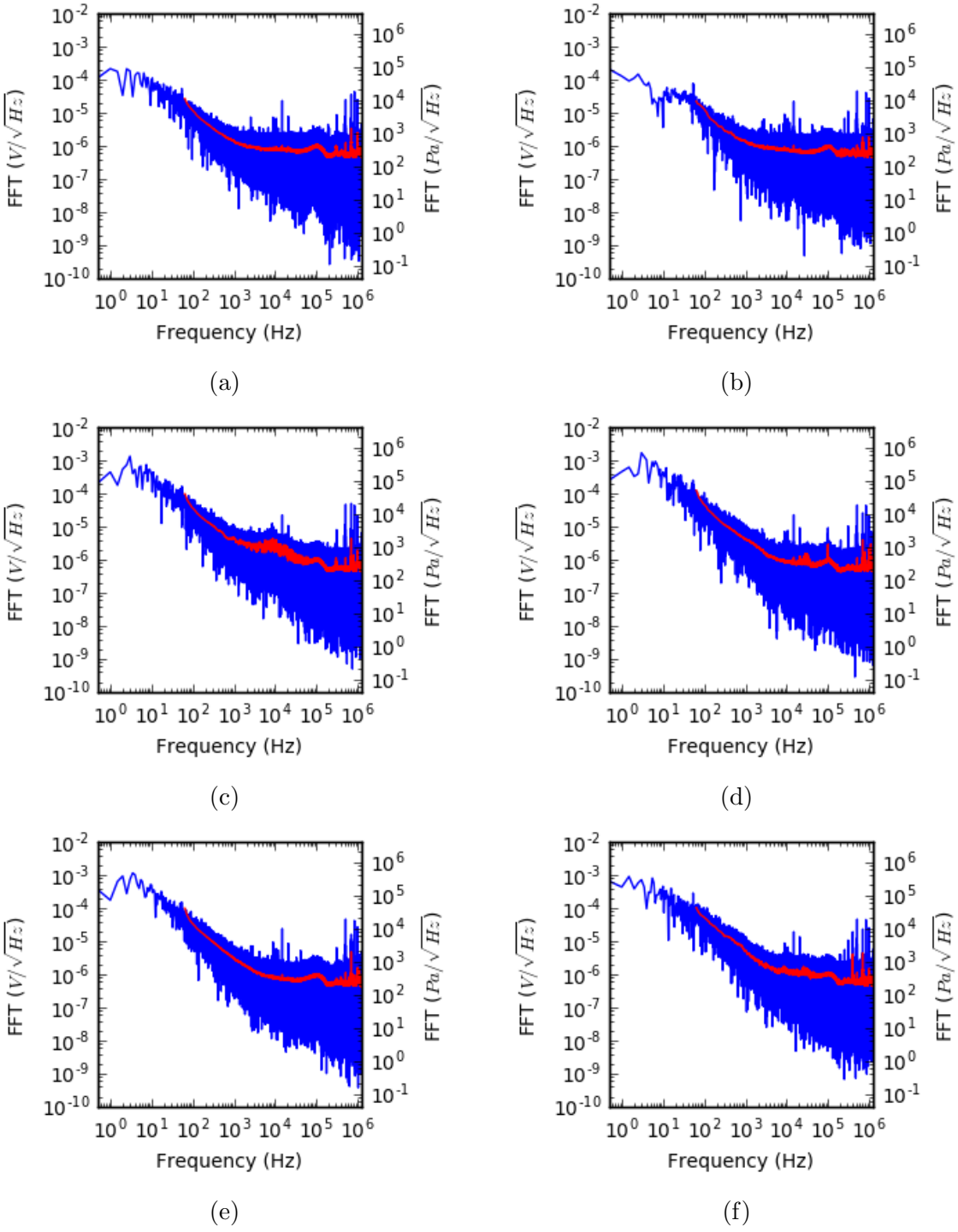

Figure C.2: Logarithm of the voltage and pressure spectrum of the overall system plotted against the logarithm of the frequency, for each of the signals ploted in Figure C.1. The red curve is a 256-bin moving average of the FFT signal.

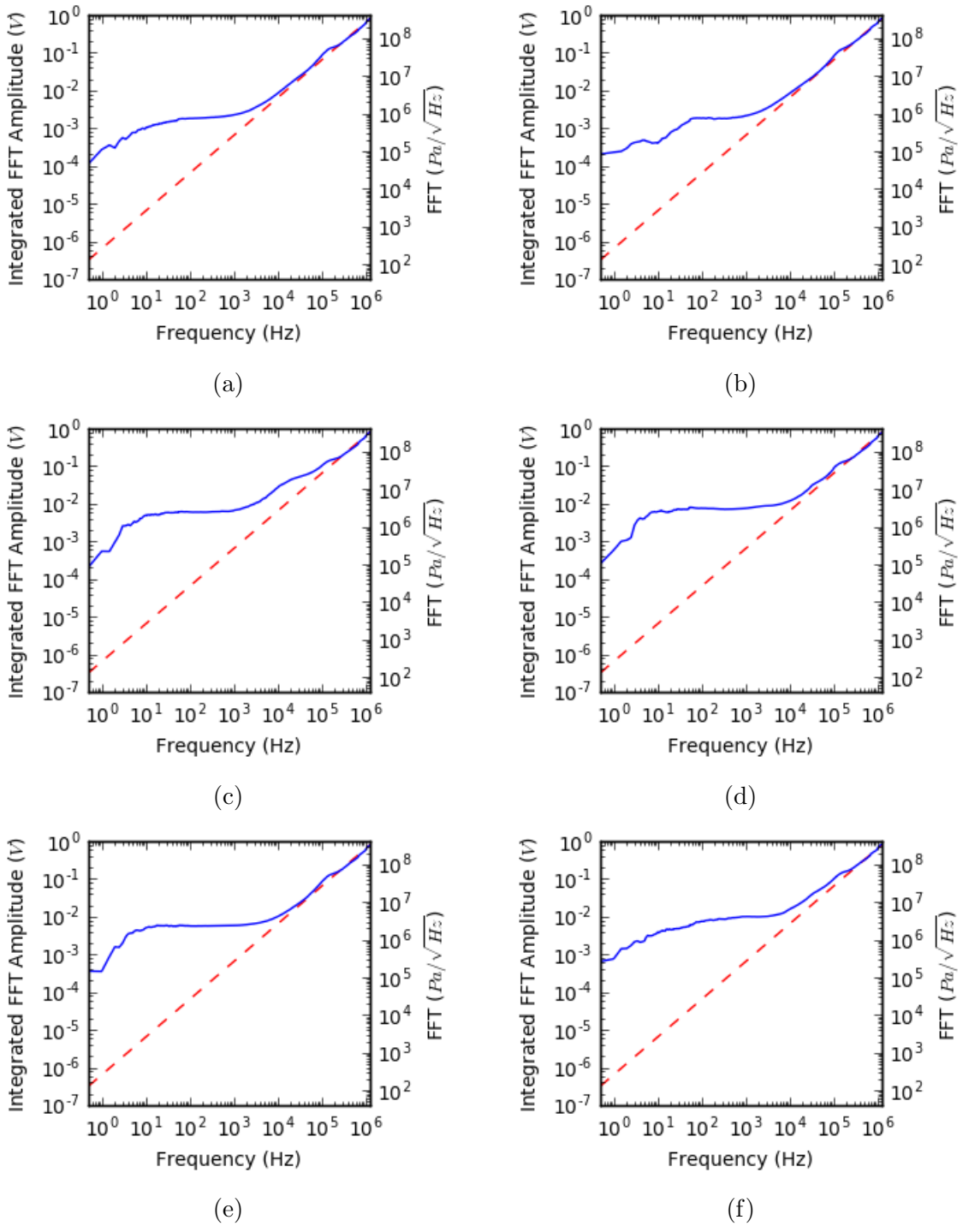

Figure C.3: System noise floor integrated over the measurement bandwidth (blue), plottedalongside the white noise limit integrated over the measurement bandwidth (red). A cutoff frequency exists around 100 kHz above which the low-frequency 1/f noise ceases to be the dominating noise source. In this higher frequency region, the white noise is an accurate approximation of the system noise.

C.2 Oscilloscope Noise Measurements

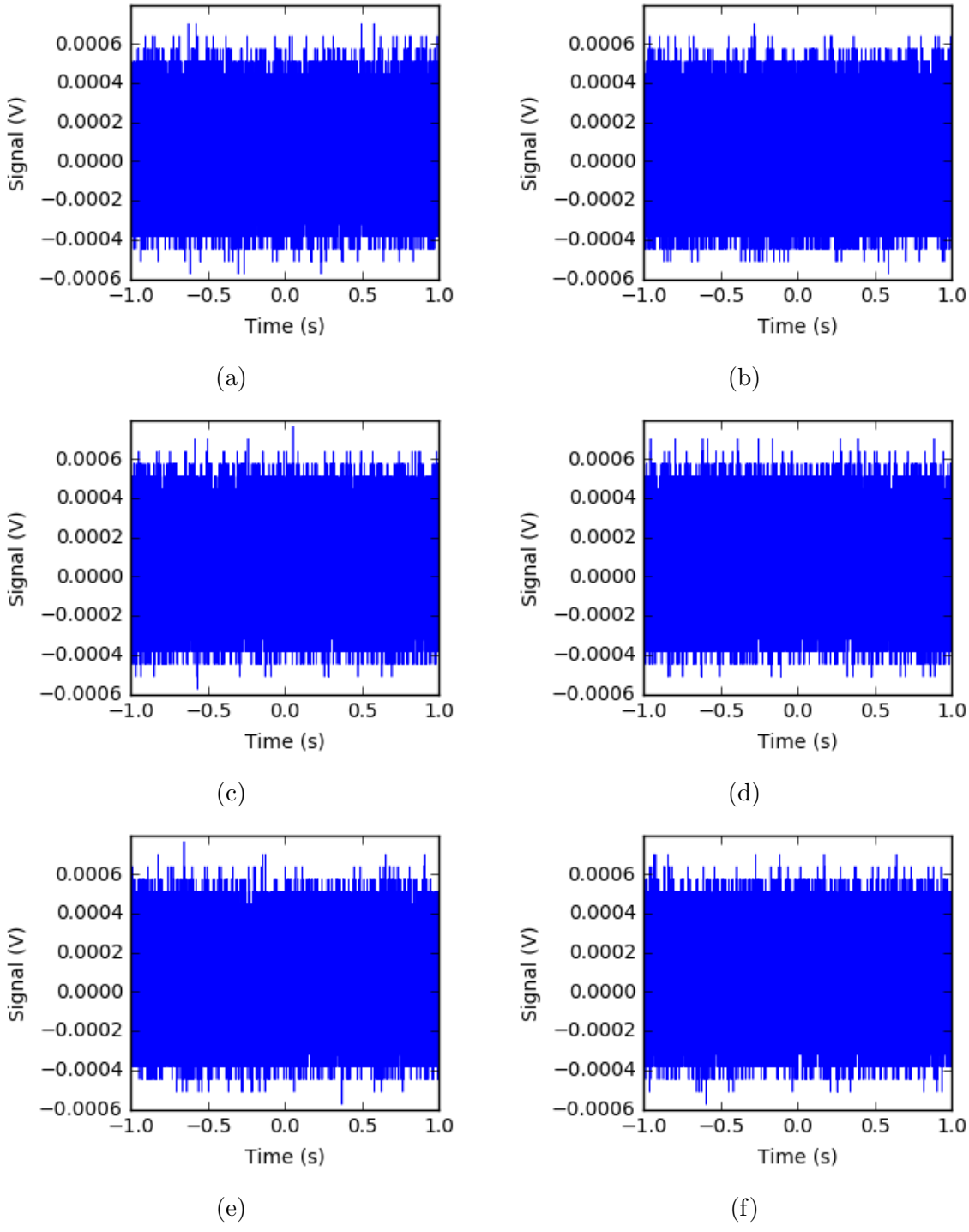

Figure C.4: Time-trace of signals measured to perform the experimental noise measurements of the oscilloscopes.

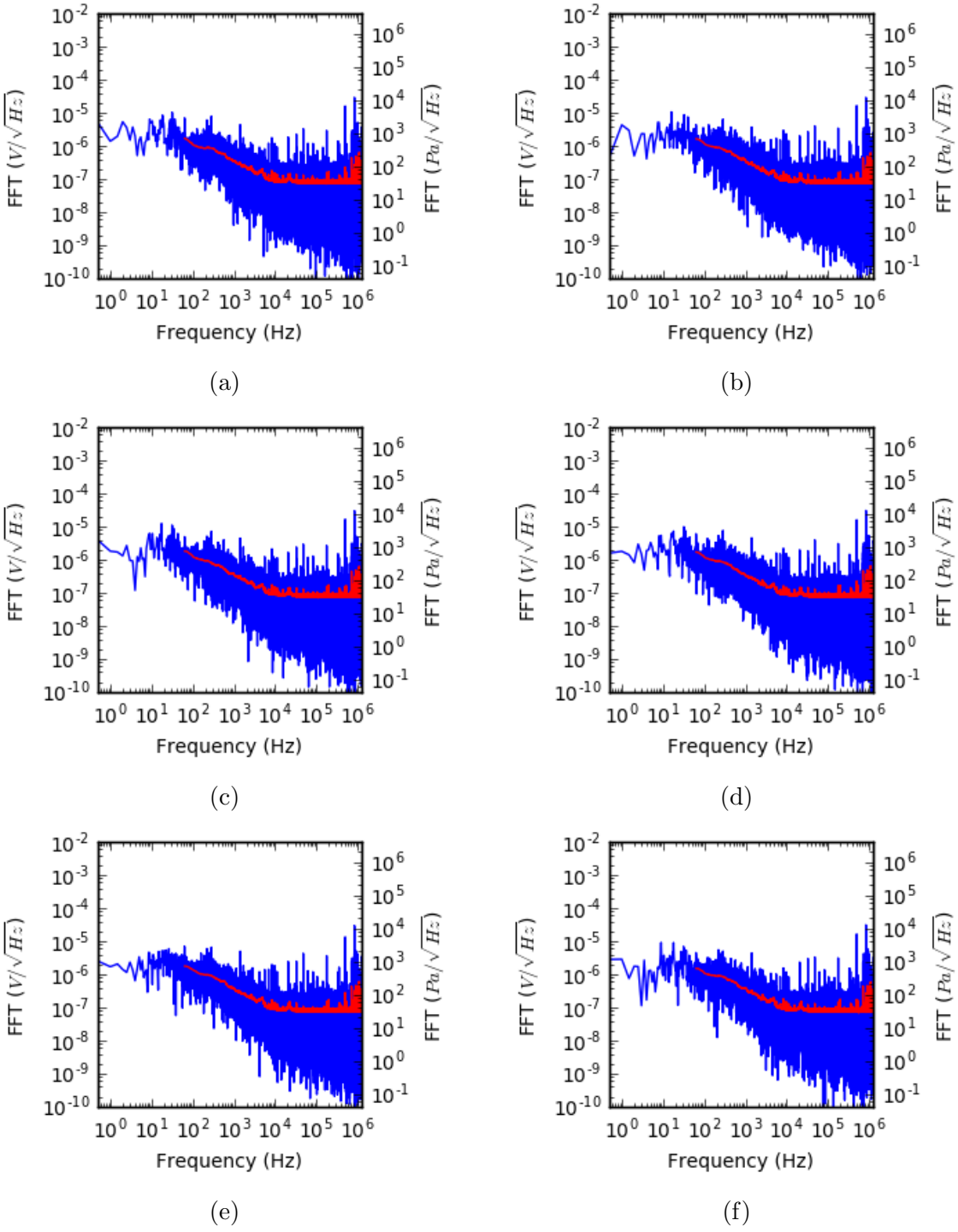

Figure C.5: Logarithm of the power spectrum of the overall system plotted against the logarithm of the frequency, for each of the signals ploted in Figure C.1. The red curve is a 256-bin moving average of the FFT signal.

Appendix D

Shock Tube Experiment List

Table D.1: Details of the performed Shock Tube Experiments

Exp. Name	Test Gas	Test Gas Pressure (psi)	Driver Gas	Driver Gas Pressure (psi)	Detonation	Triple Points
0_H2 [1]	$2H_2 + O_2 + 7Ar$	0.6	$C_2H_4 + 3O_2$	1.5	Yes	2
1_H2	$2H_2 + O_2 + 7Ar$	0.6	$C_2H_4 + 3O_2$	1.54	Yes	5
2_H2	$2H_2 + O_2 + 7Ar$	0.6	$C_2H_4 + 3O_2$	1.5	Yes	3
3_H2	$2H_2 + O_2 + 7Ar$	0.6	$C_2H_4 + 3O_2$	1.51	Yes	4
4_H2	$2H_2 + O_2 + 7Ar$	0.6	$C_2H_4 + 3O_2$	1.51	Yes	3
5_H2	$2H_2 + O_2 + 7Ar$	0.6	$C_2H_4 + 3O_2$	1.5	Yes	2
6_H2	$2H_2 + O_2 + 7Ar$	0.6	$C_2H_4 + 3O_2$	1.49	Yes	3
7_H2	$2H_2 + O_2 + 7Ar$	0.6	$C_2H_4 + 3O_2$	1.5	Yes	4
8_H2	$2H_2 + O_2 + 7Ar$	0.6	$C_2H_4 + 3O_2$	1.48	Yes	5
9_H2	$2H_2 + O_2 + 7Ar$	0.6	$C_2H_4 + 3O_2$	1.5	Yes	3
10_H2	$2H_2 + O_2 + 7Ar$	0.6	$C_2H_4 + 3O_2$	1.5	Yes	3
11_H2	$2H_2 + O_2 + 7Ar$	0.59	$C_2H_4 + 3O_2$	1.5	Yes	2
12_H2	$2H_2 + O_2 + 7Ar$	0.59	$C_2H_4 + 3O_2$	1.5	Yes	3
13_H2	$2H_2 + O_2 + 7Ar$	0.59	$C_2H_4 + 3O_2$	1.5	Yes	2
14_H2	$2H_2 + O_2 + 7Ar$	0.59	$C_2H_4 + 3O_2$	1.5	Yes	3
15_H2	$2H_2 + O_2 + 7Ar$	0.59	$C_2H_4 + 3O_2$	1.5	No	-
16_H2	$2H_2 + O_2 + 7Ar$	0.59	$C_2H_4 + 3O_2$	1.5	Yes	3
17_H2	$2H_2 + O_2 + 7Ar$	0.59	$C_2H_4 + 3O_2$	1.51	Yes	4
18_H2	$2H_2 + O_2 + 7Ar$	0.59	$C_2H_4 + 3O_2$	1.5	Yes	2
19_H2	$2H_2 + O_2 + 7Ar$	0.59	$C_2H_4 + 3O_2$	1.5	Yes	2
0_CH4 [3]	$CH_4 + 2O_2$	0.6	$C_2H_4 + 3O_2$	1.5	Yes	2

Appendix E

Equipment Specification Sheets

E.1 Laser Diode

785 nm Fabry-Perot Laser Diode, 250mW

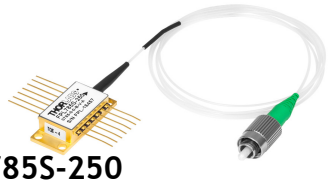

Description

FPL785S-250

The FPL785S-250 785 nm Fabry-Perot Laser Diode is based on quantum well epitaxial layer growth and a highly reliable ridge waveguide structure. This diode features high optical output power and slope efficiency.

The laser diode is housed in butterfly package with an integrated monitor photodiode, TEC, and a thermistor that allows the laser to be temperature controlled. The output is coupled to 1.0 m of FC/APC-connectorized 780HP single-mode fiber.

Specifications

Absolute Maximum Ratings	
LD Reverse Voltage (Max)	2 V
PD Reverse Voltage (Max)	20 V
Absolute Max Current	550 mA[a]
Absolute Max Power	300 mW
Operating Case Temperature	0 to 70 °C
Storage Temperature	-10 to 70°C
Pin Code	14 pin, Type 1

Characteristics (CW; T_{CHIP} = 25 °C, T_{CASE} = 0 - 70 °C)				
	Symbol	Min	Typical	Max
Center Wavelength	λ_C	775 nm	785 nm	795 nm
Spectral Bandwidth (RMS)	$\Delta\lambda$	-	0.5 nm	2 nm
Output Power CW @ I_{CW}	P_{CW}	250 mW	-	300 mW
Operating Current CW	I_{CW}	-	500 mA	550 mA[a]
Threshold Current	I_{TH}	-	110 mA	150 mA
Forward Voltage	V_F	-	2.0 V	2.8 V
Slope Efficiency	$\Delta P/\Delta I$		0.7 mW/mA	-
TEC Operation (Typical/Max @T_{CASE} = 25°C/70°C)				
-TEC Current	I_{TEC}	-	0.35 A	2.5 A
-TEC Voltage	V_{TEC}	-	0.35 V	3.2 V
-Thermistor Resistance	R_{TH}	-	10 kΩ	-

a. *Some devices will produce an output power higher than the 300 mW max when driven with a 550 mA current. Do not drive the laser diode with a current that will cause the output power to exceed the specified maximum power rating. Operating in this regime can cause damage to the device.*

Typical Performance Plots

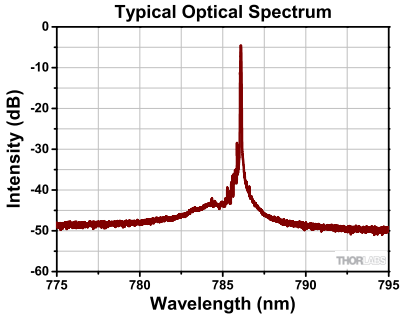

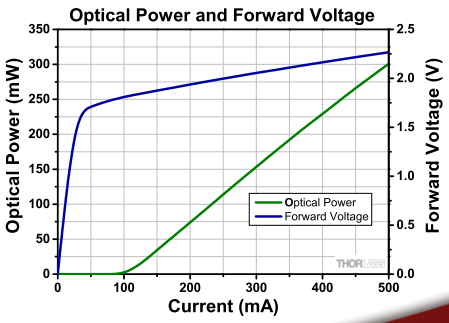

Product Data Sheet

Laser Diode

THORLABS

FPL785S-250

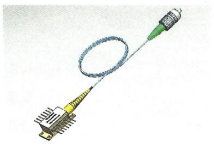

S/N: FPL-27082
Center Wavelength: 788.1 nm
Fiber Type: 780HP
Test Date: 4/12/2017

Diode Package:
Connector: NA
Tested By: Paya

QA: Pass

Summary of Test Data (CW, T_{chip}=25°C)

Parameter	*Symbol*	*Value*	*Unit*
Fiber Output Power	P_{op}	250.0	mW
Operating Current@P_{op}	I_{op}	469.5	mA
Operating Voltage@P_{op}	V_{op}	2.13	V
Monitor Current[4] @P_{op}	I_{mon}	1.398	mA
Threshold Current	I_{th}	87.5	mA
Slope Efficiency	ΔP/ΔI	0.65	W/A

Absolute Maximum Ratings

Parameter	*Ratings*	*Unit*
Laser Diode Current*	550	mA
Optical Output Power*	300	mW
LD Reverse Voltage*	2	V
Storage Temperature	-10 ~ 70	°C
Case Temperature	0 ~ 70	°C

* CW, T_{chip}=25°C

LASER RADIATION
AVOID EXPOSURE TO BEAM
CLASS 3B LASER PRODUCT

CAUTION- use of controls or adjustments or performance of procedures other than those specified herein may result in hazardous radiation exposure. There are no user serviceable parts in this product. When proper power is applied to this product, laser radiation will be emitted from distal fiber end.

FPL-27082
LIV

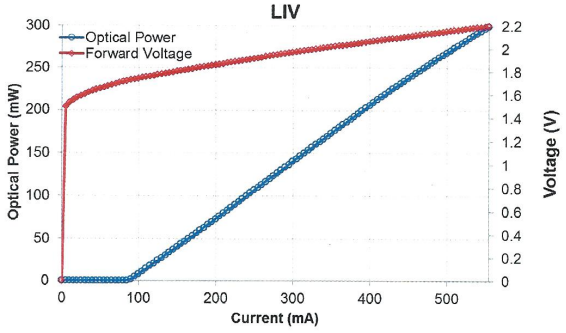

Pin Diagram

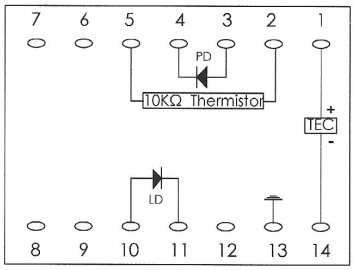

PIN	Desc
1	TEC (+)
2	Thermistor
3	PD Anode
4	PD Cathode
5	Thermistor
10	LD Anode
11	LD Cathode
13	GND
14	TEC(-)

Select Type 1 Pin Configuration when use Thorlabs Butterfly Diode Mount

Important Notes:
1. The maximum ratings mean the limitation over which the laser should not be operated even momentarily.
2. To protect the laser diode from damage due to static electricity (ESD), please follow proper ESD handling precautions.
3. To ensure safe operation use only with a suitable power source that complies with the pertinent requirements for laser systems as specified in IEC-60825-1 "Safety of Laser Products."
4. The monitor PD is intended to be used as a soft indicator of relative power. Its current value may change if the coiled fiber is repositioned. For monitoring absolute power, an external fiber tap coupler with separate monitor PD is recommended.
5. Refer to the Spec Sheet for complete specifications and additional operation notes.

USA, Canada, and South America
Thorlabs, Inc.
56 Sparta Avenue
Newton, NJ 07860, USA
Tel: 973-579-7227
Fax: 973-300-3600

Europe
Thorlabs GmbH
85221 Dachau, Germany
Tel: +49-(0)8131-5956-0

Scandinavia
Thorlabs Sweden AB
400 20 Göteborg, Sweden
Tel: +46-31-733-30-00

UK and Ireland
Thorlabs LTD.
Cambridgeshire CB7 4EX, GB
Tel: +44 (0)1353-654440

Japan and Asia
Thorlabs Japan Inc.
Toshima-ku, Tokyo 170-0013, Japan
Tel: +81-3-5979-8889

France
Thorlabs SAS
78600 Maisons-Laffitte, France
Tel: +33 (0) 970 444 844

China
Thorlabs China
Shanghai, China
Tel: +86 (0)21-32513486

E.2 2x2 Fibre Coupler

Narrowband Fiber Optic Coupler
785 nm, 50:50 Ratio

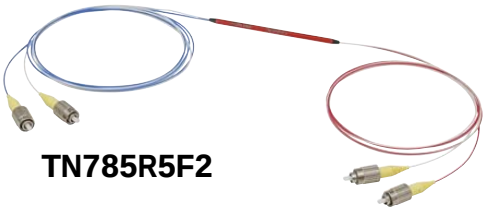

TN785R5F2

Description

Thorlabs' TN785R5F2 single mode narrowband fiber coupler is designed for a center wavelength of 785 nm with ≤0.3 dB of excess loss within the specified bandwidth.

Specifications

TN785R5F2	
Coupling Ratio[a]	50:50
Coupling Ratio Tolerance	±5.0%
Center Wavelength	785 nm
Bandwidth[a]	±15 nm
Excess Loss[a]	≤0.3 dB
Insertion Loss[a]	≤3.8 dB / ≤3.8 dB
Polarization-Dependent Loss (PDL)[a]	≤0.2 dB
Optical Return Loss (ORL) / Directivity[a]	≥60 dB
Max Power Level[b]	500 mW (With Connectors or Bare Fiber) 2 W (Spliced)
Fiber Type[c]	780HP
Port Configuration	2x2
Fiber Lead Length and Tolerance	0.8 m +0.075 m/-0.0 m
Connectors	2.0 mm Narrow Key FC/PC
Package Size	Ø0.12" x 2.76" (Ø3.2 mm x 70.0 mm)
Jacket	Ø900 µm Hytrel® Loose Tube
Pigtail Tensile Load	10 N
Operating Temperature Range	-40 to 85 °C
Storage Temperature Range	-40 to 85 °C

a. All values are specified at room temperature over the bandwidth without connectors and measured through the white input port as indicated below; similar performance (≤0.05 dB difference) is achieved when the blue port is used as the input.
b. Specifies the total maximum power allowed through the component. Coupler performance and reliability under high-power conditions must be determined within the user's setup. See Usage Tips for safety and handling information.
c. Other fiber types may be available upon request. Please contact techsupport@thorlabs.com with inquiries.

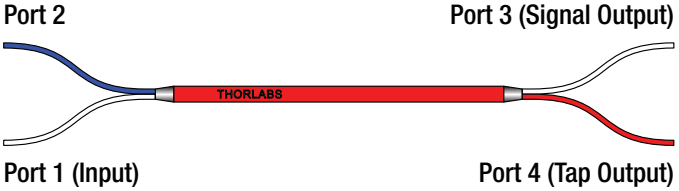

Specifications Subject to Change without Notice

May 22, 2017
TTN119487-S01, Rev B

THORLABS

FINAL INSPECTION REPORT

2x2 50:50 Narrowband Coupler

Item #: TN785R5A2
SN: T045116

Center Wavelength: 785 nm
Coupling Ratio Specification
  Signal Output: 45 % - 55 %
  Tap Output: 45 % - 55 %
Bandwidth: ±15 nm
Maximum Optical Power[a]
  With Connectors or Bare Fiber: 0.5 W
  Spliced: 2 W
Fiber Type: Coherent 780-HP

Test Data[b]	
Excess Loss[c]	≤ 0.3 dB
Input-Output Path	White (Input) – White (Signal Output)
Coupling Ratio[d]	50.4 %
Insertion Loss[e]	3.16 dB
Input-Output Path	White (Input) – Red (Tap Output)
Coupling Ratio[d]	49.6 %
Insertion Loss[e]	3.24 dB

a. Specifies the maximum power allowed through the component. Performance and reliability under high power conditions must be determined within the user's setup.
b. All values are measured at room temperature without connectors through the white input port.
c. Ratio of the input optical power to the total optical power from all output ports. It is measured at the center wavelength.
d. Does not include losses, as this is a measurement of the output power distribution only.
e. Includes both the split of the power between the two outputs, as well as any optical losses in the coupler.

Verified by: 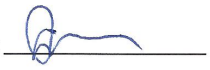

References

[1] Q. Xiao, A. Sow, B. Maxwell, and M. I. Radulescu, "Effect of boundary layer losses on 2d detonation cellular structures," *Proceedings of the Combustion Institute*, 2020.

[2] M. I. Radulescu, G. J. Sharpe, C. K. Law, and J. H. S. Lee, "The hydrodynamic structure of unstable cellular detonations," *Journal of Fluid Mechanics*, vol. 580, p. 31–81, 2007.

[3] B. M. Maxwell, R. R. Bhattacharjee, S. S. M. Lau-Chapdelaine, S. A. E. G. Falle, G. J. Sharpe, and M. I. Radulescu, "Influence of turbulent fluctuations on detonation propagation," *Journal of Fluid Mechanics*, vol. 818, p. 646–696, 2017.

[4] J. H. S. Lee, *The Detonation Phenomenon*. Cambridge University Press, 2008.

[5] P. A. Thompson, *Compressible-fluid dynamics*. McGraw-Hill, 1972.

[6] W. Fickett and W. Davis, *Detonation: Theory and Experiment*. Dover books on physics, Dover Publications, 2000.

[7] R. A. Strehlow and A. J. Crooker, "The structure of marginal detonation waves," *Acta Astronautica*, vol. 1, no. 3, pp. 303 – 315, 1974.

[8] V. Subbotin, "Two kinds of transverse wave structures in multifront detonation," *Combustion, Explosion and Shock Waves*, vol. 11, no. 1, pp. 83–88, 1975.

[9] M. I. Radulescu, *The propagation and failure mechanism of gaseous detonations: experiments in porous-walled tubes*. PhD thesis, McGill University Libraries, 2003.

[10] J. M. Powers, "Review of multiscale modeling of detonation," *Journal of Propulsion and Power*, vol. 22, no. 6, pp. 1217–1229, 2006.

[11] E. A. Lundstorm and A. K. Oppenheim, "On the influence of non-steadiness on the thickness of the detonation wave," *Proc. Roy. Soc.*, vol. 310, pp. 463–478, 1969.

[12] C. A. Eckett, J. J. Quirk, and J. E. Shepherd, "The role of unsteadiness in direct initiation of gaseous detonations," *Journal of Fluid Mechanics*, vol. 421, pp. 147–183, 2000.

[13] P. Vidal and B. A. Khasainov, "Analysis of critical dynamics for shock-induced adiabatic explosions by means of the Cauchy problem for the shock transformation," *Shock Waves*, vol. 9, no. 4, pp. 273–290, 1999.

[14] J. Austin, *The role of instability in gaseous detonation*. PhD thesis, California Institute of Technology, Pasadena, California, 2003.

[15] V. N. Gamezo, D. Desbordes, and E. S. Oran, "Two-dimensional reactive flow dynamics in cellular detonation waves," *Shock Waves*, vol. 9, pp. 11–17, Jan. 1999.

[16] C. Kiyanda and A. Higgins, "Photographic investigation into the mechanism of combustion in irregular detonation waves," *Shock Waves*, vol. 23, no. 2, pp. 115–130, 2013.

[17] M. I. Radulescu and B. M. Maxwell, "Critical ignition in rapidly expanding self-similar flows," *Physics of Fluids*, vol. 22, no. 6, p. 066101, 2010.

[18] M. I. Radulescu, "On the shock change equations," *Physics of Fluids*, vol. 32, no. 5, p. 056106, 2020.

[19] D. G. Goodwin, H. K. Moffat, and R. L. Speth, "Cantera: An object-oriented software toolkit for chemical kinetics, thermodynamics, and transport processes." http://www.cantera.org, 2017. Version 2.3.0.

[20] S. Kao and J. Shepherd, "Numerical solution methods for control volume explosions and znd detonation structure," *Galcit report fm2006*, vol. 7, pp. 1–46, 2008.

[21] F. A. Williams, "Chemical-Kinetic Mechanisms for Combustion Applications, San Diego Mechanism web page, Mechanical and Aerospace Engineering (Combustion Research), University of California at San Diego (http://combustion.ucsd.edu)," 2014.

[22] F. Williams, *Combustion Theory*. CRC Press, 2018.

[23] M. Drolet, "Design of an experiment to study the instability of detonation waves," tech. rep., University of Ottawa, Ottawa, Ontario, 2008. undergraduate thesis.

[24] G. S. Settles, *Schlieren and shadowgraph techniques: visualizing phenomena in transparent media*. Springer, 2013.

[25] S. I. Jackson, C. Chiquete, and M. Short, "An intrinsic velocity–curvature–acceleration relationship for weakly unstable gaseous detonations," *Proceedings of the Combustion Institute*, 2018.

[26] H. Hamam and S. Guizani, *Optical Fiber Communications*, pp. 692–707. John Wiley & Sons, Ltd, 2011.

[27] I. Cernak and L. J. Noble-Haeusslein, "Traumatic brain injury: An overview of pathobiology with emphasis on military populations," *Journal of Cerebral Blood Flow & Metabolism*, vol. 30, p. 255–266, Oct 2009.

[28] E. G. Damon, C. S. Gaylord, W. Hicks, J. T. Yelverton, and D. R. Richmond, "The effect of ambient pressure on tolerance of mammals to air blast," tech. rep., Defence Atomic Support Agency, Washington D.C., 1966.

[29] V. Bogo, R. Hutton, and A. Bruner, "Technical progress report on contract no da-49-146-xz-372," *Vol. DASA*, vol. 2659, 1971.

[30] M. I. P. Radulescu, *31st International Symposium on Shock Waves 2*, ch. On the Relation Between the Shock Wave Thickness in Biomaterials and the Threshold for Blast-Induced Neurotrauma, pp. 391–399. Springer International Publishing, 2019.

[31] J. E. Parsons, C. A. Cain, and J. B. Fowlkes, "Cost-effective assembly of a basic fiber-optic hydrophone for measurement of high-amplitude therapeutic ultrasound fields," *The Journal of the Acoustical Society of America*, vol. 119, no. 3, pp. 1432–1440, 2006.

[32] P. Lewin, C. Mu, S. Umchid, A. Daryoush, and M. El-Sherif, "Acousto-optic, point receiver hydrophone probe for operation up to 100 mhz," *Ultrasonics*, vol. 43, p. 815–821, Dec 2005.

[33] C. Mu, S. Umchid, L. Bansal, P. Lewin, M. El-Sherif, and A. Daryoush, "Broadband fiber optic ultrasound hydrophone probe," in *Proceedings of the Lightwave Technologies in Instrumentation and Measurement Conference, 2004.*, IEEE, 2004.

[34] J. Staudenraus and W. Eisenmenger, "Fibre-optic probe hydrophone for ultrasonic and shock-wave measurements in water," *Ultrasonics*, vol. 31, no. 4, pp. 267 – 273, 1993.

[35] A. Coleman, E. Draguioti, R. Tiptaf, N. Shotri, and J. Saunders, "Acoustic performance and clinical use of a fibreoptic hydrophone," *Ultrasound in Medicine & Biology*, vol. 24, no. 1, pp. 143 – 151, 1998.

[36] V. Wilkens and C. Koch, "Fiber-optic multilayer hydrophone for ultrasonic measurement," *Ultrasonics*, vol. 37, p. 45–49, Jan 1999.

[37] A. Mastro, M. Babich, W. Taylor, and A. Keith, "Diffusion of a small molecule in the cytoplasm of mammalian cells," in *Proceedings of the National Academy of Sciences of the United States of America*, vol. 81, p. 3414–3418, June 1984.

[38] M. Nakahara, K. Nagayama, and Y. Mori, "Shockwave dynamics of high pressure pulse in water and other biological materials based on hugoniot data," *Japanese Journal of Applied Physics*, vol. 47, pp. 3510–3517, may 2008.

[39] Thorlabs, "Single mode fc/apc fiber optic patch cables."

[40] B. Xu, Y. Liu, D. Wang, D. Jia, and C. Jiang, "Optical fiber fabry–pérot interferometer based on an air cavity for gas pressure sensing," *IEEE Photonics Journal*, vol. 9, no. 2, pp. 1–9, 2017.

[41] S. J. Rupitsch, *Piezoelectric Sensors and Actuators*. Springer Berlin Heidelberg, 2019.

[42] T. Kanada and K. Nawata, "Injection laser characteristics due to reflected optical power," *IEEE Journal of Quantum Electronics*, vol. 15, no. 7, pp. 559–565, 1979.

[43] Thorlabs, "Pda10a2 si amplified fixed gain detector user guide."

[44] M. Johnson, *Fundamental Noise Basics and Calculations*, ch. 3. New York: McGraw-Hill Education, 2003.

[45] G. P. Agrawal, *Fiber-optic communication systems*. Wiley series in microwave and optical engineering, Wiley, 4th ed ed., 2010.

[46] P. Morris, A. Hurrell, A. Shaw, E. Zhang, and P. Beard, "A fabry–pérot fiber-optic ultrasonic hydrophone for the simultaneous measurement of temperature and acoustic pressure," *The Journal of the Acoustical Society of America*, vol. 125, no. 6, pp. 3611–3622, 2009.